INVERSE COMPTON LIGHT SOURCE:

A COMPACT DESIGN PROPOSAL

by

Kirsten Elizabeth Deitrick
B.S. May 2011, Rensselaer Polytechnic Institute
M.S. August 2014, Old Dominion University

A Dissertation Submitted to the Faculty of
Old Dominion University in Partial Fulfillment of the
Requirements for the Degree of

DOCTOR OF PHILOSOPHY

PHYSICS

OLD DOMINION UNIVERSITY
May 2017

Approved by:

Jean R. Delayen (Director)

Geoffrey A. Krafft (Member)

Todd Satogata (Member)

Sebastian E. Kuhn (Member)

Masha Sosonkina (Member)

ABSTRACT

INVERSE COMPTON LIGHT SOURCE: A COMPACT DESIGN PROPOSAL

Kirsten Elizabeth Deitrick
Old Dominion University, 2017
Director: Dr. Jean R. Delayen

In the last decade, there has been an increasing demand for a compact Inverse Compton Light Source (ICLS) which is capable of producing high-quality X-rays by colliding an electron beam and a high-quality laser. It is only in recent years when both SRF and laser technology have advanced enough that compact sources can approach the quality found at large installations such as the Advanced Photon Source at Argonne National Laboratory. Previously, X-ray sources were either high flux and brilliance at a large facility or many orders of magnitude lesser when produced by a bremsstrahlung source. A recent compact source was constructed by Lyncean Technologies using a storage ring to produce the electron beam used to scatter the incident laser beam. By instead using a linear accelerator system for the electron beam, a significant increase in X-ray beam quality is possible, though even subsequent designs also featuring a storage ring offer improvement. Preceding the linear accelerator with an SRF reentrant gun allows for an extremely small transverse emittance, increasing the brilliance of the resulting X-ray source. In order to achieve sufficiently small emittances, optimization was done regarding both the geometry of the gun and the initial electron bunch distribution produced off the cathode. Using double-spoke SRF cavities to comprise the linear accelerator allows for an electron beam of reasonable size to be focused at the interaction point, while preserving the low emittance that was generated by the gun. An aggressive final focusing section following the electron beam's exit from the accelerator produces the small spot size at the interaction point which results in an X-ray beam of high flux and brilliance. Taking all of these advancements together, a world class compact X-ray source has been designed. It is anticipated that this source would far outperform the conventional bremsstrahlung and many other compact ICLSs, while coming closer to performing at the levels found at large facilities than ever before. The design process, including the development between subsequent iterations, is presented here in detail, with the simulation results for this groundbreaking X-ray source.

ACKNOWLEDGMENTS

I would first like to thank my advisor Professor Jean Delayen for providing me with this project and the resources necessary to complete it. Professor Geoff Krafft also provided excellent guidance along the way, in addition to numerous rounds of editing this document. I would like to thank Professors Todd Satogata, Sebastian Kuhn, and Masha Sosonkina for serving on my committee.

Several colleagues who worked on this project at the beginning deserve acknowledgement as well. Karim Hernández-Chahín, Rocio Olave, Christopher Hopper, and Randika Gamage helped to create the original design which I worked to improve and in the process taught me much in their particular areas of knowledge. Professor Balša Terzić and Erik Johnson helped in their simulation of the scattered X-rays at the end of my project.

Finally, I would like to express the deepest gratitude to my family and friends who have supported and encouraged me throughout this entire endeavor. They always told me it was well-within my capabilites, even when I doubted myself. I could not have done this without all of you.

TABLE OF CONTENTS

LIST OF TABLES

LIST OF FIGURES

CHAPTER 1

INTRODUCTION

1.1 CURRENT X-RAY SOURCES AND PERFORMANCE

Since their discovery in 1895, X-rays have been a powerful technique for determining the structure of condensed matter. For the first 70 years of using X-rays, sources barely changed from the original bremsstrahlung tubes used in their discovery [1]. Until recently, large accelerator-based synchrotron facilities set the standard for the highest quality X-ray beams [1]. At present, this standard has been largely surpassed in free electron lasers (FELs) [2]. Third generation light sources are synchrotrons with undulators, while fourth generation light sources are FELs driven by either a linear accelerator (linac) or an energy-recovery linear accelerator (ERL). Compact ICLS designs do not fall into either category.

While making a complete list of existing or planned light sources is beyond the scope of this dissertation, a few examples of each aforementioned type are given. Third generation synchrotron radiation sources are well established compared to their fourth generation successors. Such sources include the Advanced Light Source (ALS) at Lawrence Berkeley National Laboratory (LBNL), the Advanced Photon Source (APS) at Argonne National Laboratory (ANL), the SPring-8 (Super Photon ring-8 GeV) at the Japan Synchrotron Radiation Research Institute (JASRI), and the European Synchrotron Radiation Facility (ESRF) in Europe [3].

Among existing fourth generation installations are the Linac Coherent Light Source (LCLS) at the Stanford Linear Accelerator Center (SLAC), the Free electron LASer at Hamburg (FLASH) at DESY (Deutsches Elektronen-SYnchrotron), SPring-8 Compact SASE Source (SCSS) at JASRI, and the ERL-FEL at Jefferson Lab (JLab) [4–9]. Another facility, the European XFEL is being finalized and is expected to be available to users in 2017, while at Cornell an ERL partially coherent X-ray source has been proposed [4, 9, 10]. One advantage of linac-driven FELs is typically a more coherent X-ray beam, compared to the beam produced by ERL-driven FELs [2]. Table 1.1 shows both properties of specific installations and ranges of values for different types of installations [2, 11]. As a generalization, the desire is for shorter pulse lengths, higher average brilliance, and coherence in the X-rays [12].

TABLE 1: Typical X-ray beams at large-scale installations [2, 11].

	Pulse duration (ps)	Average brilliance (ph/(s-mm^2-mrad^2-0.1%BW)
3$^{\text{rd}}$ generation synchrotron	30	$10^{17} - 10^{20}$
APS	>20	3×10^{19}
4$^{\text{th}}$ generation FEL	0.1	$10^{22} - 10^{24}$
4$^{\text{th}}$ generation ERL	0.1 - 1	$10^{19} - 10^{22}$
Cornell ERL high flux	1.7	6×10^{21}
Cornell ERL high coherence	2	2×10^{22}

For a photon beam source, the spectral brightness parameter or spectral brilliance is defined as the six-dimensional (6D) volume of the beam as calculated in phase space [13]. For the purpose of this discussion, a sufficiently accurate expression of brilliance is

$$\mathcal{B} \approx \frac{\gamma^2 \mathcal{F}_{0.1\%}}{4\pi^2 \epsilon^N_{x,rms} \epsilon^N_{y,rms}}. \tag{1}$$

In the above formula, $\mathcal{F}_{0.1\%}$ is the flux of the X-ray beam within a 0.1% bandwidth, γ is the relativistic factor of the electron beam, $\epsilon^N_{x,rms}$ is the normalized *rms* horizontal emittance, and $\epsilon^N_{y,rms}$ is the normalized *rms* vertical emittance [12, 13]. These quantities will be defined in greater detail in Section 2.2 and as discussed there, Eq. (1) applies for electron beam energies of 10s of MeVs.

It can easily be seen that while the normalized transverse emittances of the electron beam are an important factor in this calculation, they are not the only factor which influences the brightness of the X-ray beam. For example, take two electron beams with the same bunch charge and spot sizes, which will produce the same value for $\mathcal{F}_{0.1\%}$ for identical scattering lasers. If the first beam has an energy of 25 MeV with normalized emittances of 0.1 mm-mrad, while the second has an energy of 50 MeV with normalized emittances of 0.2 mm-mrad then the brightness of the two produced X-ray beams will be identical. Despite having a larger normalized *rms* transverse emittance, the 50 MeV beam will be just as bright as the 25 MeV beam, though the energy of the resulting X-ray beams will be different for the two beams.

1.2 APPLICATIONS

There are many X-ray experiment techniques that exist today; any given technique may

be used in a wide range of fields. Some of the more prominent techniques currently in use include phase contrast imaging (PCI), absorption radiography, K-edge subtraction imaging, radiotherapy (treatment of tumors with X-rays), and computed tomography (CT). Some of the fields in which these techniques are used include medicine, cultural heritage, material science development, and industry [12, 14].

1.3 COMPACT PHOTON SOURCES

At present, most high brilliance sources exist at large facilities, especially third-generation synchrotron light sources [12]. However, due to various concerns, among them cost, risk of transporting valuable items, and limited available runtime at large facilities, there has been an increasing demand for laboratory-scale sources. Sometimes referred to as "compact", one description is any machine that fits in a 100 m^2 area. Additional desirable constraints are that the purchase and operating cost are not prohibitive for the smaller facilities and that the operation of a such a machine is possible by non-experts.

There are two main components in an inverse Compton light source (ICLS) - a relativistic electron beam and a scattering laser. In the last several years, there has been a significant advancement in the technology to produce a suitable scattering laser. The details of this progress are largely beyond the scope of this document, though the status of the current technology will be touched on later. The other component, the focus of this project, is the relativistic electron beam off which the incident laser scatters.

There exist two schemes for accelerating an electron beam to the desired energy, typically in the range of a few 10s of MeV: a linear accelerator (linac) or a storage ring (ring) [14]. A linac is composed of radiofrequency (RF) or superconducting (SC) RF (SRF) cavities that accelerate the beam to the desired energy [13]. Rings are circular devices into which a beam of a specific energy is injected, where the beam may or may not be extracted before being used [15].

Both of these options have benefits and drawbacks. Existing storage ring projects currently in development (designing or commissioning) typically have lower expected fluxes than those of linacs. The expected brightness is frequently lower [14], as the smallest achievable normalized emittances are typically larger for a ring than a linac. Additionally, a full energy linac is often required anyway for injection into the ring [1,13,14]. However, rings are capable of a high repetition rate, a higher average current than is typical for linacs, and historically have better stability [1, 14].

Linac-based ICS X-ray sources have shown promising results at lower pulse repetition

rates, though these results have yet to be reproduced at higher rates. For electron beams with an energy above 10 MeV, cumbersome shielding must be included [1, 14]. Current cryogenic equipment for SRF structures, which are used in all but one of the known linac projects (and, indeed, are by some assumed to be necessary for a linac project to succeed), are more complicated than non-expert users are comfortable using. Another common feature to most linac projects is a superconducting electron gun, a technology with promising results but not yet a mature field [14, 16]. Linac projects are more likely to be capable of shorter bunch lengths, even without compression, smaller normalized emittances, and a greater flexibility for phase space manipulations than ring projects [1, 14].

Referenced in the literature as the only existing compact ICLS is the one built by Lyncean Technologies. An electron beam is produced by a normal conducting linac and injected into a storage ring, which occupies a 1 m by 2 m footprint. This machine delivers $\sim 10^9$ ph/s in a 3% energy bandwidth, with the scattered photon beam having an *rms* spot size of ~ 45 μm [14, 17].

Table 2 contains some of the current projects with a compact ICLS design. To give some perspective to these values, the best rotating anodes, such as may currently be found in a lab as an X-ray source, have a flux of $\sim 6 \times 10^9$ ph/s and a brightness on the order of 10^9 photons/(sec-mm^2-mrad^2-0.1%BW) [1]. On the other hand, an X-ray beam that might typically be found at a large facility has a flux in the regime of $\sim 10^{11} - 10^{13}$ ph/s [18] and a brightness of $\sim 10^{19}$ photons/(sec-mm^2-mrad^2-0.1%BW) [11].

Given these numbers, a robust user program for a compact ICLS machine would require that substantial fluxes of narrow-band X-rays are the desired requirement, rather than the best average brightness. However, the potential for such machines, in terms of both performance and demand, make the prospect of a well-designed compact source significant [12].

1.4 TARGET SPECIFICATIONS FOR THE LINAC DESIGN

For an "interesting" compact source, the X-ray beam produced must be considerably higher quality than is currently available from small scale facilities. A recent paper [14] covering compact Compton sources predicted that in the near future a superconducting linac-based machine would be expected to produce a flux of $\sim 10^{13} - 10^{14}$ ph/s and a brightness on the order of $10^{12} - 10^{15}$ ph/(sec-mm^2-mrad^2-0.1%BW). One other possible figure of merit is the transverse coherence length, which increases as the source size decreases. As the transverse size of the X-ray beam decreases with the electron beam spot size, a narrower electron beam produces a greater transverse coherence length [14].

TABLE 2: Comparison of X-ray beam parameters for different ICLS compact designs.

Project	Type	E_x (keV)	Ph/s	Ph/(s-mrad^2 -mm^2-0.1%BW)	σ_x (μm)
Lyncean [12, 17, 19]	SR	10-20	10^{11}	10^{11}	45
TTX [20]	SR	20-80	10^{12}	10^{10}	50
LEXG [21]	SR (SC)	33	10^{13}	10^{11}	20
ThomX [22]	SR	20-90	10^{13}	10^{11}	70
KEK QB [23]	Linac (SC)	35	10^{13}	10^{11}	10
KEK ERL [24]	Linac (SC)	67	10^{13}	10^{11}	30
NESTOR [25]	SR	30-500	10^{13}	10^{12}	70
MIT [1]	Linac	12	10^{13}	10^{12}	2
ODU	**Linac (SC)**	**$\leq$ 12**	$\mathbf{10^{14}}$	$\mathbf{10^{15}}$	**3**

A starting point for our linac design was the decision to run at 4.2 K instead of 2 K. This choice is made for two main reasons - making the system easier to operate and reducing the operating cost. This operating temperature requires a lower frequency for the SRF structures - on the order of a few hundred MHz instead of one GHz or higher [26].

To increase brightness, the normalized *rms* transverse emittance needs to be minimized, leading to a target value of 0.1 mm-mrad. While this value is considerably smaller than in other SRF injector guns, as shown in this thesis, a small bunch charge of 10 pC makes this emittance attainable [16, 26]. To attain a high average flux, considering that the average flux is proportional to both the bunch charge and the repetition rate, a high repetition rate of 100 MHz was chosen to counterbalance the low bunch charge. Minimizing the spot size of both electron and laser beams also helped to increase the flux. Thus, the spot size for both was set at $\sim$3 μm, which is small but feasible.

An electron beam energy of 25 MeV and an incident scattering laser energy of 1.24 eV were chosen. At this laser energy, the interaction is within the Thomson regime, so the energy of the scattered X-rays is given by

$$E_{\mathrm{X-ray}} = 4\gamma^2 E_{laser} \tag{2}$$

where γ is the relativistic factor of the electron beam and E_{laser} is the energy of the incident laser [12]. The chosen energies of 25 MeV for the electron beam and 1.24 eV for the laser generate X-rays of up to 12 keV. X-rays at 12 keV have a corresponding wavelength of approximately one Angstrom, the same as in large third generation synchrotron facilites.

For the energy smearing of the forward flux to be small relative to the total bandwidth necessitates that the relative beam energy spread be less than 0.03%. At the chosen energy of 25 MeV, this leads to an *rms* energy spread requirement of 7.5 keV. In order to keep the flux reduction due to the hourglass effect negligible, the compressed bunch length is set to < 1 mm [26].

For the best possible X-ray beam, a high quality high power laser is necessary. The ideal laser would, among other properties, have a circulating power of 1 MW, compared to 100 kW today. One MW is widely regarded as feasible, but has not yet been achieved [12, 14, 26, 27]. The other properties relevant to the optical cavity are less demanding: 1 μm wavelength (1.24 eV), 5×10^{16} ph/bunch, spot size of 3.2 μm at collision, and peak strength parameter $a = 0.026$, a term which is defined in the next chapter [26].

It is possible to take the properties of the electron beam and incident laser beam and estimate selected parameters of the X-ray beam which would be produced from a collision between the two. These formulae are presented in the next chapter, however the results will be summarized here. The X-ray beam energy will be 12 keV with 1.6×10^6 photons/bunch. The X-ray beam flux will be 1.6×10^{14} ph/s, with an average brilliance of 1.5×10^{15} ph/(sec-mm^2-mrad^2-0.1%BW) [12,26]. These values are sufficiently high as to indicate that a compact Compton source which fulfills these parameters is likely to be very interesting to potential users [14].

These specifications are based on and similar to those earlier presented in [27]. Desired electron beam parameters at the interaction point (IP) are shown in Table 3. Optical cavity parameters are shown in Table 4, based on performances that may soon be attainable [12,27]. Using the values in these tables and the formulae presented in Section 2.4 of the next chapter, the resulting X-ray beam can be described by the quantities in Table 5.

TABLE 3: Electron beam parameters at interaction point.

Parameter	Quantity	Units
Energy	25	MeV
Bunch charge	10	pC
Repetition rate	100	MHz
Average current	1	mA
Transverse *rms* normalized emittance	0.1	mm-mrad
$\beta_{x,y}$	5	mm
$\sigma_{x,y}$	3	μm
FWHM bunch length	3 (0.9)	psec (mm)
rms energy spread	7.5	keV

TABLE 4: Laser parameters at interaction point.

Parameter	Quantity	Units
Wavelength	1 (1.24)	μm (eV)
Circulating power	1	MW
N_γ, Number of photons/bunch	5×10^{16}	
Spot size (*rms*)	3.2	μm
Peak strength parameter, $a = eE\lambda_{laser}/2\pi mc^2$	0.026	
Repetition rate	100	MHz
Pulse duration	50	ps

TABLE 5: Light source parameters.

Parameter	Quantity	Units
X-ray energy	Up to 12	keV
Photons/bunch	1.6×10^6	
Flux	1.6×10^{14}	photon/sec
Average brilliance	1.5×10^{15}	photon/(sec-mm^2-mrad^2-0.1%BW)

CHAPTER 2

INVERSE COMPTON LIGHT SOURCE

2.1 BACKGROUND

2.1.1 SPECIAL RELATIVITY AND BEAM DYNAMICS

For a particle of speed v and rest mass m, its "normalized" speed is β, such that $\beta \equiv v/c$ where c is the speed of light. The relativistic factor, γ, is given by

$$\gamma \equiv 1/\sqrt{1-\beta^2}, \tag{3}$$

with a kinetic energy of $(\gamma-1)mc^2$, and a total energy of γmc^2. The relativistic momentum is given by $\mathbf{p} = \gamma m\mathbf{v}$, where $\mathbf{v}$ is the velocity of the particle. Nonrelativistic approximations (classical mechanics) apply when $\beta \ll 1$ [28, 29].

Let there be two inertial reference frames, K and K', with $\mathbf{v}$ being the relative velocity between them. The space-time coordinate for a point is given by (ct, x, y, z) and (ct', x', y', z'), in the K and K' frames, respectively. Let $x_0 \equiv ct, \mathbf{x} = (x, y, z)$ with x_0' and $\mathbf{x}'$ defined similarly. Additionally, let the "normalized" velocity $\boldsymbol{\beta}$ be defined, such that $\boldsymbol{\beta} = \mathbf{v}/c$ and $\beta = |\boldsymbol{\beta}|$. Then the Lorentz transformation, relating the time-space coordinates in the two frames, is given by

$$\begin{aligned} x_0' &= \gamma(x_0 - \boldsymbol{\beta}\cdot\mathbf{x}) \\ \mathbf{x}' &= \mathbf{x} + \frac{\gamma-1}{\beta^2}(\boldsymbol{\beta}\cdot\mathbf{x})\boldsymbol{\beta} - \gamma\boldsymbol{\beta}x_0. \end{aligned} \tag{4}$$

It can be seen that for nonrelativistic speeds between the two frames (i.e., $\beta \sim 0, \gamma \sim 1$), Eq. (4) simplifies into the Galilean transformation [29].

For a photon in a plane wave of frequency ω and wave vector $\mathbf{k}$ in the inertial reference frame K, then in the reference frame K' which moves for at speed $\boldsymbol{\beta}c$ with respect to frame K, this plane wave will have a frequency of ω' and wave vector $\mathbf{k}'$. Because the phase of the plane wave remains constant regardless of frame,

$$\phi = \omega t - \mathbf{k}\cdot\mathbf{x} = \omega' t' - \mathbf{k}'\cdot\mathbf{x}' \tag{5}$$

is a Lorentz invariant. Because the phase is invariant, $(\omega, \mathbf{k})$ is a 4-vector. Subsituting for the coordinates in K' with the equivalent expression in K coordinates, it is found by Lorentz transformation that

$$\begin{aligned} k'_0 &= \gamma(k_0 - \boldsymbol{\beta}\cdot\mathbf{k}) \\ k'_{\parallel} &= \gamma(k_{\parallel} - \beta k_0) \\ \mathbf{k'}_{\perp} &= \mathbf{k}_{\perp} \end{aligned} \tag{6}$$

with $\omega' = ck'_0$ and $\omega = ck_0$. For light waves, $|\mathbf{k}| = k_0$ and $|\mathbf{k}'| = k'_0$. With this additional relationship, Eq. (6) can be written as

$$\begin{aligned} \omega' &= \gamma\omega(1 - \beta\cos\theta) \\ \tan\theta' &= \frac{\sin\theta}{\gamma(\cos\theta - \beta)} \end{aligned} \tag{7}$$

with the inverse formulae

$$\begin{aligned} \omega &= \gamma\omega'(1 + \beta\cos\theta') \\ \tan\theta &= \frac{\sin\theta'}{\gamma(\cos\theta' + \beta)} \end{aligned} \tag{8}$$

where θ and θ' are the angles of $\mathbf{k}$ and $\mathbf{k}'$, respectively, relative to the direction of $\mathbf{v}$ [29]. Equations (7) and (8) provide the relativistic transformation rule for the scattering angle.

The relativistically correct generalization of Newton's law relating force and the rate of change of momentum is $\mathbf{F} = d\mathbf{p}/dt$. Applying the definition of relativistic momentum given previously yields

$$\mathbf{F} = m\frac{d}{dt}\gamma\mathbf{v}. \tag{9}$$

For a particle with charge q and velocity $\mathbf{v}$ in an electric field $\mathbf{E}$ and magnetic induction $\mathbf{B}$, then

$$\mathbf{F} = q(\mathbf{E} + \mathbf{v}\times\mathbf{B}) \tag{10}$$

is the Lorentz force acting on that particle [28, 29]. The above formula can also be written as

$$\frac{d(\gamma\mathbf{v})}{dt} = \frac{q}{m}(\mathbf{E} + \mathbf{v}\times\mathbf{B}). \tag{11}$$

In this project, the electromagnetic (EM) fields which act on the particles in the bunch are both external (SRF cavities, magnets) and internal (the EM fields generated by the bunch acting upon each particle in the bunch).

2.1.2 MAXWELL'S EQUATIONS AND ELECTROMAGNETIC FIELDS

In a source-free vacuum, Maxwell's equations (SI units) are given by

$$\begin{aligned} \boldsymbol{\nabla}\cdot\mathbf{E} &= 0 \\ \boldsymbol{\nabla}\times\mathbf{B} &= \frac{1}{c^2}\frac{\partial\mathbf{E}}{\partial t} \\ \boldsymbol{\nabla}\times\mathbf{E} &= -\frac{\partial\mathbf{B}}{\partial t} \\ \boldsymbol{\nabla}\cdot\mathbf{B} &= 0 \end{aligned} \tag{12}$$

with c the speed of light, $\mathbf{E}$ the electric field, and $\mathbf{B}$ the magnetic induction. The wave equation for the electic and magnetic fields is given by

$$\begin{aligned} \boldsymbol{\nabla}^2\mathbf{E} - \frac{1}{c^2}\frac{\partial^2\mathbf{E}}{\partial t^2} &= 0 \\ \boldsymbol{\nabla}^2\mathbf{B} - \frac{1}{c^2}\frac{\partial^2\mathbf{B}}{\partial t^2} &= 0 \end{aligned} \tag{13}$$

Ideally, a cavity is a vacuum volume enclosed by perfectly conducting surfaces. The boundary conditions between a vacuum and an ideal perfect conductor are given by

$$\begin{aligned} \hat{n}\cdot\mathbf{B} &= 0 \\ \hat{n}\times\mathbf{E} &= 0 \end{aligned} \tag{14}$$

where $\hat{n}$ is the vector normal to the surface, which is equivalent to imposing the requirement that there is no parallel electric field or normal magnetic field at the surface [29]. Consequently, the EM fields within the cavity are the solutions to Maxwell's equations in a vacuum (12) and the wave equation (13) that satisfy the boundary conditions (14).

Consider a cavity in the shape of a simple cylinder, which is known as a pillbox cavity. For any cylindrical geometry, the electromagnetic fields will be in the form of

$$\begin{aligned} \mathbf{E}(x,y,z,t) &= \mathbf{E}(x,y)e^{j(kz-\omega t)} \\ \mathbf{H}(x,y,z,t) &= \mathbf{H}(x,y)e^{j(kz-\omega t)}, \end{aligned} \tag{15}$$

where k is the wave number and $\omega = 2\pi f$ is the angular frequency of the cavity. Two types of solutions exist to the wave equation, depending on the boundary condtion - transverse magnetic (TM) and transverse electric (TE) modes. The solutions for a pillbox cavity of

radius R and length L in a TM mode are given by

$$\begin{aligned}
E_z &= E_0 \cos\left(\frac{p\pi z}{L}\right) J_m\left(\frac{x_{mn} r}{R}\right) \cos(m\phi) \\
E_r &= -E_0 \frac{p\pi R}{L x_{mn}} \sin\left(\frac{p\pi z}{L}\right) J'_m\left(\frac{x_{mn} r}{R}\right) \cos(m\phi) \\
E_\phi &= E_0 \frac{mp\pi R^2}{rLx_{mn}^2} \sin\left(\frac{p\pi z}{L}\right) J_m\left(\frac{x_{mn} r}{R}\right) \sin(m\phi) \\
H_z &= 0 \\
H_r &= jE_0 \frac{m\omega R^2}{c\eta r x_{mn}^2} \cos\left(\frac{p\pi z}{L}\right) J_m\left(\frac{x_{mn} r}{R}\right) \sin(m\phi) \\
H_\phi &= jE_0 \frac{\omega R}{c\eta x_{mn}} \cos\left(\frac{p\pi z}{L}\right) J'_m\left(\frac{x_{mn} r}{R}\right) \cos(m\phi)
\end{aligned} \tag{16}$$

and the solutions in a TE mode are given by

$$\begin{aligned}
H_z &= H_0 \sin\left(\frac{p\pi z}{L}\right) J_m\left(\frac{x'_{mn} r}{R}\right) \cos(m\phi) \\
H_r &= H_0 \frac{p\pi R}{L x'_{mn}} \cos\left(\frac{p\pi z}{L}\right) J'_m\left(\frac{x'_{mn} r}{R}\right) \cos(m\phi) \\
H_\phi &= -H_0 \frac{mp\pi R^2}{rL(x'_{mn})^2} \cos\left(\frac{p\pi z}{L}\right) J_m\left(\frac{x'_{mn} r}{R}\right) \sin(m\phi) \\
E_z &= 0 \\
E_r &= jH_0 \frac{m\eta\omega R^2}{cr(x'_{mn})^2} \sin\left(\frac{p\pi z}{L}\right) J_m\left(\frac{x'_{mn} r}{R}\right) \sin(m\phi) \\
E_\phi &= jH_0 \frac{\eta\omega R}{cx'_{mn}} \sin\left(\frac{p\pi z}{L}\right) J'_m\left(\frac{x'_{mn} r}{R}\right) \cos(m\phi)
\end{aligned} \tag{17}$$

where c is the speed of light, η is the impedance of free space, ω is the frequency of each mode, J_m is the m^{th} order Bessel function of the first kind, and J'_m is its derivative. The values x_{mn} and x'_{mn} are the n^{th} zero of the Bessel functions J_m and J'_m, respectively. The modes are referred to as TM_{mnp} and TE_{mnp}, where m, n, and p are integers corresponding to the number of sign changes of E_z or H_z in the z, r, and ϕ directions in a cylindrical coordinate system. The frequency of a TM mode is given by

$$\omega_{mnp} = c\sqrt{\left(\frac{x_{mn} c}{R}\right)^2 + \left(\frac{p\pi}{L}\right)^2} \tag{18}$$

while the frequency of a TE mode is given by

$$\omega_{mnp} = c\sqrt{\left(\frac{x'_{mn} c}{R}\right)^2 + \left(\frac{p\pi}{L}\right)^2}. \tag{19}$$

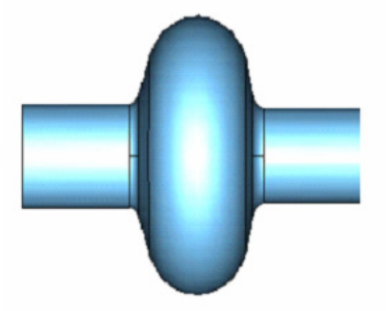

FIG. 1: The profile of a single elliptical cavity.

The lowest possible modes are the TM_{010} and TE_{111} modes. TM_{0np} modes have non-zero E_z components, with TM_{010} being the fundamental accelerating mode [28]. Though using a pillbox cavity would accelerate the beam, it became advantageous to move towards an elliptical cavity, seen in Fig. 1. Eventually, multicell elliptical accelerating structures became a common approach to beam acceleration [30].

Another basic type of cavity is the coaxial resonator. One example of this, the half-wave cavity, is shown in Fig. 2. The mode used to accelerate particles traversing this type of cavity is the TEM mode, referring to transverse electromagnetic mode. In Fig. 2, both the electric and magnetic fields are transverse to the length of the cavity. Spoke cavities also use the TEM mode to accelerate particles [28].

Analytic solutions for EM fields exist for very simple cavity geometries. While the analytical solution to a pillbox cavity has been presented, the EM field found in the cavity is altered by adding beam ports to allow the beam to pass through, let alone altering the geometry to an elliptical shape. For these and other more complex geometries, numerical methods are used to solve for the fields. Some of the numerical techniques used include the Finite Difference Method (FDM), Boundary Element Method (BEM), Finite Element Method (FEM), Finite Volume Method (FVM), and Finite Integration Technique (FIT) [31, 32]. Different simulation tools use different numerical methods to solve for the EM fields [33, 34]. The electromagnetic solvers used for this work are Poisson Superfish and CST Microwave Studio, which are further detailed in Chapter 3.

2.1.3 SRF PARAMETERS OF CAVITIES

There exist a number of "figures of merit" which are helpful in evaluating different SRF cavities. While a more nuanced comparison of two similar cavities may require tracking a

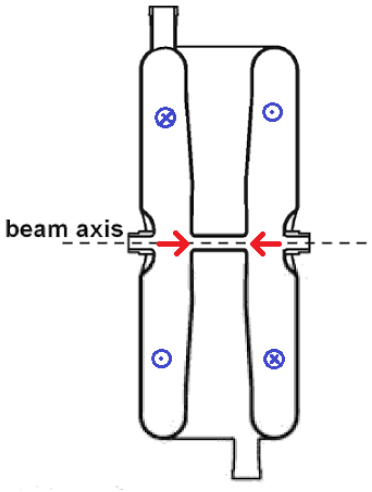

FIG. 2: The profile of a half-wave coaxial resonator. The electric field is shown in red, while the magnetic field is shown in blue.

beam through them, these parameters are useful in initial evaluations of proposed cavity designs.

The voltage gain by a particle is the work done upon that particle by the longitudinal electric field. The voltage gain is given by

$$V_{\text{acc}}(t,\phi) = \int_{-\infty}^{\infty} E_z(z) e^{i(\omega t(z)+\phi)} dz \tag{20}$$

where $E_z(z)$ is the longitudinal electric field as a function of z, ω is the RF frequency, $t(z)$ is the time the particle is located at position z, and ϕ is the phase between the particle and the RF field. For a particle which remains at a constant velocity as it traverses the cavity, the relationship $z = \beta ct$ is true, where βc is the velocity of the particle. Substituting this into Eq. (20), the voltage gain is given by

$$V_{\text{acc}}(\beta,\phi) = \int_{-\infty}^{\infty} E_z(z) e^{i(\omega z/\beta c+\phi)} dz. \tag{21}$$

As can be seen from the above equation, V_{acc} is sinusoidal with respect to ϕ. For a given particle arrival time and velocity, there exists some phase at which V_{acc} is maximum. The value of V_{acc} at this velocity and phase is V_0.

The average accelerating field experienced by the particle is given by

$$E_{\text{acc}} = \frac{V_0}{L} \tag{22}$$

where L is the reference length of the cavity. The parameters of $E_{\text{peak}}/E_{\text{acc}}$ [unitless] and $B_{\text{peak}}/E_{\text{acc}}$ [mT/(MV/m)] give the ratio of the peak electric or magnetic induction field, respectively, on the surface of the cavity to the accelerating field [35]. Throughout this document, these ratios are instead quoted as $E_p^*[MV/m]$ or $B_p^*[mT]$, with ${}^*E_{\text{acc}} = 1\ MV/m$. The ratio $B_{\text{peak}}/E_{\text{peak}}$ or B_p/E_p is also quoted. The energy stored in a cavity is given by

$$U = \frac{1}{2}\epsilon_0 \int_V |\mathbf{E}|^2 dV = \frac{1}{2}\mu_0 \int_V |\mathbf{H}|^2 dV \tag{23}$$

where ϵ_0 is the permittivity of free space, μ_0 is the vacuum permeability, and $|\mathbf{E}|$ and $|\mathbf{H}|$ are the electric and magnetic field, respectively, within the cavity. The integral is taken over the entire cavity [29]. Power dissipation of a cavity is given by

$$P_d = \frac{1}{2}R_s \int_S |\mathbf{H}|^2 dS \tag{24}$$

where R_s is the surface resistance. The integral is taken over the inner surface of the structure. The unloaded quality factor is given by

$$Q_0 = \frac{\omega U}{P_d} \tag{25}$$

where ω is the RF frequency. Q_0 is the ratio of stored energy (U) and the energy dissipated through the inner surface during one radian(P_d). The shunt impedance is given by

$$R = \frac{V_0^2}{P_d} \tag{26}$$

and is a measure of the cavity efficiency in transforming RF power to voltage gain [28]. The ratio $R/Q_0[\Omega]$ is independent of cavity size and material, making it useful for comparing different cavity geometries [35]. The geometry factor is given by

$$G = Q_0 R_s[\Omega] \tag{27}$$

which is also independent of size and material, making it also suitable for the comparison of different cavity shapes. The parameter $RR_s[\Omega^2]$ is sometimes also quoted, though it may be represented as $(R/Q_0)\times Q_0 R_s$. Given that it is the product of two parameters dependent only on cavity shape, it follows that this parameter is also dependent only on cavity shape [28].

2.2 BEAM PARAMETERS

Throughout this document, various beam parameters are used in a number of ways - making approximations, determining desired beam quality, and evaluating simulated beams.

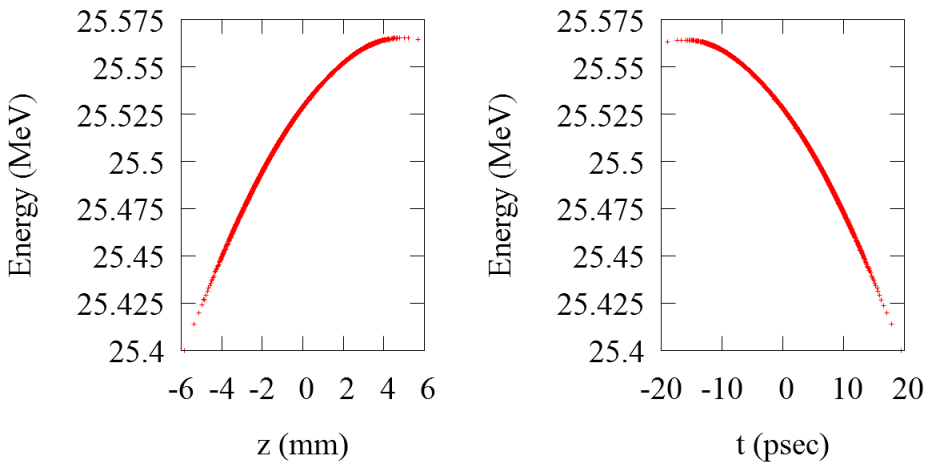

FIG. 3: Identical bunch plotted for (left) E vs z and (right) E vs t.

To make this document more accessible, a collection of the more frequently used terms are explained here.

Assume some number of particles, in this case electrons, exist in a bunch with an ideal (average) energy of E_0. At any given time t in the laboratory, each particle can be described by a set of six coordinates: (x, p_x, y, p_y, z, p_z), where x and y are the transverse positions of the electron, p_x and p_y are the transverse momenta, z is the longitudinal position relative to a reference particle along the beam path, and p_z is the momentum along the beam path. Such a coordinate system is not always the most convenient for calculating and interpreting beam properties, where coordinates as the particles pass a given longitudinal location are preferred. Thus a modified viewpoint, where the phase space coordinates (x, p_x, y, p_y, z, p_z) are functions of the longitudinal coordinate s, the distance along the beam path, and z becomes the longitudinal offset from a reference particle, is standard in accelerator physics. Within this convention, t may replace z, where now t is the additional time it takes for the particle to arrive at the position s compared to the reference particle, such that $t = -z/\beta_z c$. An example of how this difference appears is shown in Fig. 3 where the energy of the particles within a bunch is plotted versus z and t. For a free particle, the energy E of any particle in the bunch is related to its total momentum p by $\beta E = cp = c\sqrt{p_x^2 + p_y^2 + p_z^2}$.

It is often more convenient to use an alternate set of coordinates: $(x, x', y, y', z, \delta)$ where $x' \equiv p_x/p_z$, y' is similarly defined, and $\delta \equiv \Delta p/p_0$ such that $\Delta p \equiv p - p_0$, keeping in mind that p_0 is the momentum of the reference particle. As long as the relative momentum error δ is not too large, $x' \approx p_x/\langle p_z \rangle$.

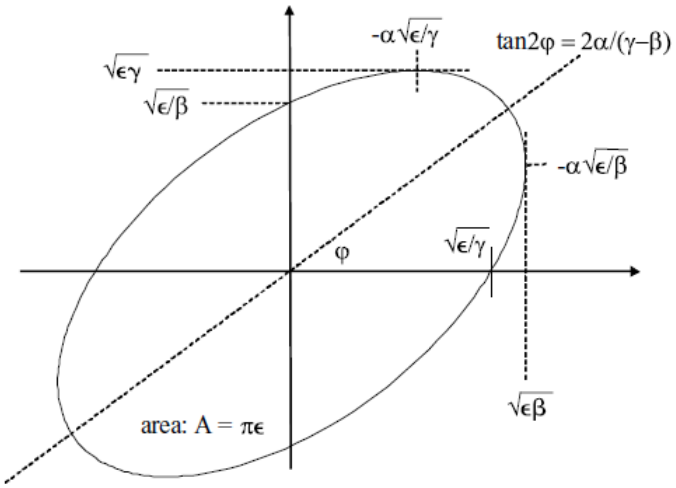

FIG. 4: Phase space ellipse with Twiss parameters.

Beam transverse phase spaces, as they are referenced in this document, typically refer to the horizontal and vertical phase spaces, which are shown as plots of x' vs. x and y' vs. y, respectively, of all the electrons in the bunch. An ellipse can be drawn around a certain percentage of the beam. In the case of the horizontal phase space, this ellipse can be described by

$$\gamma_x x^2 + 2\alpha_x x x' + \beta_x x'^2 = \epsilon_x, \tag{28}$$

where $\alpha_x(s), \beta_x(s), \gamma_x(s)$, and ϵ_x are (horizontal) ellipse parameters, also referred to as Twiss parameters. In order to clarify that the Twiss parameters β and γ, as they appear in the above formula, are not the relativistic factors denoted similarly, subscripts have been added. The formulae for the vertical Twiss parameters are analogous. The area enclosed by the ellipse is $\epsilon_x \pi$, where ϵ_x is the unnormalized horizontal *rms* emittance, while the other parameters describe the shape and orientation of the ellipse. Fig. 4 shows a phase space ellipse and how the Twiss parameters correspond to the drawn ellipse. Such an idealized model for the beam applies only when the focusing forces are linear.

After numerous manipulations by non-linear elements, the edges of the ellipse in phase space may develop indistinct edges. For example, the ellipse containing ∼85% of the bunch may be significantly smaller than the ellipse containing 100% of the bunch [13]. Additionally, the phase space distribution may not retain an elliptical shape. To this end, emittance is often quoted as the area of an ellipse containing some percentage of the beam. The percentage chosen depends on the particles of the bunch and applications of the beam. Typically for

electrons, and throughout this document, root mean square (*rms*) emittances are calculated and quoted. This term has multiple definitions in accelerator literature and is ambiguous. In this document, quoted values for simulation results use the unnormalized Sacherer *rms* emittance, which is defined by

$$\epsilon_{x,rms} = \sqrt{\sigma_x^2 \sigma_{x'}^2 - \sigma_{xx'}^2}, \tag{29}$$

where $\sigma_x \equiv \sqrt{\langle x^2 \rangle - \langle x \rangle^2}$, $\sigma_{x'} \equiv \sqrt{\langle x'^2 \rangle - \langle x' \rangle^2}$, and $\sigma_{xx'} \equiv \langle xx' \rangle - \langle x \rangle \langle x' \rangle$. $\sigma_{xx'}$ represents the correlation of the transverse phase space, so when the beam is neither diverging or converging, $\sigma_{xx'} \approx 0$.

Unnormalized transverse *rms* emittance is constant when the bunch is not accelerated or deccelerated, or when it passes through a linear focusing system. The dependence of the unnormalized emittance on the energy of the beam is a consequence of the use of $\sigma_{x'}$ and $\sigma_{xx'}$ in Eq. (29), as these quantities are dependent on p_z. Consequently, even if p_x remains constant as the energy of the bunch is changed, p_z has changed, changing x'. The normalized *rms* emittance is defined to be

$$\epsilon_{x,rms}^N = \sqrt{\sigma_x^2 \sigma_{p_x}^2 - \sigma_{xp_x}^2}/mc, \tag{30}$$

which is related to the unnormalized *rms* emittance by

$$\epsilon_{x,rms}^N = \beta\gamma\epsilon_{x,rms}, \tag{31}$$

where $\gamma \equiv 1/\sqrt{1-\beta^2}$, the Lorentz factor. This normalized *rms* emittance remains constant when the energy of the bunch is altered, only changing due to non-linearities of the focusing system through which it passes. Consequently, this makes it valuable in quantifying non-linear effects in the system, such as space charge. Typical convention in accelerator literature is for a symbol similar to $\epsilon_{N,x}$ to represent $\epsilon_{x,rms}^N$, leaving the fact that the value is *rms* to be assumed by the reader. However, $\epsilon_{x,rms}^N$ is used throughout this document to be explicitly clear as to the formula definition used to calculate this parameter value.

With this more typical and convenient definition of emittance, the Twiss parameters can be calculated from a beam distribution using the formulae

$$\begin{aligned} \beta_x &= \frac{\sigma_x^2}{\epsilon_{x,rms}} \\ \alpha_x &= -\frac{\sigma_{xx'}}{\epsilon_{x,rms}} = -\frac{\beta_x'}{2} \\ \gamma_x &= \frac{\sigma_{x'}^2}{\epsilon_{x,rms}}, \end{aligned} \tag{32}$$

where $\beta_x'(s)$ is the rate of change of $\beta_x(s)$ at s along the beam trajectory. It should be noted that if any two of the above parameters have a known value, that the third can be found using the relationship $\gamma_x(s)\beta_x(s) - \alpha_x^2(s) = 1$. Thus of the three Twiss parameters, only two are independent variables, as the value of the third is constrained by the previously given relationships [28].

Space charge refers to the electrostatic forces in the beam frame that the bunch particles apply to each other. In the case where the particles all have the same charge sign (positive or negative) this force is repulsive. These forces are nonlinear and can defocus the beam. A magnetic self-field arises from taking the static electric field the bunch produces in the beam frame and Lorentz transforming it into the lab frame. For two bunches at the same energy, the one with a higher charge density is more affected by the space charge contributions. The effect tends to be more pronounced at lower velocities, as at higher velocities the space charge and magnetic self-forces typically cancel each other [13, 28].

Thus far, it has been tacitly assumed that there is no impact from metallic or magnetic surfaces near the beam. However, this is rarely a good assumption near the cathode surface, where image charge or mirror charge should be taken into account for better accuracy [13, 29, 36, 37]. Typically, when image charge is taken into account, this means that the electromagnetic effects of the image charge on the bunch are considered [13].

2.3 BUNCH COMPRESSION

Bunch compression is the process of decreasing the longitudinal length which the beam occupies. Most bunch compressor lattices are designed at a reference energy, typically the average kinetic energy of the bunch. However, all bunches have some amount of energy spread. Let the momentum of a particle with the average kinetic energy of the bunch be represented by p_0 [15]. Then the relative energy deviation, or the deviation in momentum relative to the momentum of the reference particle, is $\delta = \Delta p/p_0$ such that $\Delta p \equiv p - p_0$ for all other particles of momentum p in the bunch [13, 15]. As a bunch moves through the compressor lattice, the particles with the reference momentum follow the "ideal" trajectory. Particles either above or below this momentum follow different trajectories.

The horizontal dispersion is given by $D_x(s) = \Delta x(s)/\delta$ where $\Delta x(s)$ is the horizontal offset a particle with relative energy deviation δ experiences from the ideal trajectory given by a particle with the reference momentum ($\delta = 0$). The rate of change of horizontal dispersion with respect to the beam path is represented by D_x'. Vertical dispersion is similarly defined, for a vertical displacement instead of the horizontal. When a beam is bent in the horizontal

plane, only horizontal dispersion is created. For a compression lattice which bends the beam in a horizontal direction, it is said to be an achromat if at the entrance and exit $D_x, D'_x = 0$.

A chirped bunch is one in which a correlation exists between the longitudinal position and δ for the particles within the bunch. When the head of the bunch has the lowest energy, then the bunch is said to be negatively chirped. A positively chirped bunch has the lowest energy at the tail of the bunch [15]. An example of a chirped bunch is shown in Fig. 3, which is positively chirped.

R_{56}, sometimes given as M_{56}, is the element of the transfer matrix which relates a particle's relative energy deviation δ with its displacement from the center z after traveling through magnets. The momentum compaction factor α_c is given by

$$\alpha_c = \frac{1}{L_0}\int_0^{L_0} \frac{D_x(s)}{\rho(s)} ds = \langle \frac{D_x(s)}{\rho} \rangle \tag{33}$$

where $L_0 = \int ds$ is the design path length taken by a particle with the reference momentum ($\delta = 0$) and ρ is the bending radius. The bending radius is given by $\rho = p_0/(eB)$, where p_0 is the momentum of the particle, e is the electric charge, and B is the magnetic field transverse to the motion of the particle. R_{56} is then given by

$$R_{56} = L_0 \alpha_c. \tag{34}$$

For a given bunch, there exists a specific value of R_{56} which, to first order, translates into an optimally compressed beam. If the R_{56} is larger or smaller than this value, the beam which exits the compressor is either over- or under-compressed, respectively. For an identical bunch entering the compressor, the longitudinal phase spaces of the exiting bunch are shown for three different R_{56} values in Fig. 5. While the bunch which traveled the $R_{56} = 1.6$ m compressor has an approximately vertical longitudinal phase space, the compressors with greater or smaller values of R_{56} produce a skewed phase space. For these cases, the bunch is over- or under-compressed, respectively [13, 15].

The betatron phase advance between locations s_a and s_b is

$$\phi(s_a) - \phi(s_b) = \int_{s_b}^{s_a} \frac{1}{\beta(s)} ds \tag{35}$$

where $\beta(s)$ is the beta function of the beam at location s given by Eq. (32). The beta function used in this integral is the one that corresponds to the bending plane of the compressor [15]. For details on the betatron phase and its origin from the phase-amplitude solution to the transverse equations of motion, the reader is directed to Chapter 2 of [15].

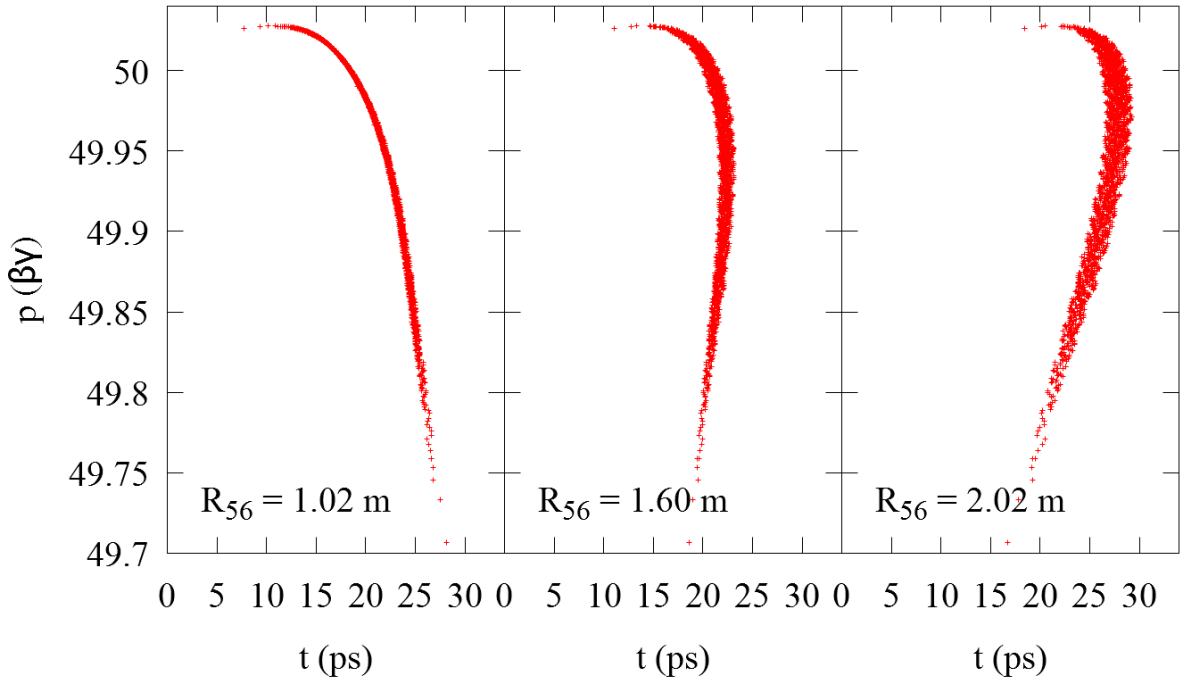

FIG. 5: The longitudinal phase spaces of bunches exiting compressors of different R_{56} values, resulting in a bunch which is under compressed (left), optimally compressed (center), and over compressed (right).

2.4 DIPOLE RADIATION

When the beam electrons interact with the incident laser field in an inverse Compton source, they are accelerated. This acceleration leads the particles to radiate electromagnetic fields. Because the acceleration is mainly in one direction normal to the beam motion and the appropriate approximations apply, the distribution of the radiated photons is well-described by dipole emission, which is now briefly reviewed.

The source-free Maxwell equations have plane-wave solutions of the form

$$\begin{aligned} \mathbf{E}(x,y,z,t) &= \hat{\varepsilon} E_0 \sin(\mathbf{k}\cdot\mathbf{x} - \omega t) \\ \mathbf{B}(x,y,z,t) &= \hat{k} \times \hat{\varepsilon} (E_0/c) \sin(\mathbf{k}\cdot\mathbf{x} - \omega t), \end{aligned} \tag{36}$$

where $\hat{\varepsilon}$ is the unit vector describing the polarization, E_0 is the amplitude of the electric field, $\mathbf{k}$ is the propagation vector, $\hat{k} \equiv \mathbf{k}/|\mathbf{k}|$, and the wave angular frequency is given in vacuum by $\omega = |\mathbf{k}|c$. For propagation in vacuum $\hat{k}\cdot\hat{\varepsilon} = 0$. The energy density and intensity (Poynting vector) of the plane wave, averaged over a wavelength are

$$U = \frac{\varepsilon_0}{2} E_0^2 \tag{37}$$

and

$$\mathbf{S} = \frac{1}{\mu_0} \mathbf{E} \times \mathbf{B} = \frac{c\varepsilon_0 E_0^2}{2} \hat{k}, \tag{38}$$

respectively.

Solving for the non-relativistic motion of an electron near the origin ($x = 0, y = 0, z = 0$) excited by a plane wave of a single frequency, the motion is given by

$$\mathbf{x}(t) = \hat{\varepsilon} \frac{eE_0}{m\omega^2} \sin\omega t = \hat{\varepsilon} a_0 \frac{c}{\omega} \sin\omega t, \tag{39}$$

where the important parameter, the unit-free field strength

$$a_0 = \frac{eE_0\lambda}{2\pi mc^2} \tag{40}$$

is introduced, with λ being the wavelength. For $a_0 \ll 1$ the normalized velocity satisfies $\beta(t) \ll 1$ and the non-relativistic approximation applies.

Now specialize to the case that the incident plane wave propagates along the negative z-axis and the wave is polarized along the x-axis. In this case the electron motion is

$$\begin{aligned} x(t) &= a_0 \frac{c}{\omega} \sin\omega t \\ y(t) &= 0 \\ z(t) &= 0. \end{aligned} \tag{41}$$

To calculate the electromagnetic radiation emitted by the accelerating electron, let us introduce the scalar and vector potentials with the definitions

$$\begin{aligned} \mathbf{E} &= -\boldsymbol{\nabla}\phi - \frac{\partial \mathbf{A}}{\partial t} \\ \mathbf{B} &= \boldsymbol{\nabla}\times\mathbf{A}. \end{aligned} \tag{42}$$

In the Lorenz gauge, the potentials satisfy the inhomogeneous wave equations

$$\begin{aligned} \Box\phi(\mathbf{x},t) &= \left[\nabla^2 - \frac{\partial^2}{c^2\partial t^2}\right]\phi(\mathbf{x},t) = -\frac{\rho(\mathbf{x},t)}{\varepsilon_0} \\ \Box\mathbf{A}(\mathbf{x},t) &= \left[\nabla^2 - \frac{\partial^2}{c^2\partial t^2}\right]\mathbf{A}(\mathbf{x},t) = -\mu_0\mathbf{J}. \end{aligned} \tag{43}$$

Applying the retarded solution to the wave equation for a point particle undergoing a motion $\mathbf{r}(t) = d(t)\hat{x}$ yields

$$\begin{aligned} \phi(\mathbf{x},t) &= \frac{e}{4\pi\varepsilon_0}\int \frac{\delta(t'-t+R/c)}{R}dt' = \frac{e}{8\pi^2\varepsilon_0}\iint \frac{e^{i\omega(t'-t+R/c)}}{R}d\omega dt' \\ A_x(\mathbf{x},t) &= \frac{\mu_0 e}{4\pi}\frac{\dot{d}(t')\delta(t'-t+R/c)}{R}dt' = \frac{\mu_0 e}{8\pi^2}\iint \frac{\dot{d}(t')e^{i\omega(t'-t+R/c)}}{R}d\omega dt' \end{aligned} \tag{44}$$

where $R^2 = (x-d(t))^2 + y^2 + z^2$. By performing the required derivatives, imposing the non-relativistic approximation, and passing into the far field limit gives

$$\begin{aligned} \mathbf{B}(\mathbf{x},t) &\approx \frac{\mu_0 e}{4\pi c r}\ddot{d}(t-r/c)\hat{x}\times\mathbf{n} \\ \mathbf{E}(\mathbf{x},t) &\approx \frac{\mu_0 e}{4\pi r}\ddot{d}(t-r/c)\mathbf{n}\times(\mathbf{n}\times\hat{x}) \end{aligned} \tag{45}$$

where now $r^2 = x^2+y^2+z^2$ and $\mathbf{n} \equiv \mathbf{x}/r$. Referring to Fig. 6, this result is

$$\begin{aligned} \mathbf{B}(\mathbf{x},t) &\approx \frac{\mu_0 e}{4\pi c r}\ddot{d}(t-r/c)\sin\Theta\ \hat{\Phi} \\ \mathbf{E}(\mathbf{x},t) &\approx \frac{\mu_0 e}{4\pi r}\ddot{d}(t-r/c)\sin\Theta\ \hat{\Theta} \end{aligned} \tag{46}$$

where Θ is the angle between the acceleration and the propagation direction. By calculating the Poynting vector, the intensity per unit solid angle is

$$\frac{dI}{d\Omega} = \frac{e^2}{16\pi^2\varepsilon_0 c^3}\ddot{d}^2(t-r/c)\sin^2\Theta. \tag{47}$$

It displays, through the $\sin^2\Theta$ factor, the characteristic dipole radiation pattern [29]. There is no radiation emitted along the direction of motion, and radiation intensity is maximum in the direction normal to the particle motion. Defining Fourier transforms as

$$\begin{aligned} \tilde{d}(\omega) &= \int d(t)e^{-i\omega t}dt \\ d(t) &= \frac{1}{2\pi}\int \tilde{d}(\omega)e^{i\omega t}d\omega \end{aligned} \tag{48}$$

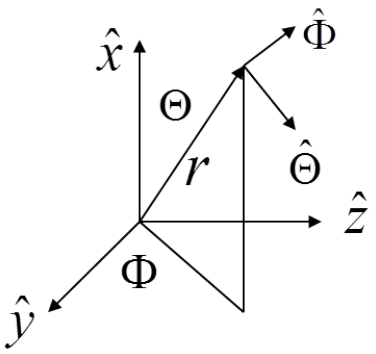

FIG. 6: Spherical coordinate system.

and applying Parseval's theorem of the theory of Fourier transforms allows the energy spectrum to be evaluated. Letting U_γ denote the energy radiated, the energy spectrum is

$$\frac{dU_\gamma}{d\omega d\Omega} = \frac{e^2\omega^4}{32\pi^3\varepsilon_0 c^3}|\tilde{d}(\omega)|^2 \sin^2\Theta. \tag{49}$$

Using Eq. (39) as the result for the motion at a given frequency, superposing, and introducing the classical electron radius $r_e = e^2/4\pi\varepsilon_0 mc^2$ and $d = eE/m\omega^2$ this expression becomes

$$\frac{dU_\gamma}{d\omega d\Omega} = \frac{\varepsilon_0 c r_e^2}{2\pi}|\tilde{E}(\omega)|^2 \sin^2\Theta. \tag{50}$$

Therefore, the spectra radiated in any particular direction have identical shapes proportional to $|\tilde{E}(\omega)|^2$, but their overall strength is modulated by the dipole radiation pattern.

This same calculation method can be used to calculate the radiation from a moving electron stimulated by an incident laser. Simply transform the incident laser plane wave into the electron rest frame, calculated the emitted spectrum as above, and Lorentz transform back into the lab frame. The result is found in [12] and is

$$\frac{dU_\gamma}{d\omega d\Omega} = \frac{\varepsilon_0 c r_e^2}{2\pi}|\tilde{E}\left[\omega(1-\beta\cos\theta)/(1+\beta)\right]|^2 \frac{\sin^2\phi(1-\beta\cos\theta)^2 + \cos^2\phi(\beta-\cos\theta)^2}{\gamma^2(1-\beta\cos\theta)^4}. \tag{51}$$

Proper relativistic Doppler shifting is accounted by changing the argument of the Fourier transform and the final ratio in this expression is the result of properly Lorentz transforming the solid angle and dipole radiation pattern.

2.5 PHYSICS OF COMPTON SCATTERING

The process of scattering a photon off an electron at rest is known as both Thomson scattering, at lower photon energies, and Compton scattering, at higher photon energies.

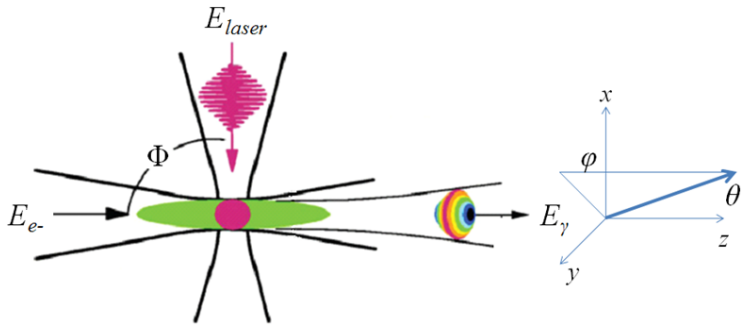

FIG. 7: Diagram of inverse scattering geometry with angles denoted.

The term inverse Compton scattering (ICS) is used in the situation such that the electron loses energy to the incident photons. A diagram of the scattering process is shown in Fig. 7. In the diagram and following formulae, Φ is the angle between the relativistic electron and the laser beams, and $\Delta\Theta$ is the angle between the laser beam and scattered photons. If θ and ϕ represent spherical polar angles that the scattered photons make in the coordinate system such that the electron beam moves along the z axis, then the angle $\Delta\Theta$ is $\cos\Delta\Theta = \cos\Phi\cos\theta - \sin\Phi\sin\theta\cos\phi$. The coordinate system is set so the interaction point (IP) of the electron and laser beams occurs in the $x - z$ plane.

A general formula expressing the energy of a scattered photon in the lab frame, E_γ, as a function of the direction of the scattered photon, is

$$E_\gamma(\Phi,\theta,\phi) = \frac{E_{laser}(1-\beta\cos\Phi)}{1-\beta\cos\theta + E_{laser}(1-\cos\Delta\Theta)/E_{e^-}} \tag{52}$$

where β is the relativistic factor equal to v_z/c, E_{laser} is the energy of the laser beam, and $E_{e^-} = \gamma m_e c^2$ is the energy of the electron [12]. This formula includes the impact of electron recoil. The Thomson formula is a good approximation if the electron recoil is negligible, i.e. the energy of the laser in the beam frame is much less than the rest mass of the electron. When this is true, then the formula for the energy of the scattered photon becomes

$$E_\gamma(\Phi,\theta) \approx E_{laser}\frac{1-\beta\cos\Phi}{1-\beta\cos\theta}. \tag{53}$$

Assuming $\gamma \gg 1$ and $\theta \ll 1$, it can also be approximated as

$$E_\gamma(\Phi,\theta) \approx \frac{2\gamma^2 E_{laser}(1-\cos\Phi)}{1+\gamma^2\theta^2}, \tag{54}$$

where γ is the usual relativistic factor for the electron.

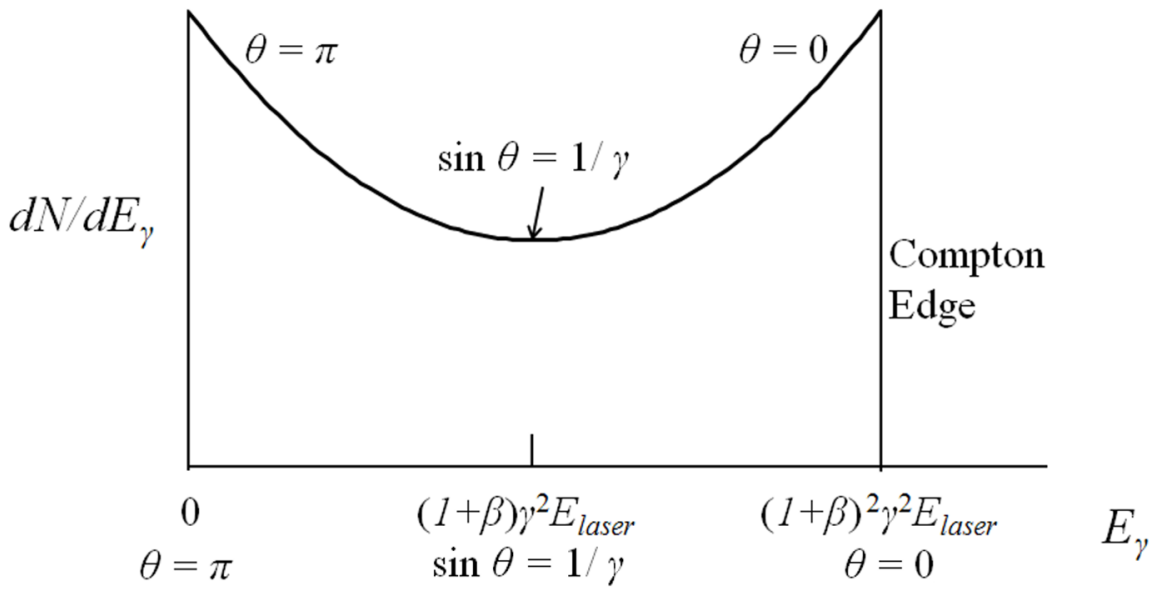

FIG. 8: Number density of scattered photons as a function of the energy of scattered photons.

Consider the situation of a head-on collision between the electron and the laser ($\Phi = \pi$). The energy of the laser in the beam frame is $E'_{laser} = \gamma(1+\beta)E_{laser}$. Assuming that the Thomson formula is a good approximation, i.e. $E'_{laser} \ll mc^2$ is true, then the energy of the scattered photon is also E'_{laser} in the beam frame. Going back into the lab frame, the photons scattered in the forward (positive z) direction have the highest energy, which is $\gamma^2(1+\beta)^2 E_{laser} \approx 4\gamma^2 E_{laser}$. The high energy boundary of emission is called the Compton edge; no radiation is emitted at higher energies. For photons scattered at the angle θ such that $\sin\theta = 1/\gamma$ ($1/\gamma \ll 1$), the energy decreases to $2\gamma^2 E_{laser}$, which is also the average energy of the scattered photons. Both the Compton edge and the number density of scattered photons as a function of the energy of scattered photons can be seen in Fig. 8. For the case of side-scattering ($\Phi = \pi/2$), the scattered photons with the highest energy is slightly removed from the z axis.

The number of photons produced by scattering an incident laser off an electron is proportional to the time-integrated intensity of illumination. Consequently, the total photon yield is proportional to the square of the field strength, as in the case of undulator radiation. Progressing by the analogy with undulator radiation, the field strength parameter for a plane wave incident laser is defined to be

$$a = \frac{eE\lambda_{laser}}{2\pi mc^2}, \tag{55}$$

where e is the electron charge, E is the transverse electric field of the laser, λ_{laser} is the laser wavelength, and mc^2 is the rest energy of the electron. This value quantifies the normalized transverse vector potential for the EM field accelerating the electrons during scattering. For Compton scattering, a plays a role similar to that of K in the field of undulators. For the case of $a \ll 1$, the backscattering is in the linear regime, an assumption that continues as formulae are presented.

If we take the assumption that the transverse intensity distributions of the laser and electron beams are round Gaussian distributions with the *rms* sizes of σ_e and σ_{laser} respectively, then

$$U_\gamma = \gamma^2(1+\beta)\sigma_T \frac{N_e N_{laser}}{2\pi(\sigma_e^2 + \sigma_{laser}^2)} E_{laser}, \tag{56}$$

where U_γ is the total energy of the scattered photons, N_e is the number of electrons in the bunch, N_{laser} the number of photons in the incident laser, and σ_T is the Thomson cross section $8\pi r_e^2/3$, where r_e is the classical electron radius [12, 38, 39]. The classical electron radius is defined as $r_e = e^2/4\pi\epsilon_0 mc^2$, where e is the electric charge of the electron, ϵ_0 is the permittivity of free space, m is the mass of the electron, c is the speed of light [29]. From this formula, the total number of scattered photons N_γ is

$$N_\gamma = \sigma_T \frac{N_e N_{laser}}{2\pi(\sigma_e^2 + \sigma_{laser}^2)}. \tag{57}$$

In the limit of $\sigma_e \ll \sigma_{laser}$, under the assumption that the incident laser is a flat pulse, the number of the scattered photons per electron is

$$N_{pere^-} = \frac{2\pi\alpha N_\lambda a^2}{3} \tag{58}$$

where α is the fine-structure constant and N_λ is the number of wavelengths in the incident pulse.

Given that the spectral energy density of the scattered photons may be analytically computed in the linear Thomson backscatter limit, it can further be determined that the number of scattered photons within a 0.1% bandwidth at the Compton edge is $N_{0.1\%} = 1.5 \times 10^{-3} N_\gamma$. Consequently, the rate of photons (flux) into this bandwidth is $\mathcal{F}_{0.1\%} = 1.5 \times 10^{-3} \dot{N}_\gamma$. For high-frequency repetitive sources, $\dot{N}_\gamma = f N_\gamma$, where f is the repetition rate.

There exists a number of causes for X-ray energy spread in the bunch of scattered photons. The ones to be addressed here include energy spread in the electron and laser beams and the finite width of apertures defining the experiment acceptance. Energy spread due to finite width of the apertures is minimized in the forward direction, which is a typical location

for experiments to be set up. The contribution to the relative energy spread of the scattered photons due to the electron beam energy spread is $2\sigma_{E_{e^-}}/E_{e^-}$, where $\sigma_{E_{e^-}}$ is the *rms* energy spread of the electron beam. The contribution to the energy spread of the scattered photons due to the linewidth of the laser is simply equal to the relative laser linewidth. The contribution due to the specific opening angle can be found by using the angle and the energy curve to determine the energy spread possible through an aperture of that angle. The final contribution to be addressed here is that of the finite opening angle. Off-center electrons in the beam may pass through the collision region. Typically, these electrons have nonzero values of transverse momenta, afterwards moving at angle with respect to the forward direction. Electrons traveling along this angle will have a lower energy than the forward-moving electrons, when Doppler-shifted into the beam frame. Referred to as emittance-generated energy spread, it can be estimated using

$$\frac{\sigma_{E_\lambda}}{E_\lambda} = \frac{2\gamma^2\epsilon}{\beta_{e^-}}, \tag{59}$$

where ϵ is the average transverse unnormalized emittance of the electron beam at the IP and β_{e^-} is the beta function of the electron beam at the IP.

The pulse length of the scattered photons in the forward direction of the backscattering arrangement is equal to the pulse length of the electron bunch within corrections on the order of $\mathcal{O}(1/\gamma^2)$. There is no longitudinal spreading possible as both the electron bunch and the scattered radiation move in the same direction and at the velocity of light (photons) and nearly the velocity of light (electrons).

The general definition for the spectral brilliance of a beam is given by

$$\mathcal{B} = \frac{\mathcal{F}_{0.1\%}}{4\pi^2\sigma_x\sigma_{x'}\sigma_y\sigma_{y'}}, \tag{60}$$

where σ_x and σ_y are the *rms* transverse sizes of the beam and $\sigma_{x'}$ and $\sigma_{y'}$ are the *rms* transverse angular sizes of the beam. However, by taking advantage of the analogy to undulator radiation, it is possible to approximate the brilliance of the scattered photons using the parameters of the electron beam at the collision. The standard approximation is $\sigma_{x'} \approx \sqrt{\epsilon_x/\beta_x + \lambda/2L}$, where ϵ_x is the *rms* unnormalized horizontal emittance, β_x is the horizontal beta function, λ is the emitted wavelength, and L is the effective length of the source. This result assumes the X-ray beam angular sizes are a combination of the intrinsic beam angles and radiation diffraction, which is quantified by $\lambda/2L$. Taking this approximation into account, Eq. (60) becomes

$$\mathcal{B} = \frac{\mathcal{F}_{0.1\%}}{4\pi^2\sqrt{\beta_x\epsilon_x}\sqrt{\epsilon_x/\beta_x + \lambda/2L}\sqrt{\beta_y\epsilon_y}\sqrt{\epsilon_y/\beta_y + \lambda/2L}}. \tag{61}$$

For free electron laser (FEL) applications, the *rms* unnormalized emittance required from the electron beam to achieve the diffraction limit is $\epsilon_{x,y} < \lambda/4\pi$, which is not typically achievable for lower energy electron beams, as the lower energy means that the *rms* unnormalized emittance is much larger [12, 38, 39]. For a non-diffraction limited source such as this one, $\epsilon_{x,y} > \lambda/4\pi$, implying that the decrease in brilliance for the photon source due to $\lambda/2L$ terms is negligible [15]. With this in mind, the brightness in such a non-diffraction limited mode of operation is

$$\mathcal{B} \approx \frac{\mathcal{F}_{0.1\%}}{4\pi^2 \epsilon_x \epsilon_y}. \tag{62}$$

Scattering results are simulated by applying the Monte Carlo method to distributions in an electron bunch and incident laser pulse. Consequently, scattered photons are generated conforming to the initial distributions and the differential scattering cross section. These scattered photons yield a distribution at some given location. Though impossible to generate the number of electrons and photons present in typical Compton sources, certain approximations allow for reduced numbers of particles to yield reasonably accurate results. There already exist codes with a high level of accuracy that quantitatively predict the scattered photons when in the linear or low-intensity scattering regimes. As the majority of both existing and prospective systems reside in the linear regime, accurate simulations for non-ideal electron bunch distributions may be made. These simulations take into account such effects as longitudinal pulsing and electron pulse length effects, transverse profiles in the electron and incident laser beams, hourglass effects, and three-dimensional diagnostics for the scattered radiation [12, 38–40].

2.6 CONSIDERATIONS FOR THIS PROJECT

The ultimate goal of this project is to simulate a machine design that produces an electron beam such that when it is scattered off a laser at the IP, the specifications given in Table 5 are met by the X-ray beam produced. However, it is more convenient through much of the design process to evaluate possible systems by how closely the simulated electron beam produced matched the values contained in Table 3. Toward finalizing of the design, the estimated X-ray beam parameters are determined by assuming an incident laser meeting the specifications in Table 4 and by calculating the X-ray flux and brilliance.

Two issues should be mentioned, before moving on to the design of the system. First is that, even with the rapid advancement of laser technology in recent years and claims that the existence of such a laser meeting the parameters in Table 4 would be a reasonable assumption, such a stable optical cavity does not currently exist [1, 12, 14]. A second concern is that the

formulae that have been given and used for estimates may not rigorously apply, e.g., the electron beam at the IP does not have a Gaussian distribution. As previously mentioned, there already exist codes to simulate the scattered X-ray beam, given arbitrary distributions of both the electron and incident laser beams. These codes are highly accurate for linear or low-intensity scattering, i.e. $a \ll 1$, so use of these codes yields more accurate estimations of the resulting X-ray source than those from formulae assuming idealized beams.

Initially during the ICLS design process, the project was divided into four sections, with frequent communication between the separate groups dealing with the sections. The sections were: (1) design the SRF electron gun, (2) design the spoke cavity (a number of which make up the linac), (3) tracking of an electron bunch through the gun and linac, and (4) the tracking of that bunch through a designed system of magnets (i.e. the bunch compressor and final focusing). As the project progressed, all aspects became the responsibility of the author. Effort by previous contributors will be appropriately credited and acknowledged throughout the document.

CHAPTER 3

SIMULATION CODES AND CONSIDERATIONS

3.1 SIMULATION CODES

The entirety of this work is the product of evaluating results generated by various simulation calculations. Consequently, confidence that the generated results are sufficiently accurate and not the product of simulation artifacts is desired. Additionally, a start-to-end calculation is desired. Thus the simulated bunch cannot change as it passes from one code to a different one and the results of one code must be correctly used by another.

3.1.1 CST MICROWAVE STUDIO

Computer Simulation Technology (CST) is the developer of the 2012 CST Microwave Studio® (CST MWS) software package, which is a three-dimensional (3D) electromagnetic (EM) solver. Using this code, it is possible to construct an RF structure, then solve for the eigenmodes, RF properties, and 3D EM fields of that structure [34].

One of the more critical considerations when applying the solver to a structure is the type and size of the mesh. If the mesh is not fine enough to accurately represent the structure, the validity of the results is debatable. If the mesh is too fine, the run time for the solver increases significantly and the number of computations may introduce error into the result. Additionally, a balance must be struck between mesh size of the solver and the output grid step size of the EM fields; there should not be more than a single grid point within a given mesh cell.

An appropriate means to determine the proper mesh and grid sizes is that reducing the step size does not change the tracking simulation results for a set electron bunch and physical layout, and the change in step size merely increases the solve time or the output file size, respectively.

3.1.2 SUPERFISH

The Poisson Superfish collection of programs is developed and supported by the Los Alamos Accelerator Code Group. These programs calculate the static magnetic and electric

fields, as well as RF EM fields in either 2D Cartesian coordinates or axially symmetric cylindrical coordinates. Superfish is intended to handle RF cavity and waveguide problems, which is the focus here. The most recent version of 7.19 was published on 18 October 2013 [33].

The considerations and criteria for solver mesh and output grid sizes are the same as for CST MWS. While the spoke cavities that constitute the linear accelerator (linac) cannot be modeled with Superfish, the superconducting radio-frequency (SRF) injector gun is axially symmetric, allowing it to be fully modeled by Superfish.

3.1.3 *ASTRA*

Developed at DESY, the Astra (**A** **S**pace Charge **Tr**acking **A**lgorithm) software package consists of five programs which can be used collectively to generate a particle bunch (*generator*), track the bunch particles through user defined fields (*Astra*), display EM fields of beam line elements and particle distributions (*fieldplot*), display phase space plots (*postpro*), and display beam parameters as a function of longitudinal beam line position (*lineplot*). The most recent version of 3.1 was published in April 2014 and is used for this work.

The program *Astra* within the Astra package is the code which tracks the particle bunch through user defined external EM fields as well as internal EM fields due to space charge. *Astra* is a 6D code, meaning that each "macroparticle" is defined using six coordinates. For a macroparticle, the charge is not set by the particle species. Instead, it is set by the user-set bunch charge and number of particles used to calculate the tracking. Consequently, the beam does not have to be assumed to be axially symmetric through the tracking, which is necessary to accurately track a bunch through a cavity without this constraint. The bunch particles are tracked by applying a non-adaptive Runge-Kutta integration of 4^{th} order to the general equations of motion [37].

There are two primary areas of concern regarding the accuracy of this code. The first is the range of allowed time steps used in the Runge-Kutta integration. The time step used by *Astra* is contained within the range given by H_min and H_max, which are defined by the user. H_min is the smallest allowed value for the time step of the Runge-Kutta integration, and H_max is the largest allowed value for the time step. If H_min or H_max are too small or large, respectively, then the integration is inaccurate, as are the results. In order to determine that H_max is not too large, it is sufficient to check for warning messages produced by *Astra* when the program is executed and that simulation results converge for decreasing values of H_max. H_min is too small if the tracking results are dependent upon

it. At that point, the integration time step is so small that it generates numerical noise, giving inaccurate results. Overall, these concerns and approaches are typical for accurate Runge-Kutta integrations [37, 41].

Astra has two methods to calculate space charge, the second accuracy concern. The one used in the SRF gun region is to calculate with the cylindrical grid algorithm. The user defines the number of longitudinal grid cells and rings concentric to the bunch, to which the program adds two rings and four longitudinal slices outside of the bunch. After *Astra* Lorentz translates the grid system into the bunch frame (i.e., average rest system of the bunch), the program numerically integrates over the rings. Field contributions from each ring are summed up at the center point of each grid cell. The space charge field between center points is provided by a cubic spline interpolation of adjacent center points.

The other method, used in the linac tracking, is for the code to interpolate using the 3D fast Fourier transform (FFT) algorithm [37]. The FFT algorithm is a method of calculating the constants of the interpolating trigonometric polynomial of a data set. By using the FFT algorithm instead of a direct computation, the number of operations required for an interpolation is significantly decreased. For example, a data set with 8 (2^3) points requires 48 operations using the FFT algorithm and 120 using direct computation. For a data set with 1024 (2^{10}) points, interpolation using the FFT algorithm requires ~13,300 operations while the direct computation requires ~4,200,000. The error and run time of an interpolation scales with the number of operations required to interpolate a data set. Consequently, use of the FFT algorithm is attractive for more quickly attaining a more accurate result [41].

The number of grid lines for each dimension is set by the user, with the restriction that the number be equal to 2^n for $n = 1, 2, 3, ...$ for the FFT method to apply. The user also sets the number of empty boundary cells, to allow for a balance between computational time and statistical noise in the result. As before, the grid is Lorentz translated into the bunch frame, and a constant charge density within each cell is assumed [37]. *Astra* solves the 3D Poisson equation in this frame with an analytical Green function method which is computed using a FFT. A more detailed explanation of this approach is described in [36]. Having solved the space charge fields at the grid cell centers in the bunch frame, *Astra* Lorentz transforms these fields into the lab frame. The space charge fields between these center points is provided by a linear interpolation of adjacent center points. As this interpolation is linear rather than cubic spline, the a finer grid may have to be used to produce accurate results when using this method.

For both cases, a new space charge field is not calculated at each Runge-Kutta time step.

Instead, the space charge field is calculated at some time step. For a subsequent time step, this field is scaled by the change in the bunch between the two steps. Changes in the bunch are considered for such attributes as energy, *rms* size in all directions, and aspect ratio of the beam. The user may set a limit on how much this calculated field may be scaled. Once the scale falls outside of this defined range, a new space charge field is calculated from the particle distribution. The user may also set a limit on how much particles may move within a single time step. In order to fulfill this constraint, the time step may be decreased.

For the emission of particles from the cathode using the 2D axially symmetric grid, the space charge field is not scaled at subsequent time steps. Instead, the field is calculated at each time step. Between subsequent time steps, particles are introduced to the bunch (emitted from the cathode) at intervals set by the user-defined longitudinal distribution. Consequently, the total bunch charge of the distribution changes at each interval, until the entire bunch has been emitted from the cathode. At each interval, the space charge field seen by emitted particles is the space charge field of the previous time step (not interval), scaled for the difference in bunch charge. The initial number of longitudinal slices and rings is reduced from the user supplied numbers if necessary, in order to limit the minimum size of the grid cell dimensions. In this case, the number of both grid defining properties is smoothly increased as the number of emitted particles increases. The image or mirror charge in the cathode is included by default. This contribution to the space charge field is neglected once the contribution falls below 1% at both the center and tail of the bunch. This option can be turned off and is only available for the 2D grid. Radiation and retarded time effects are not included [37].

3.1.4 IMPACT-T

IMPACT-T is a 6D accelerator simulation code, developed at Lawrence Berkeley National Laboratory (LBNL). The beta version 1.7 released on 15 September 2013 is used for this work. This code tracks a distribution of particles through a desired beamline, while including a number of additional collective effects, the most relevant to this project being space charge fields.

Similarly to *Astra*, IMPACT-T creates a user-defined distribution of macroparticles to track through the beamline. Alternatively, a distribution can be read in from a suitably formatted file. IMPACT-T tracks this distribution by solving the general equations of motion,

$$\dot{\mathbf{r}} = \frac{\mathbf{p}}{m\gamma} \tag{63}$$

$$\dot{\mathbf{p}} = q(\mathbf{E} + \frac{\mathbf{p}}{m\gamma} \times \mathbf{B}) \tag{64}$$

such that γ is the relativistic Lorentz factor as previously defined in Eq. (3); $\mathbf{p} = \gamma m\dot{\mathbf{r}}$ is the relativistic momentum; m is the rest mass of the particle; and q is the charge of the (macro)particle. The total electric and magnetic fields, $\mathbf{E}$ and $\mathbf{B}$ respectively, need to include contributions both external and internal to the bunch. The code solves these two equations using a second-order leap-frog algorithm.

As with the time step in *Astra*, the user must choose the appropriate time step when using IMPACT-T to produce accurate results. While IMPACT-T does not provide messages warning of too large a time step as *Astra* does, the method of determining the correct time step remains the same.

Once again, the accuracy of the calculated space charge field is a consideration. While the default assumption of the code is that the bunch is axially symmetric, the user can set the code to evaluate a bunch with no symmetries. In either case, IMPACT-T calculates the space charge by using the same method, which will now be explained for the 3D case.

In the input file for IMPACT-T, the user defines the number of mesh points in the x, y, and z directions. Because the code calculates the space charge field using a FFT method, this number must be 2^n for $n = 1, 2, 3, ...$ To calculate the space charge contributions at a given time step, the program superimposes the 3D grid from the mesh points onto the bunch distribution. In each cell of the grid, there exists some number of particles, thus giving the cell a total charge. The simplification is then made that the charge density within the cell is constant. Now that IMPACT-T has assigned a charge density to every cell in the grid, the program Lorentz tranforms the grid cells into the rest frame of the beam. It proceeds to solve the 3D Poisson equation with open boundary conditions by using an integrated Green function method and a 3D FFT for faster computing, fully detailed in [36]. This solution is then Lorentz transformed back into the lab frame, which yields the space charge fields in the lab frame which, with the beamline field elements, are taken into account each time step.

In order to calculate the image charge, IMPACT-T uses a shifted-Green function method, again computed by a FFT [36, 42]. The use of a shifted-Green function method instead of the standard Green function method is far more efficient, as the only fields needed are within the beam, not the entire domain contained between the bunch and the image charged particles [36]. Unlike *Astra*, the image charge is taken into account whenever the bunch charge is nonzero [36, 42].

3.1.5 ELEGANT

`elegant` (ELEctron Generation ANd Tracking) is a 6D accelerator simulation code using the Self Describing Data Sets (SDDS) file protocol with a wide variety of capabilities [43–45]. Given this scope, the focus will be on components that were directly related to this project. Both `elegant` and the SDDS Toolkit (which allows for interacting with SDDS files) are developed and supported by APS at Argonne.

The tracking in `elegant` can handle most elements that may be found in rings, linacs, and transport lines; `elegant` also allows for the analysis of SDDS files. The beam dynamic calculation is done using matrix or symplectic tracking methods. The use of `elegant` to simulate the bunch before it exits the linac is unsuitable for two reasons. First, there is no provision for space charge in `elegant` in the transverse directions, something which is critically important in this project. Second, `elegant` does not support tracking through user-defined EM field maps [43]. These needs are capably filled by *Astra* and IMPACT-T. Fortunately, the programs `astra2elegant` and `impact2elegant` easily translate the file outputs from *Astra* and IMPACT-T, respectively, into a file format that `elegant` can read. These programs are contained within the SDDS Toolkit package [46].

`elegant` capably tracks a bunch using either a file containing a distribution or a set of Twiss parameters to describe the distribution. Using the Twiss parameters to track the beam through a lattice assumes that the distribution of the particles within the bunch is idealized. Consequently, these results differ from those given for tracking an actual distribution unless the distribution exactly matches an ideal bunch distribution. Fortunately, both the tracking and optimizing functions can be used with specific particle distributions, which allows for the simulated distributions from the linac (whether from *Astra* or IMPACT-T) to be tracked through the transport line.

In addition to being able to analyze a given distribution, `elegant` also has the capability to produce output which allows for floor plans to be generated, given a transport lattice [43].

While `elegant` is capable of analyzing particle distributions contained in SDDS files, these analyses are placed into their own SDDS files. This complicates evaluations, as SDDS files are not "human-readable". While the SDDS Toolkit does have graphic capabilites, the learning curve made it quicker to translate the SDDS files into a format readable by `gnuplot`. Consequently, a number of `python` functions were written to create tab formatted text files containing the analyses of distributions [47]. Files formatted in this way are plottable by `gnuplot` [48].

3.2 START-TO-END CALCULATIONS

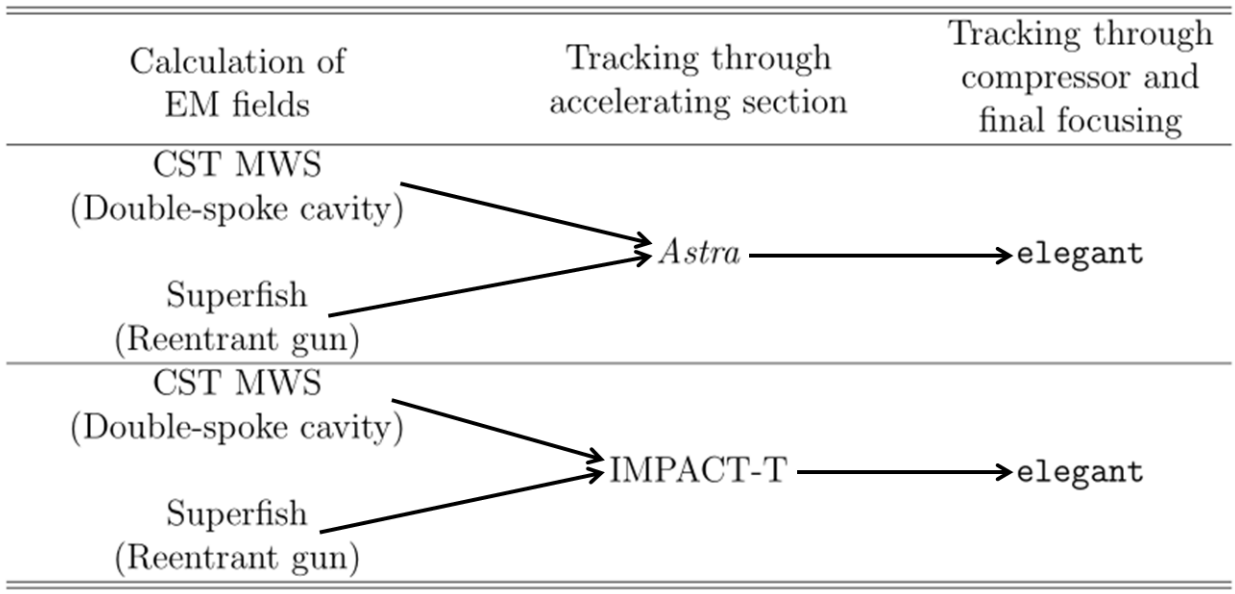

FIG. 9: Diagram of how each simulation code was used, with arrows indicating a result from one code used by another. Version 1 is on top, Versions 2 & Final on bottom.

This section consists of the details of how each simulation code was used, including the obstacles of using the output of one code as the input of another. Fig. 9 presents an overview of the dependencies and uses of the codes. Arrows between codes indicate that results from one code are used by the next downstream code. For example, CST MWS generates the EM fields of the double-spoke cavities, which in turn are used by IMPACT-T to track the macroparticles of the bunch through the linac.

As previously mentioned, the goal of start-to-end calculation includes preserving the distribution of the bunch as the particles move from one simulation code (IMPACT-T or *Astra*) to another (`elegant`), as well as an accurate representation of the EM fields in the different SRF structures to be used while simulating the acceleration of the bunch. The first objective is easily met, which was mentioned in the previous sectionn.

The second objective is more complicated. There exist four sets of possibilities: CST to *Astra*, Superfish to *Astra*, CST to IMPACT-T, and Superfish to IMPACT-T. See Appendix A for detailed output formats of CST and Superfish, input formats for *Astra* and IMPACT-T, and the `python` functions that transform one into another. However, an overview of the processes will be given here.

After designing a structure in CST, the program allows for the output of 3D EM fields into two text files, one for the E field and one for the H field. The user is prompted to pick

grid intervals for each Cartesian direction, creating a 3D grid that encloses the structure. Finally, the text file produced for a field, the E field for example, will list the coordinates (x, y, z) at a grid point and the field components found at that point (E_x, E_y, E_z). Assuming the same grid intervals are chosen for the H field, the user is left with a set of coordinates for which the EM field values $(E_x, E_y, E_z, H_x, H_y, H_z)$ are known.

A complication is that CST outputs the fields for the entire structure, though only the fields near the beam are necessary to track a bunch through a structure. In order to produce a sufficiently small output grid only covering the beam region, that small grid must be applied over the entire structure. This results in output text files which are several gigabytes in size. Files of this size either take much longer to be transformed into the proper output format or are unable to be transformed due to memory limitations. Consequently, another `python` function was written, which limits the EM field map to the entire length of the structure for a given cutoff radius, such as 1 cm. This limited EM field map is then written to two files in the same format as the CST MWS exports field data. Simulations using both *Astra* and IMPACT-T have shown that results are identical when using either the full or partial field data, as long as the bunch does not leave the region defined by the cutoff radius. At this point, transforming field data output from CST to either *Astra* or IMPACT-T is a matter of unit conversion and rearranging, which is relatively straightfoward.

Superfish is somewhat more complicated. That code allows for the field output to be restricted to a portion of the structure (such as the beamline), and outputs the cylindrial field components for both E and B on a 2D grid of radius and longitudinal position. This still provides a full 3D field map, as using Superfish results in fulfilling the axially symmetric restriction, so there is no angular dependence on the field value.

While this is sufficient for IMPACT-T, using the appropriate option, *Astra* requires the EM fields and the grid points of those fields to be 3D Cartesian. However, as can be seen in Fig. 10, projecting concentric circles onto a rectangular grid requires either a very small radius interval for the output or the interpolation of known points onto a rectangular grid. As statistical noise increasingly affects the field output for decreasing grid intervals less than a threshold, it is both more straightforward and accurate to interpolate the necessary data points.

Consequently, a `python` function was written to create the Cartesian grid and EM field data for the first quadrant $(x, y \geq 0)$, as the data for the other three quadrants are rotations of this data. To calculate the needed data points, both linear and cubic spline interpolations were tried. After the appropriate grid intervals were found for both the Superfish and

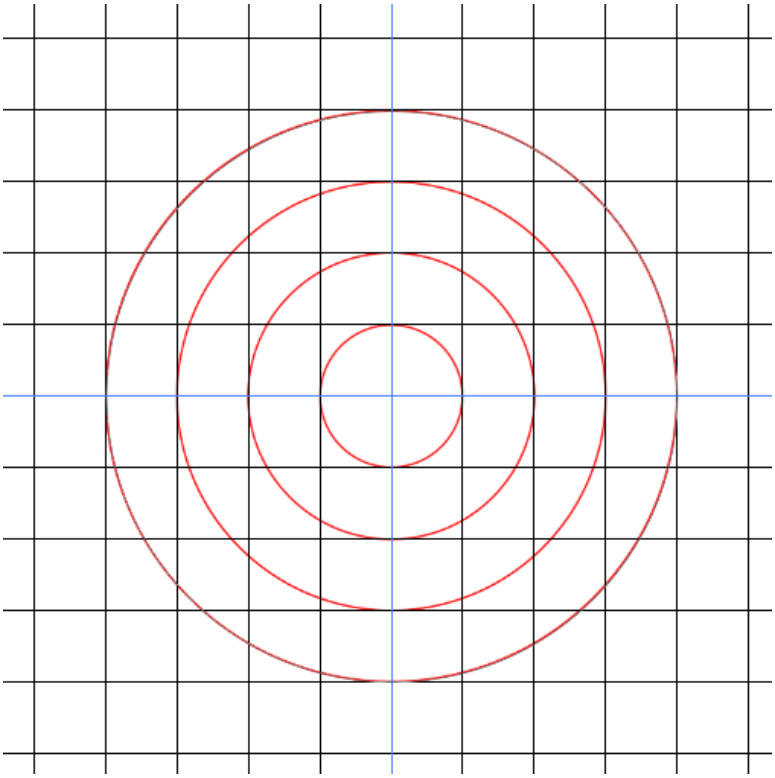

FIG. 10: Concentric circles overlaid on a rectangular grid.

Cartesian grids, the simulation results of tracking an identical bunch through either option had no significant difference. After moving to tracking with IMPACT-T, a comparison of both the original cylindrical data, linear interpolation, and cubic spline interpolation finds that the simulation results for tracking an identical bunch have no appreciable differences.

CHAPTER 4

SRF ELECTRON GUN

4.1 BACKGROUND

There exist three types of photoinjectors, or guns, presently: the DC gun, the normal conducting RF gun, and the SRF gun. While the first two types represent technology that is mature and the result of development over many decades, SRF guns are still an emerging technology [1, 16].

The concept for an SRF gun was initially published in the early 1990s [49], though more consistent publishing on the subject did not occur until nearly a decade later [50–53]. Using the idea of a reentrant cavity for an SRF gun was first presented in [50], which subsequently inspired a number of similar gun designs [16, 54]. A reentrant type cavity is significantly concave on the cavity wall which conatins the cathode aperture. Table 6 compares various SRF gun designs with each other and to the parameters desired for this project, referred to as ODU ICLS in the table. This table contains the design parameters for projects at the Naval Postgraduate School (NPS), the University of Wisconsin FEL (WiFEL), and Brookhaven National Lab (BNL).

There are two considerations that can be seen from Table 6. The first is that the bunch charge of the ODU ICLS gun is smaller than the other designs by an order of magnitude or more. The second is that the desired transverse normalized *rms* emittance is also smaller than the other designs by nearly an order of magnitude or more. As previously mentioned, the reduced bunch charge contributes to making the extremely small emittance feasible.

TABLE 6: Comparison of various SRF gun design projects.

Parameter	ODU ICLS	NPS	WiFEL	BNL	Units
Frequency	500	500	200	112	MHz
Bunch charge	0.01	1	0.2	5	nC
Trans. norm. *rms* emittance	0.1	4	0.9	3	mm-mrad

4.2 EMITTANCE COMPENSATION

It is common in RF/SRF gun design to mitigate the growth of the transverse emittance of the bunch due to space charge in order to produce a beam with the smallest emittance. Emittance compensation is the reduction of emittance due to linear space-charge forces [55, 56]. One of the most common techniques in emittance compensation is the use of a solenoid. By placing a solenoid after an injector, the goal is to manipulate the transverse phase space so that the focusing effect of the solenoid negates the defocusing effect of the space charge [55–57]. This technique is used in the three other SRF gun designs listed in Table 6 [16].

At the beginning of this project, simulations were run that modeled a bunch exiting the gun which passed through a solenoid before entering the linac. This approach to emittance compensation failed in two ways - the transverse normalized *rms* emittance was not decreased and the bunch exiting the linac was difficult to manipulate for compression and final focusing [26]. Consequently, in designing the ODU ICLS accelerator a different approach was taken which used RF focusing by altering gun geometry to provide focusing, instead of it being provided by a solenoid as in similar SRF gun designs [16]. Altering gun geometry to change produced beam properties has been done previously [50, 58].

RF focusing refers to focusing provided by the RF EM fields of the accelerating structure [28]. One example of this is shown in [58], where the RF EM fields of the gun are manipulated by recessing the cathode holder by a varying amount. In Fig. 11, two similar gun geometries are shown, with the only difference between them being the recessed cathode in the bottom right figure. In essence, this alteration to the gun geometry is to produce a radial electric field which focuses the beam. Ideally, the focusing provided will negate the defocusing produced by the space charge. However, there is a cost to this approach. As the cathode is further recessed, the radial component of the electric field (and thus the focusing) increases, but the longitudinal component (which accelerates the beam) decreases [58].

By changing the geometry of the nosecone, it is also possible to alter the EM fields within the gun. To illustrate this, two similar geometries are shown separately and at overlapping locations in Fig. 12. Selected components of the EM fields for two paths along the cavity are shown in Fig. 13. The accelerating field along the beam axis is shown for both geometries as is the radial (focusing) field along the path parallel to the beam axis at a distance of 0.5 mm.

Regardless of how the radial field is produced, there is still a balancing act that must be found between the accelerating and focusing fields. Given that increasing the focusing field decreases the accelerating one, a simplistic line of thought leads one to simply increase the operating gradient until the bunch that exits the gun is sufficiently relativistic such that

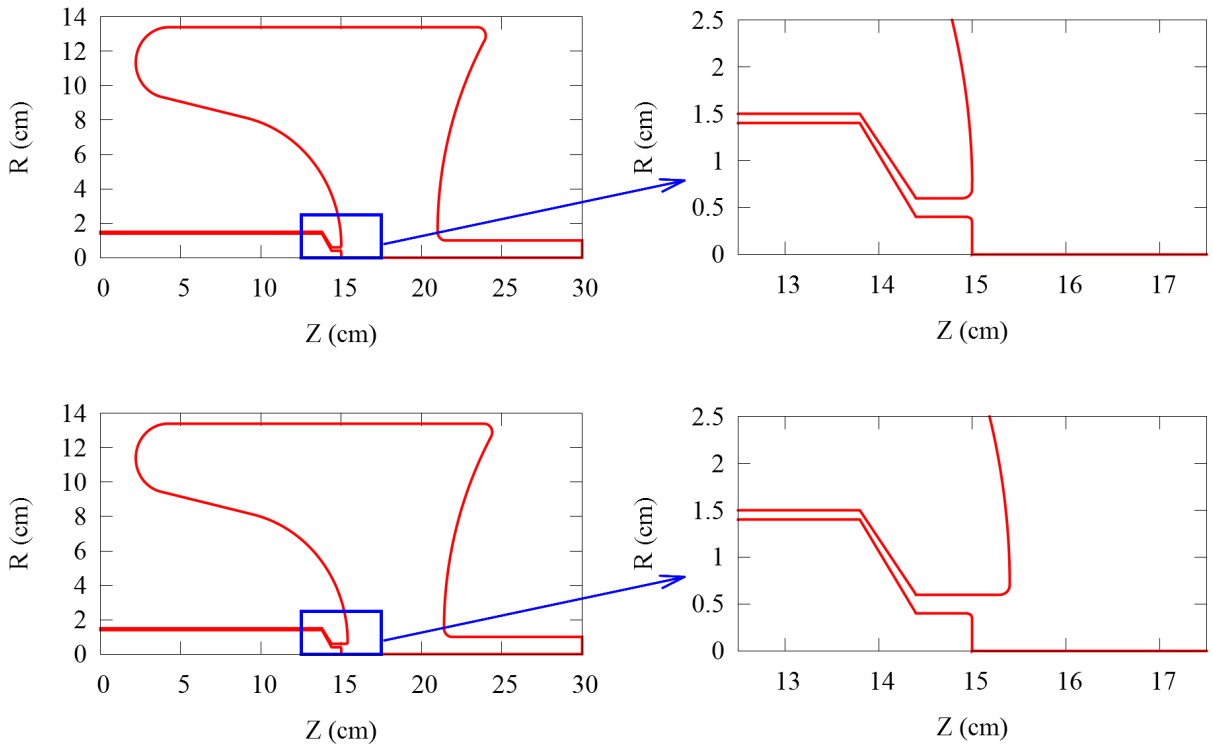

FIG. 11: Two identical gun geometries with (bottom) and without (top) a recessed cathode to provide RF focusing. Enlarged plots of the area in the blue box are shown to the right.

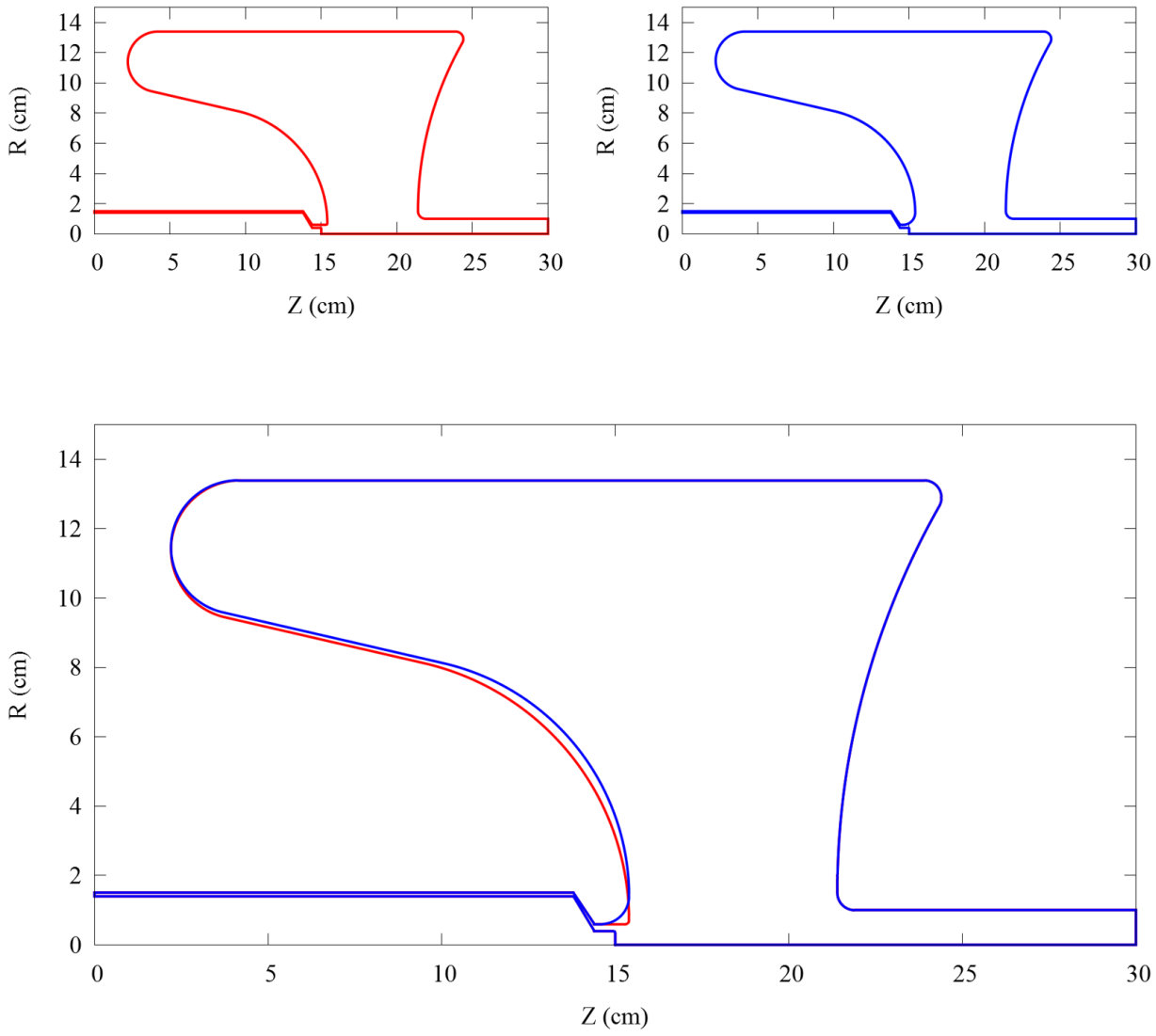

FIG. 12: Two similar geometries with differing nosecone shapes, referred to as designs A and B, are shown on the plots on the top row (left and right, respectively). The bottom row contains a plot of designs A and B overlapping, in order to emphasize the difference between the two designs.

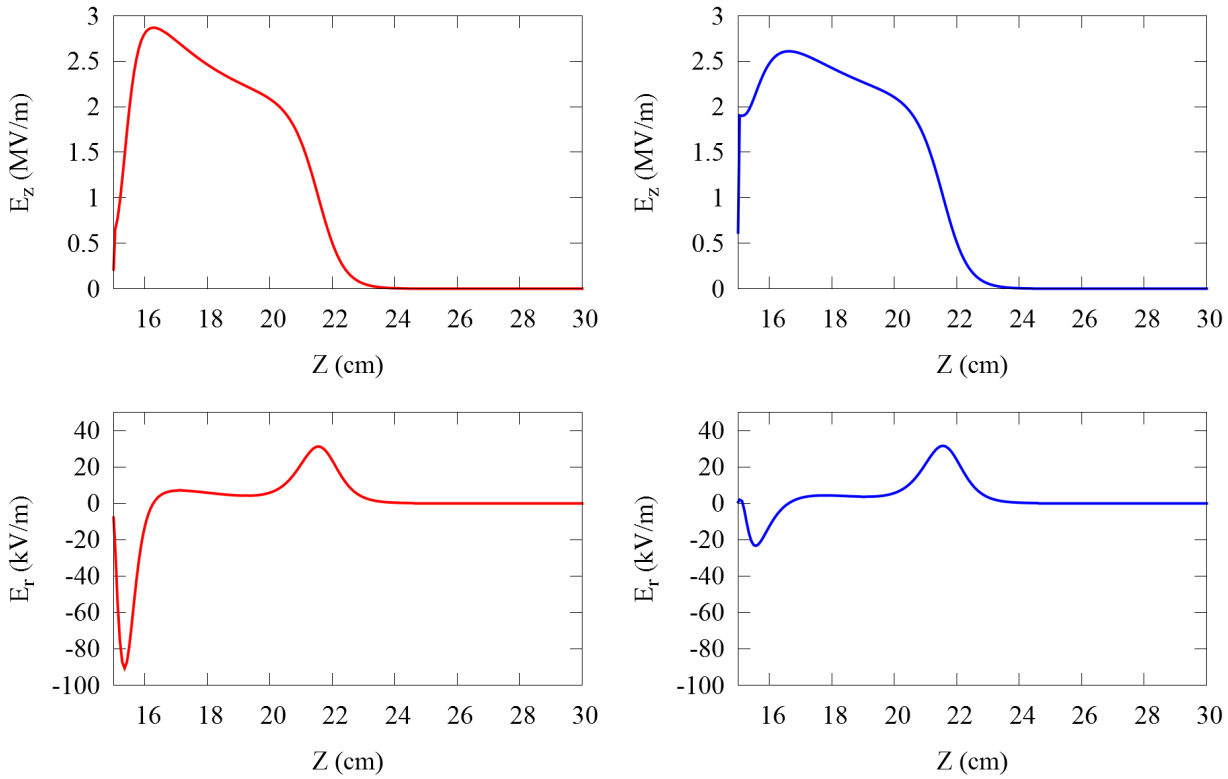

FIG. 13: The longitudinal electric field along the beam axis for A and B designs (top row, left and right respectively), and the radial electric field along a path 0.5 mm from and parallel to the beam axis (bottom row, left and right respectively).

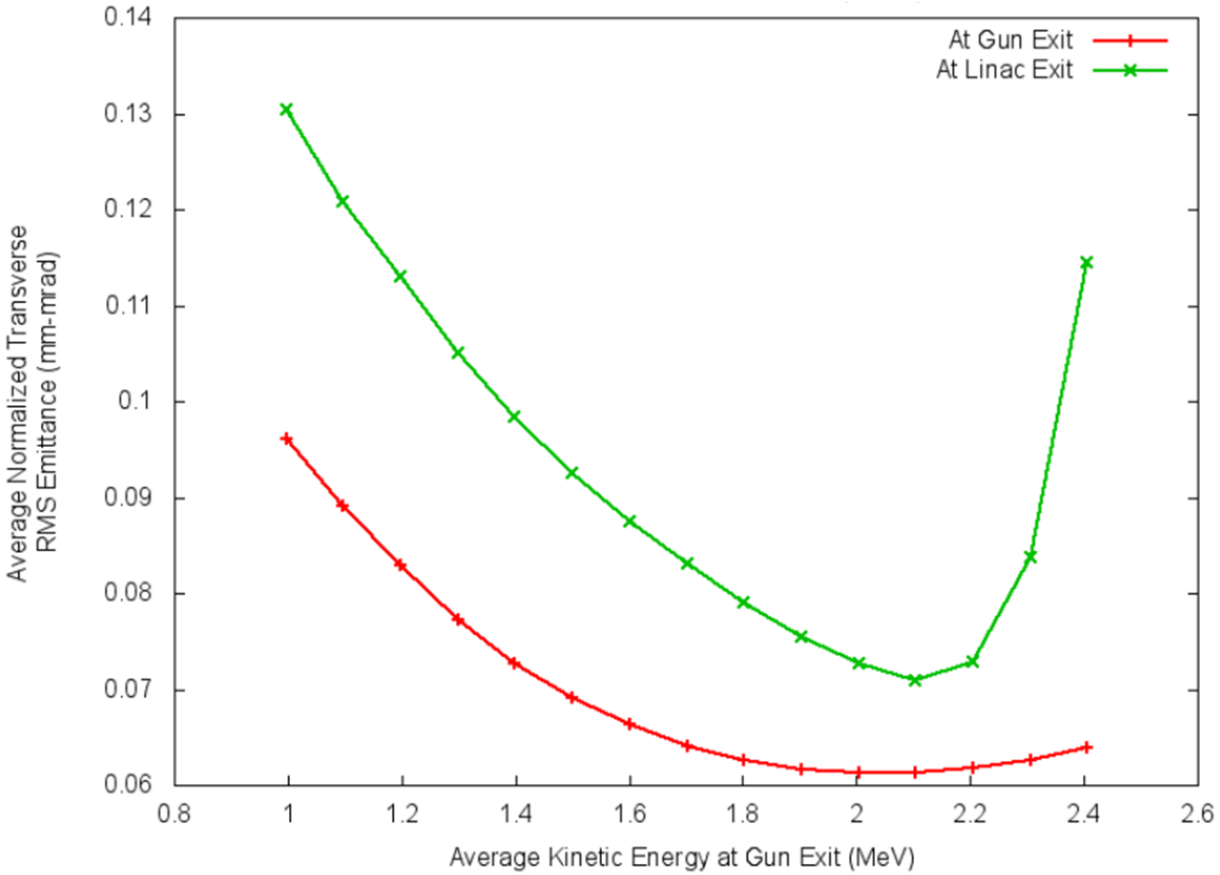

FIG. 14: The normalized average transverse *rms* emittance exiting both the gun and the linac as a function of the kinetic energy of the bunch exiting the gun.

space charge is negligible. There are two main reasons that such an approach is not feasible.

First, for any given gun geometry there is a point at which increasing the operating gradient is more detrimental than beneficial to the beam quality. Past this point, the strength of the focusing field is actually over-compensating for the effects of space charge on the bunch. This detrimental effect on the emittance due to over-compensating can be seen in Fig. 14, which demonstrates that the difference between the normalized transverse *rms* emittances of the bunch exiting the gun and the linac is also dependent upon the operating gradient of the gun. This effect arises from over-focusing the beam. Therefore, in general there exists an operating gradient for a given geometry which produces the smallest transverse emittance.

When computing the EM field for a simulation, several limitations that exist in real cavities can be ignored. However for real SRF cavities, there exists a difference between the highest peak surface field a cavity has ever attained and the highest peak surface field

most cavities can *reliably* obtain. In other words, no system design should require that the operating gradient of the cavities have peak electric and magnetic surface fields above certain values [59], leading to the second source of constraint.

What the value for each field is for "reliable" function is not a hard limit. Ten years ago, the rule of thumb was that operating gradients should be set such that the peak electric E_p and magnetic B_p surface fields were less than or equal to $30 - 35$ MeV/m and $60 - 70$ mT, respectively [60]. For more recent values of these parameters, the Jefferson Lab Continuous Electron Beam Accelerator Facility (CEBAF) 12 GeV Upgrade can be used as a guide. The operating gradient called for in the upgrade corresponds to the newly installed cavities running at an accelerating gradient of 19.2 MV/m, which in turn corresponds to $E_p \sim 41.7$ MV/m and $B_p \sim 71.8$ mT [30, 61]. Additionally, a large number of these new cavities are capable of operating up to at least $E_p \sim 58.6$ MV/m and $B_p \sim 101$ mT [30, 62].

A more direct comparison can be made to the peak surface fields expected at the operating gradient of the other SRF guns. The NPS gun has the operating gradient set such that E_p and B_p correspond to 51 MV/m and 78 mT, respectively. The WiFEL gun is set such that $E_p \sim 53$ MV/m, with B_p low enough to not be the limiting factor [63]. The BNL gun specifications call for E_p and B_p of 38 MV/m and 73 mT, respectively [64]. Consequently, the initial decision to limit the operating gradient of this gun such that $E_p \leq 40$ MV/m and $B_p \leq 80$ mT, is reasonable to the point of erring on the conservative side [26].

4.3 FIRST ITERATION

The initial version of the gun geometry was created by Rocio Olave and Karim Hernández-Chahín. In this work, CST MWS calculated the EM fields for a given geometry while *Astra* tracked a simulated bunch through those fields. The bunch consisted of 2000 particles with the properties given in Table 7. These values were influenced by a recent dissertation concerning the optimizing of RF guns, allowing for the choice of realistic parameters for a bunch produced by a cathode [26, 65]. The final iteration of this design is shown in Fig. 15, with the RF properties of the gun shown in Table 8 [66].

At this point, it became desirable to calculate the EM fields of the gun using Superfish instead of CST MWS. This change was motivated by the preference to more easily allow for the optimization of the gun geometry as a function of tracking results and the ability to know precisely the optimal gun geometry. As the desired EM field is unknown before starting, the beam properties of a bunch which has been tracked through the resulting fields is the only way to evaluate the "goodness" (or quality) of a given geometry. The process of exporting

TABLE 7: First bunch distribution off the cathode.

Parameter	Quantity	Units
Longitudinal distribution	Plateau	
Bunch length	24	ps
Rise time	6	ps
Radial distribution	Uniform	
rms bunch radius	0.5	mm
Initial transverse momentum	0	mrad
Bunch charge	10	pC
Initial kinetic energy	1	keV
p_z distribution	Isotropic	

TABLE 8: Cavity and RF properties of CST version of zeroth gun iteration.

Parameter	Quantity	Units
Frequency of accelerating mode	500	MHz
Cavity length	221.5	mm
Cavity radius	133.9	mm
Cavity gap	60	mm
Beamport aperture radius	10	mm
Peak electric surface field E_p^*	5.59	MV/m
Peak magnetic surface field B_p^*	10.4	mT
B_p^*/E_p^*	1.86	mT/(MV/m)
Geometrical factor, G	89.5	Ω
$(R/Q) \times G$	1.01×10^4	Ω^2
Energy content U^*	160	mJ

*At $E_{\text{acc}} = 1$ MV/m

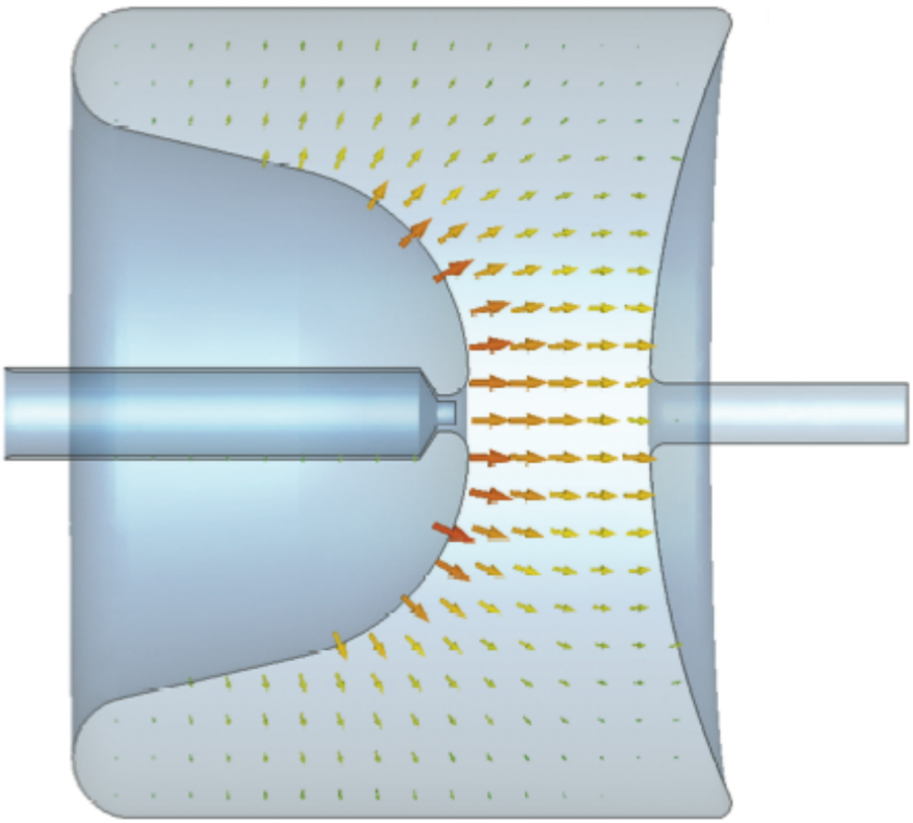

FIG. 15: Zeroth iteration of gun geometry with electric field.

the geometry of the gun from CST MWS is difficult. It became clear that obtaining a precise geometry was not as straightforward as desired.

To define the gun geometry in Superfish, the 2D Computer-Aided Design (CAD) file to describe the shape was exported from CST MWS [67]. The exported shape was then used to create a piecewise parametric function consisting of lines and circular arcs.

During the course of constructing this piecewise function, it was observed that there existed a discontinuity in the surface tangent of the geometry outside of the cathode holder. As the discontinuity was located in the area of highest electric surface field, an attempt was made to reduce the peak electric surface field there by adjusting the shape to better preserve the continuity of the surface tangent outside of the cathode holder. Small adjustments were made while preserving the general profile of the gun. The resulting adjusted profile is shown overlapping the piecewise function on the left of Fig. 16, with a zoomed view of the discontinuity shown on the right of the figure.

A comparison of the EM fields in the two cases is shown in Fig. 17, with both the longitudinal field on-axis and the radial field 0.5 mm away from and parallel to the beam axis plotted as a function of z. For both plots, a close-up view is on the right to emphasize the differences in resulting fields from the different goemetries. Table 9 contains the cavity and RF properties of the adjusted profile. The parameters of the bunch exiting the gun, after being tracked by *Astra*, are shown in Table 10. While the normalized transverse *rms* emittance is larger than desired by 20%, these results are encouraging in their support of the feasibility of the initial target specifications.

4.4 GEOMETRY PARAMETERIZATION

During the course of the design further gun optimization was necessary to obtain the desired electron beam at the IP. To spport the optimization it was necessary to create a set of parameters to fully define the parametric piecewise function that describes the gun shape, assuming the overall gun shape is retained, i.e. the reentrant cathode entrance, nosecone, fin, and reentrant exit face. These components are labeled on an outline of the gun in Fig. 18. In order to minimize the number of parameters in the design, constraints were set and a few assumptions were made.

Two of the constraints have already been mentioned, in context with adjusting the zeroth iteration of the gun design exported from CST MWS: the gun shape will be continuous and, except for the cathode holder, that the surface tangent will also be continuous. One additional constraint is that the radius of the gun is adjusted so that the fundamental

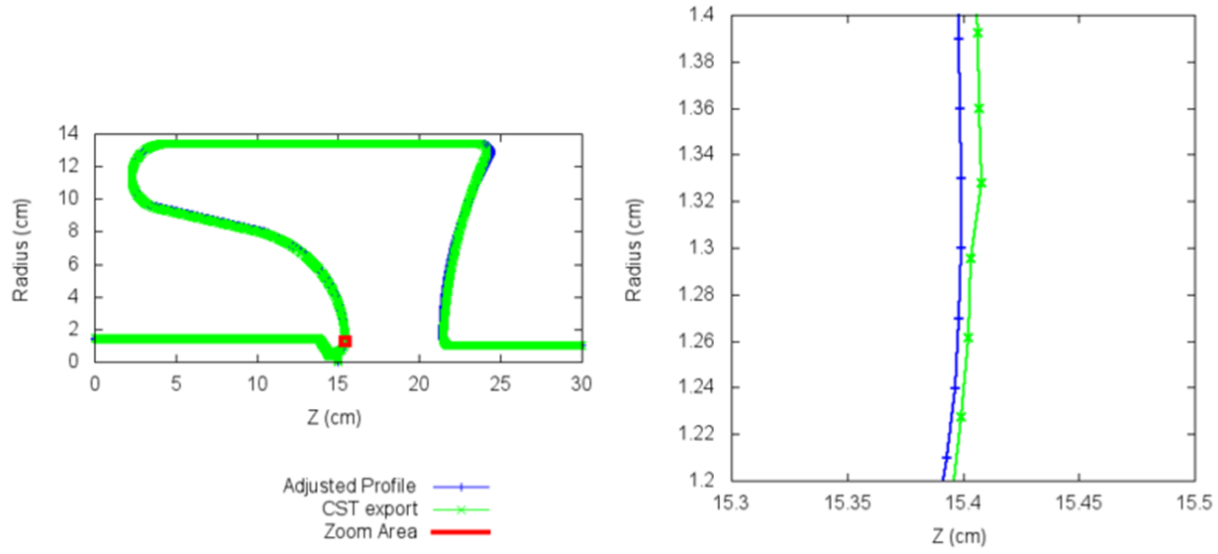

FIG. 16: Comparison of CST export and adjusted geometry, with zoom area to the right.

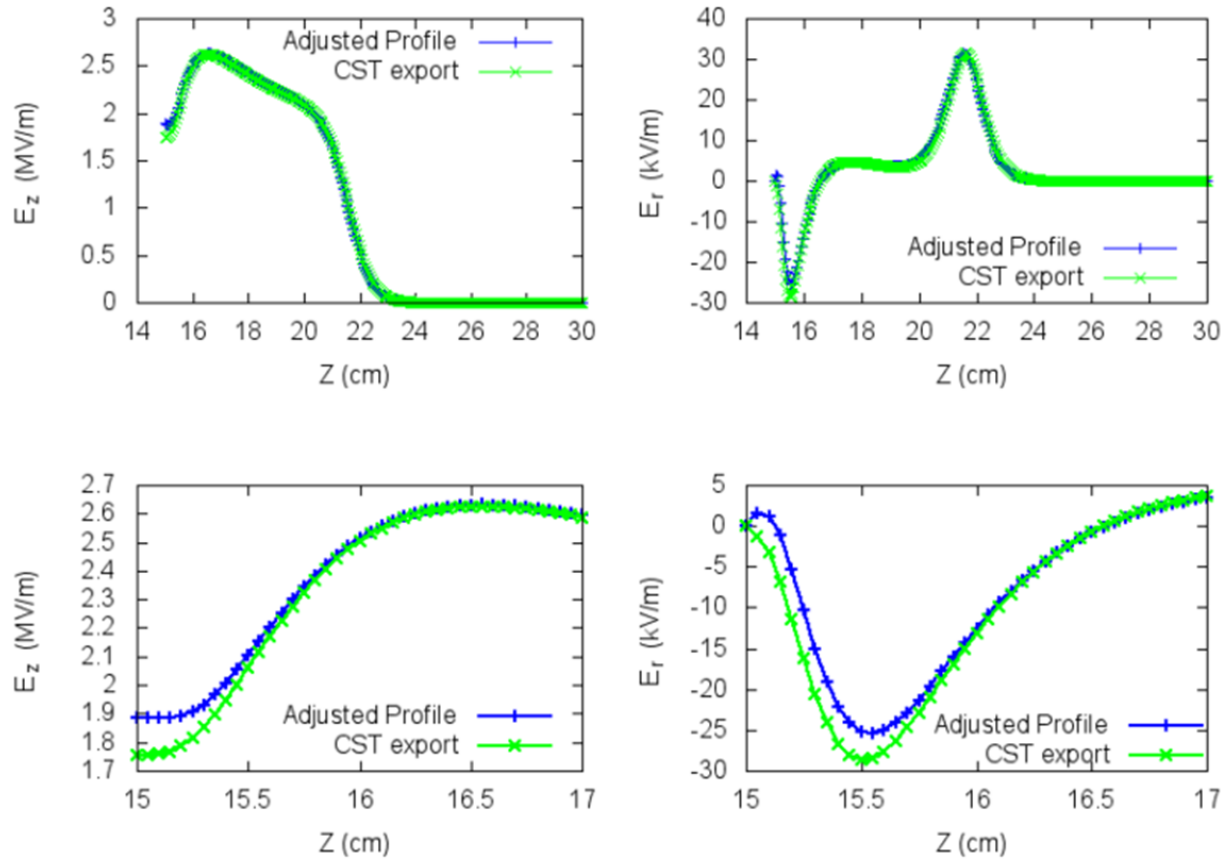

FIG. 17: Comparison of longitudinal field on-axis and radial field 0.5 mm away from and parallel to the beam axis for CST export and adjusted geometry, with zoom areas to the right.

TABLE 9: Cavity and RF properties of adjusted gun profile (first gun iteration).

Parameter	Quantity	Units
Frequency of accelerating mode	498.4	MHz
Cavity length	221.5	mm
Cavity radius	133.9	mm
Cavity gap	69	mm
Beamport aperture radius	10	mm
Peak electric surface field E_p^*	3.68	MV/m
Peak magnetic surface field B_p^*	6.67	mT
B_p^*/E_p^*	1.81	mT/(MV/m)
Geometrical factor, G	84.5	Ω
$(R/Q) \times G$	1.3×10^4	Ω^2
Energy content U^*	45	mJ

*At $E_{\mathrm{acc}} = 1$ MV/m

TABLE 10: *Astra* tracking results of first design iteration at gun exit.

Parameter	Quantity	Units
kinetic energy	1.55	MeV
rms energy spread	0.53	keV
$\sigma_{x,y}$	0.48	mm
$\epsilon^N_{(x,y),\mathrm{rms}}$	0.12	mm-mrad
σ_z	2.1	mm

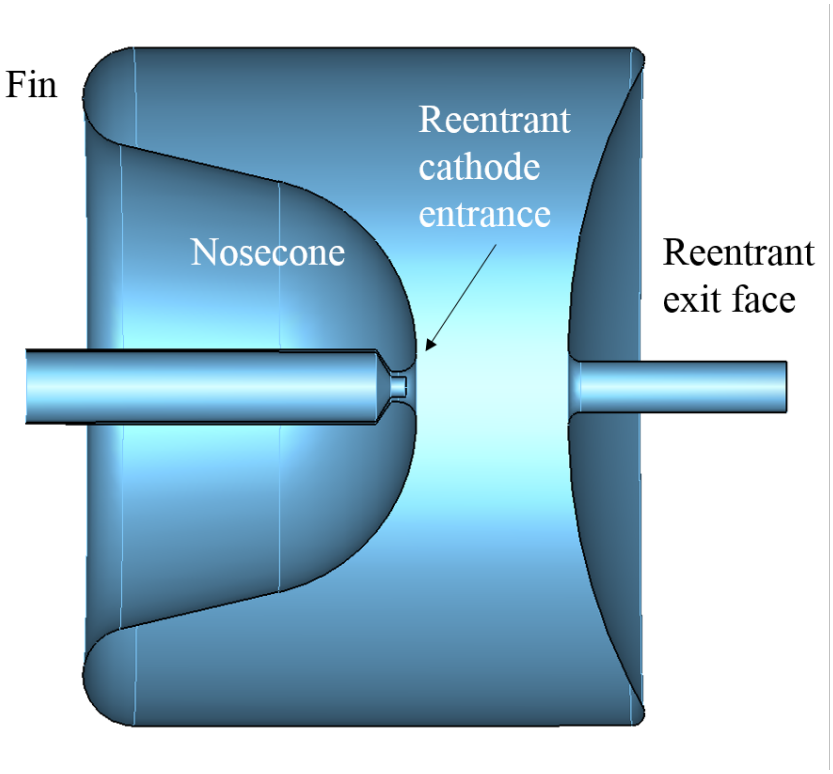

FIG. 18: Basic gun geometry with labels of the components.

frequency is 500 MHz. The two assumptions made are that the new gun shape is similar to its original and that there is an identical radius for the two smaller spherical blends on the exit face, one between the exit face and the cylinder shell (which is a distance of the gun radius away from and parallel to the beam axis) and the other between the exit face and the beam pipe.

With these constraints and assumptions, twelve parameters can be defined which can be used to fully dictate the entire geometry. Table 11 shows the list of these twelve parameters, including the symbol which is keyed to Fig. 19, a short description, and the value of each in the first iteration of the geometry. For an example showing how changing the value of one parameter can alter the design, observe Fig. 12. Here the shape on the left has $y_E = 7$ mm, while the shape on the right has $y_E = 14$ mm, with all other parameter values being held constant, except for the radius which is altered so that the frequency of each geometry is 500 MHz.

4.4.1 SWITCHING TO IMPACT-T

TABLE 11: List of geometry parameters with descriptions and values for the first iteration of the gun geometry.

Parameter	Description	Value	Units
R_{cav}	Radius of gun	133.94	mm
R_{cathode}	Radius of cathode holder tip	4.	mm
R_{pipe}	Radius of exiting beam pipe	10.	mm
R_{entrance}	Radius of entrance in nosecone	6.	mm
x_E	Distance of cathode recession	4.	mm
y_E	y-position of location on nosecone with vertical surface tangent	13.	mm
α	Angle of nosecone	13	°
l_{fin}	Horizontal distance between fin tip and cathode tip	127.95	mm
h_{fin}	Maximum width of fin	52.734	mm
l_{gap}	Horizontal distance between x_E and x-position of y_{E2}	60.	mm
l_{rec}	Horizontal distance between two locations on exit face with vertical surface tangent	30.	mm
y_{E2}	y-position of location nearest beam pipe with vertical surface tangent	15.	mm

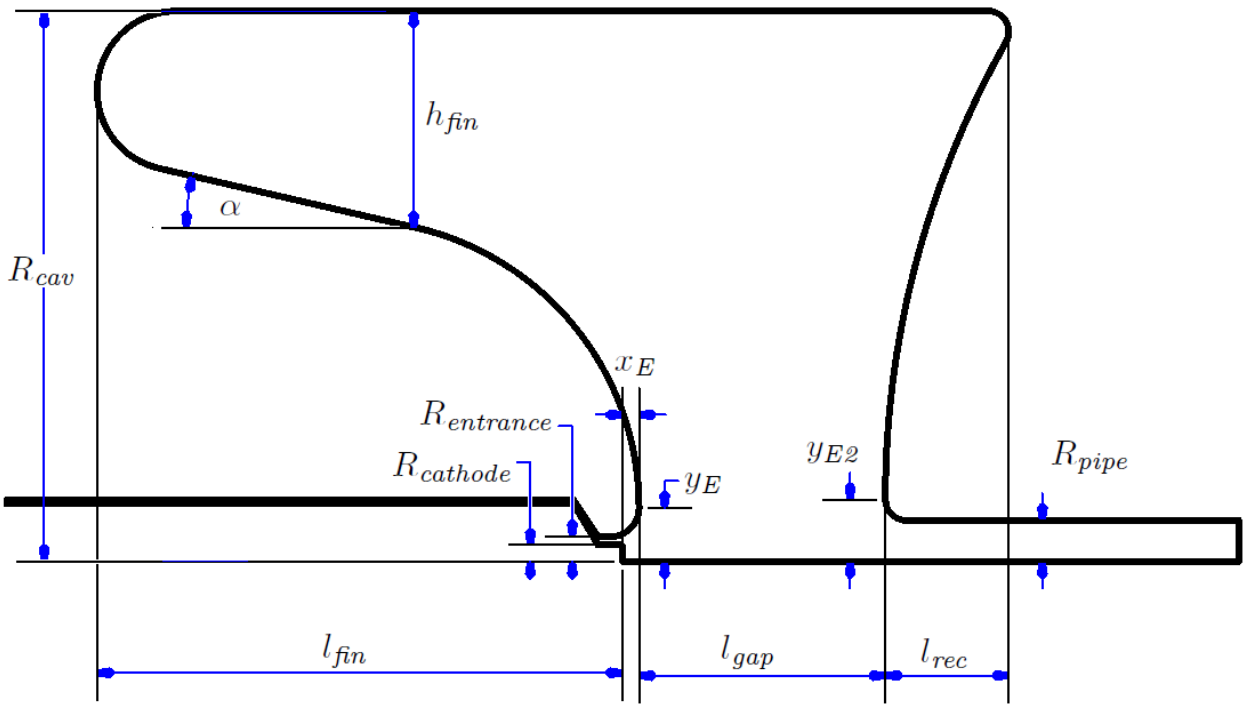

FIG. 19: Diagram of gun geometry with parameters.

Prior to the second iteration design for the gun, particle tracking for the accelerating section was performed with *Astra*. During the second iteration and subsequently, it was advantageous to perform the tracking using IMPACT-T. A shorter run time results using IMPACT-T to track 100,000 macroparticles as compared to *Astra* tracking 2,000. In addition, this switch was prompted by concerns over the accuracy of *Astra*'s space charge calculations.

The *Astra* tracking results converge for 2,000 macroparticles at a given set of input variables for space charge calculation (relating to the grid applied over the bunch to make the calculations). However, this convergence only holds for a specific distribution out of the cathode. When the distribution of the bunch out of the cathode changes, the correct input settings for space charge calculation change as well, which is articulated in the documentation for ASTRA [37]. While a user may be willing to spend the time correcting the input settings for every new cathode distribution, it is far easier and quicker to use a code more insensitive to initial distributions, such as IMPACT-T. While the correct settings must still be found in a similar manner, these settings remain constant when the initial distribution is altered.

Even putting aside the necessity of adjusting the input variables for the space charge calculation with every new bunch distribution off the cathode, there is a more fundamental potential flaw. It has been suggested that accurate space charge calculations must take place at a *time* step, rather than a position step. Furthermore, this is most likely to make a difference in regions where the bunch is not yet relativistic [42].

There does not yet exist complete benchmarking of space charge calculation in tracking codes with regards to experimental results [68–71]. Given that the driving force of the gun design has been the resulting transverse emittance, which is greatly affected by space charge, it is reasonable to make a strong effort to use the most accurate space charge model available. Due to quicker processing time, space charge calculation at constant times, and no need to change space charge calculation settings when altering the initial bunch distribution from the cathode, IMPACT-T is the appropriate choice to produce accurate simulation results.

4.5 SECOND ITERATION

At the exit of the first iteration linac, the *rms* energy spread was over four times the desired value. The full consequences of this result are expanded upon later in this dissertation. The energy spread was limited by a long bunch length and reducing the bunch length should produce the appropriate energy spread at the linac exit. To determine the appropriate bunch

TABLE 12: Second iteration bunch distribution off the cathode.

Parameter	Quantity	Units
Longitudinal distribution	Plateau	
Bunch length	1.5	ps
Rise time	0.375	ps
Radial distribution	Uniform	
rms bunch radius	1	mm
Initial transverse momentum	0	mrad
Bunch charge	10	pC
Initial kinetic energy	1	keV
p_z distribution	Isotropic	

length, simulations were run with successively smaller bunch durations off the cathode passing through the first gun geometry, until the bunch exiting the linac met the desired energy spread value. The bunch length found was 1.5 ps, which is 6.25% of the originial bunch length. The *rms* spot size off the cathode was doubled to mitigate the increased effect of space charge due to a significantly reduced initial bunch length. All properties of the new bunch distribution are shown in Table 12. As this changes the charge distribution within the bunch and consequently the defocusing effect of the space charge forces which needs to be compensated, the first design iteration no longer produces the best beam.

Given the drastic computing power and time that would be necessary to run an optimization varying large numbers of parameters, it was decided to focus on a few key parameters to improve the beam properties. To improve beam properties, a parameter scan was run for two specific parameters: x_E and y_E. This scan consists of incrementing the specific parameter and holding the other ten independent parameters constant at the values shown in Table 11, while adjusting the gun outer radius to achieve the proper frequency. These two parameters were chosen as their position influences the radial focusing field in the gun makes it likely that altering one or both of them would lead to the best resulting beam.

Given the emphasis in the preceding portion of this chapter, one may think that the approach would be to choose the shape that produces the beam with the smallest emittance out of the gun. But, as has already been shown, the smallest emittance out of the gun does not necessarily correspond to the smallest emittance out of the linac. Additionally, given the small spot size desired at the IP, if the spot size coming out of the linac is too large, focusing the beam becomes a non-trivial problem that is best avoided. Therefore, the design

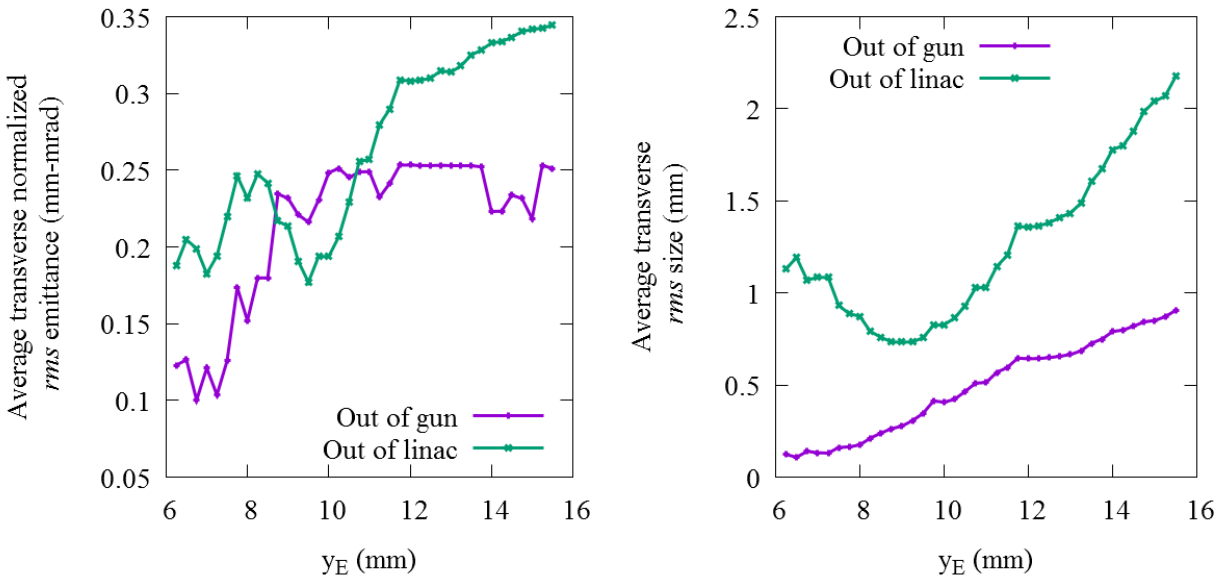

FIG. 20: Plots of the average transverse normalized *rms* emittance (left) and size (right), out of both gun and linac, given as a function of y_E, the geometry parameter being varied.

was altered so that the transverse emittance and the *rms* spot size were minimized for the bunch exiting the linac.

In each simulation run, it is set such that E_p and B_p are both less than or equal to 40 MV/m and 80 mT, respectively. The amplitude of the spoke cavities that make up the linac are adjusted in each case so that the beam energy after passing through the gun and four spoke cavities is always 25 MeV. Selected results of the scans are shown in Fig. 20. The plots contained within this figure show the values of the transverse rms normalized emittances and sizes both out of the gun and out of the linac as a function of the value of the parameter being varied.

The option that best fulfilled the desires of both a small emittance and size simultaneously is $x_E = 4.$ mm and $y_E = 9.5$ mm, with a radius (R_{cav}) of 134 mm. All other parameter values are equal to those shown in Table 11. Notably, x_E did not change, as varying this parameter had no significant effect on the results. Fig. 21 shows both a side-by-side and overlapping comparisons of the first and second iteration gun geometries, while Table 13 gives the RF properties of the second iteration gun. Fig. 22 compares the longitudinal electric field on axis and the radial electric field parallel to and 0.5 mm away from the axis for both guns. To demonstrate the benefit of this geometry alteration, Table 14 compares the bunch produced

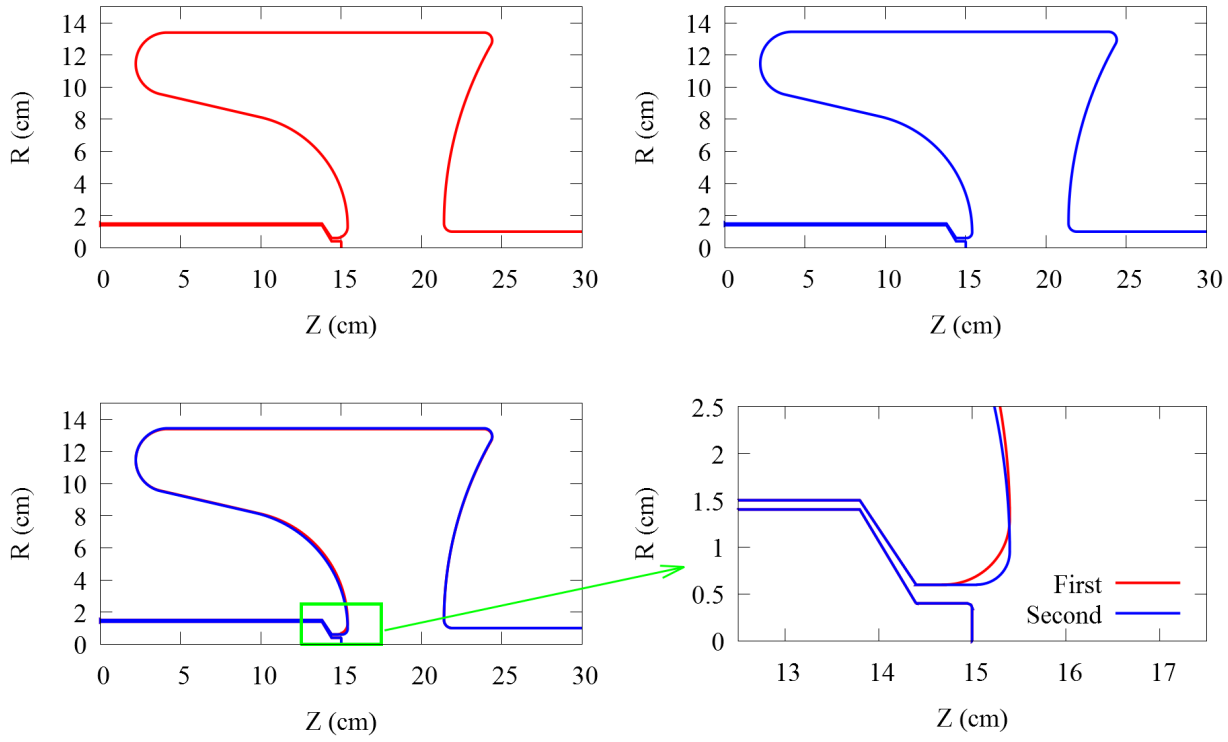

FIG. 21: Side-by-side and overlapping comparisons of the first and second gun geometry iterations, with a zoom view of the main difference.

out of the linac when started with the first and second iteration guns. The transverse phase space and the beam spot exiting the second iteration gun are shown in Fig. 23.

4.6 FINAL DESIGN

At this point, the only significant difference between the final results for the second iteration and the original target goals is the transverse emittance, making it the parameter most in need of improvement. Consequently, the bunch length off the cathode was increased until the bunch length exiting the linac was such that more than 80% of the bunch was contained within 3 psec. The reasoning for this adjustment was that with a bunch sufficiently short, chirping the final two cavities could decrease the energy spread if necessary. This approach led to a new bunch off the cathode that is 3 times the length of the bunch in the second iteration, with the details of the new bunch shown in Table 15.

Going back to the fact that different bunch distributions produce different space charge fields, thus requiring different radial electric fields to be optimally compensated, the geometry

TABLE 13: Cavity and RF properties of second gun design iteration.

Parameter	Quantity	Units
Frequency of accelerating mode	500	MHz
Cavity length	221.5	mm
Cavity radius	134	mm
Cavity gap	69	mm
Beamport aperture radius	10	mm
Peak electric surface field E_p^*	3.89	MV/m
Peak magnetic surface field B_p^*	6.53	mT
B_p^*/E_p^*	1.68	mT/(MV/m)
Geometrical factor, G	84.4	Ω
$(R/Q) \times G$	1.33×10^4	Ω^2
Energy content U^*	44	mJ

*At $E_{\text{acc}} = 1$ MV/m

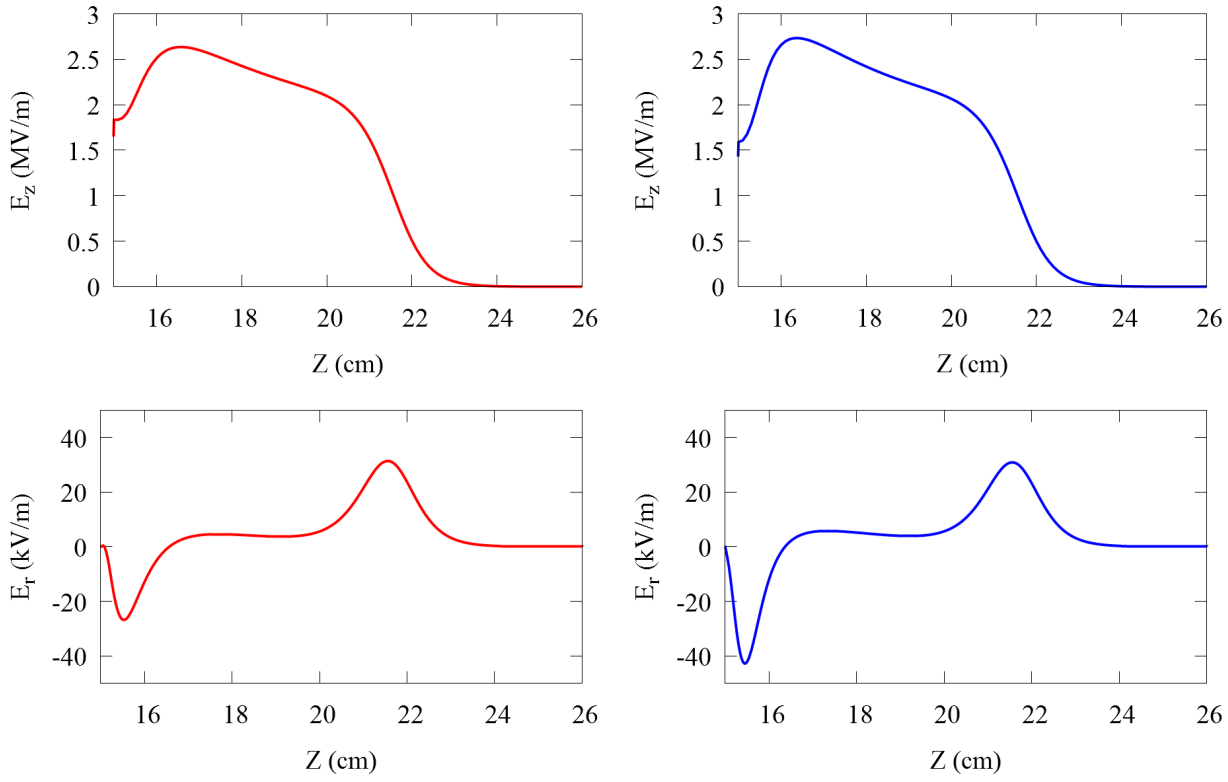

FIG. 22: Comparison of longitudinal field on-axis (top row) and radial field 0.5 mm away from and parallel to the beam axis (bottom row) for the first (left column) and second (right column) geometry iterations.

TABLE 14: Comparison of beam properties from results of tracking second iteration bunch distribution through both first and second gun iterations at the exit of the gun (top) and linac (bottom).

Parameter	First	Second	Units
kinetic energy	1.6	1.5	MeV
rms energy spread	3.5	4.4	keV
$\sigma_{x,y}$	0.67	0.35	mm
$\epsilon^N_{(x,y),\mathrm{rms}}$	0.25	0.22	mm-mrad
σ_z	0.27	0.28	mm
kinetic energy	25.	25.	MeV
rms energy spread	6	9	keV
σ_x	1.4	0.75	mm
σ_y	1.4	0.76	mm
$\epsilon^N_{x,\mathrm{rms}}$	0.32	0.18	mm-mrad
$\epsilon^N_{y,\mathrm{rms}}$	0.31	0.17	mm-mrad
σ_z	0.30	0.35	mm

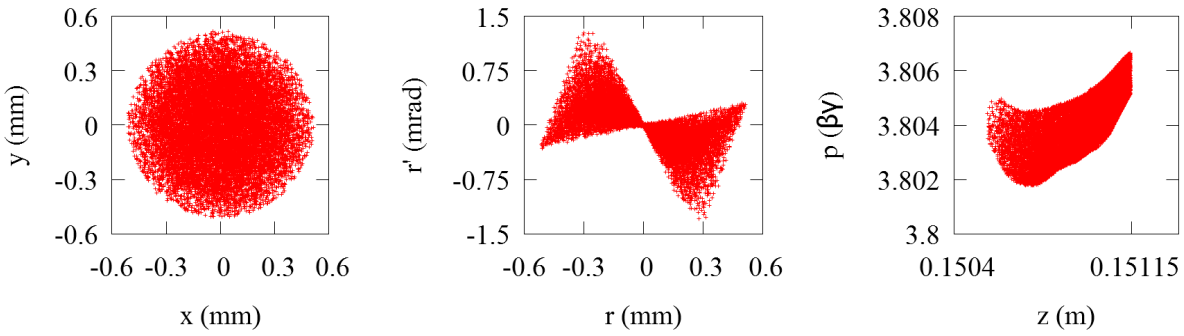

FIG. 23: Beam spot (left), transverse phase space (center), and longitudinal phase space (left) of bunch exiting gun in the second iteration.

TABLE 15: Final iteration bunch distribution off the cathode.

Parameter	Quantity	Units
Longitudinal distribution	Plateau	
Bunch length	4.5	ps
Rise time	1.125	ps
Radial distribution	Uniform	
rms bunch radius	1	mm
Initial transverse momentum	0	mrad
Bunch charge	10	pC
Initial kinetic energy	1	keV
p_z distribution	Isotropic	

of the gun was varied slightly to provide the best possible bunch exiting the linac, primarily by minimizing the transverse normalized *rms* emittance. A comparison of the two geometries is shown in Fig. 24, with the physical and RF properties of the new design shown in Table 16. The gun is operated at the gradient which corresponds to $B_p < 80$ mT and $E_p \sim 40$ MV/m. A comparison of selected portions of the EM fields is shown in Fig. 25.

The IMPACT-T tracking results at the exit of the gun are shown in Table 17, with the transverse phase space and beam spot at the gun exit shown in Fig. 26. Except for the energy, all other properties of the bunch exiting the final gun iteration are smaller than those of the second iteration. This includes both the *rms* energy spread and the *rms* bunch length. This result may seem counterintuitive, as the bunch off the cathode is three times longer in the final version than the second. The second version bunch is so short as to increase the contribution of the longitudinal space charge to the longitudinal distribution of the beam.

4.6.1 DRIVE LASER

In order to produce a 4.5 psec flat-top bunch off the cathode, there exist multiple options. One fully realized option is in use in the LCLS injector [72]. This drive laser was manufactured by *Thales Laser* and is a frequency tripled, chirped-pulse amplification system based on a Ti:sapphire laser [72, 73]. The specifications called for by the LCLS commissioning require a FWHM pulse duration of 6 ps with a repetition rate of up to 120 Hz. In addition, the laser has an adjustable pulse duration between 3 and 20 ps [72]. While the pulse duration is in the correct regime this project requires, the repetition rate is less than required by nearly

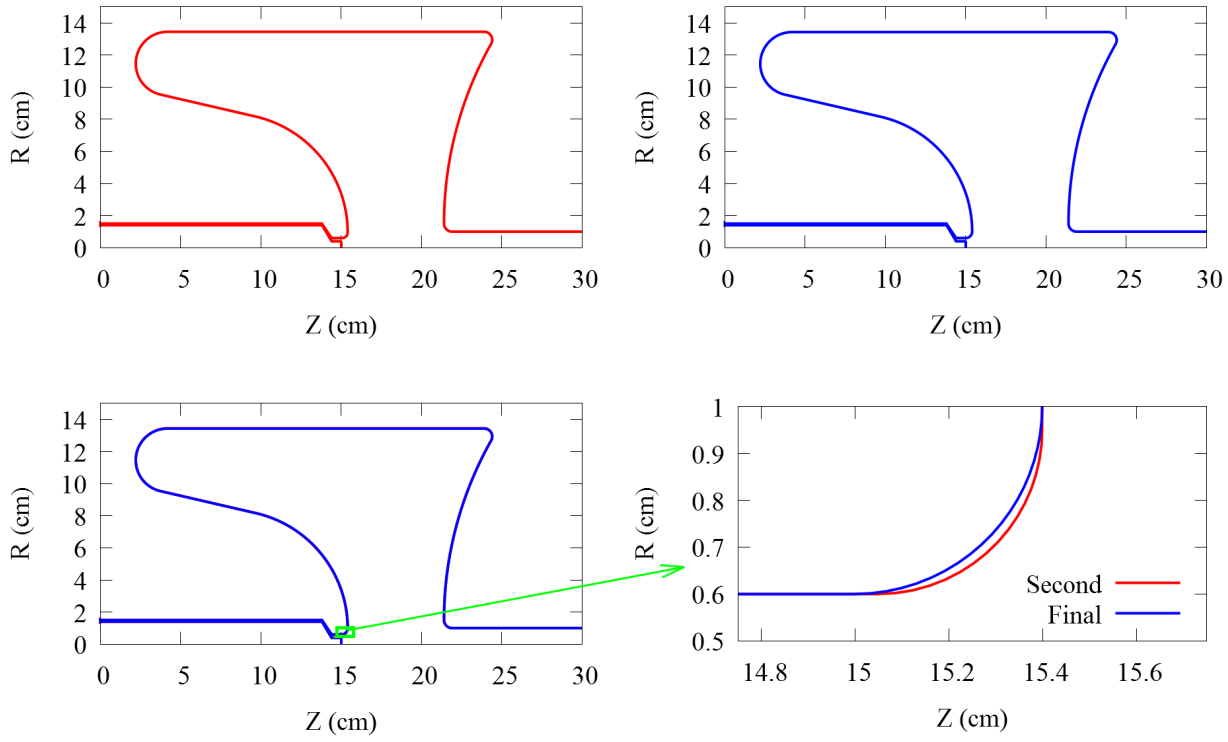

FIG. 24: Side-by-side and overlapping comparisons of the second and final gun geometry iterations, with a zoom view of the main difference.

TABLE 16: Cavity and RF properties of final gun design iteration. Set to operate at $E_{\text{acc}} = 10.3$ MV/m.

Parameter	Quantity	Units
Frequency of accelerating mode	500	MHz
Cavity length	221.5	mm
Cavity radius	134	mm
Cavity gap	69	mm
Beamport aperture radius	10	mm
Peak electric surface field E_p^*	3.86	MV/m
Peak magnetic surface field B_p^*	6.55	mT
B_p^*/E_p^*	1.70	mT/(MV/m)
Geometrical factor, G	83.7	Ω
$(R/Q) \times G$	1.31×10^4	Ω^2
Energy content U^*	44	mJ

*At $E_{\text{acc}} = 1$ MV/m

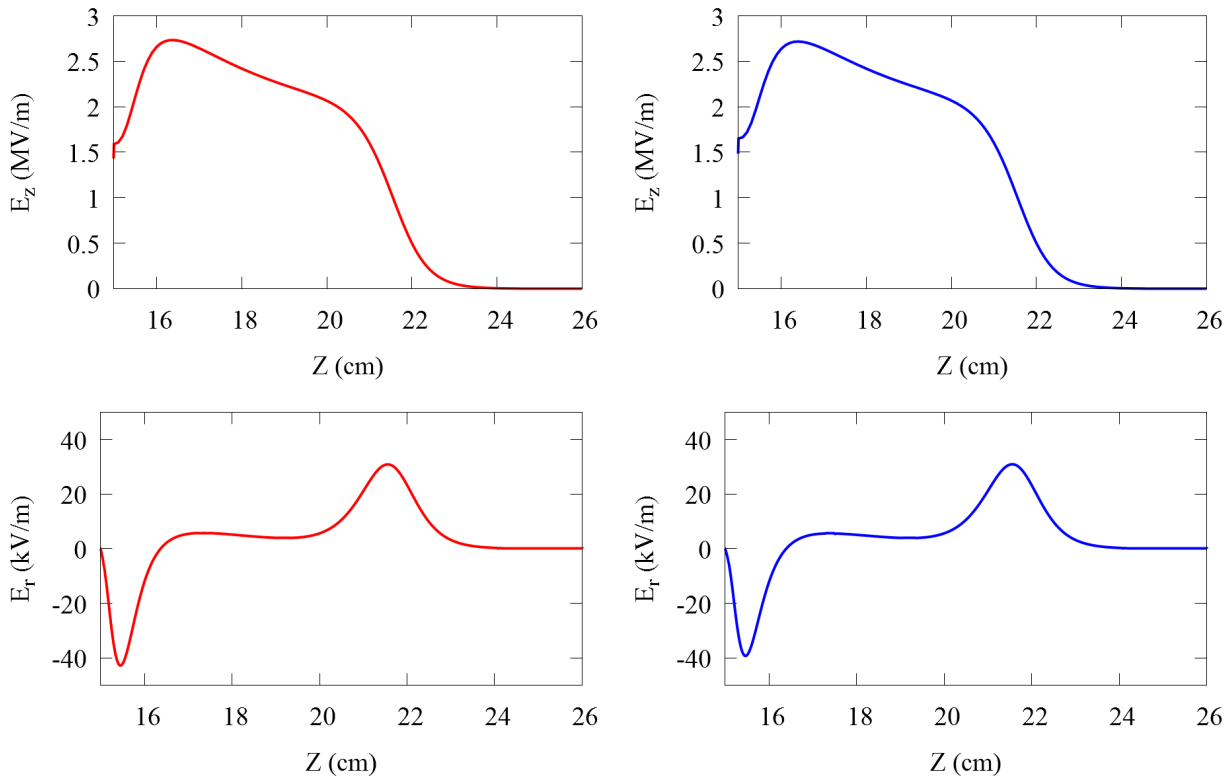

FIG. 25: Comparison of longitudinal field on-axis (top row) and radial field 0.5 mm away from and parallel to the beam axis (bottom row) for the second (left column) and final (right column) geometry iterations.

TABLE 17: IMPACT-T tracking results of final design iteration at gun exit.

Parameter	Quantity	Units
kinetic energy	1.51	MeV
rms energy spread	0.68	keV
$\sigma_{x,y}$	0.29	mm
$\epsilon^{N}_{(x,y),\mathrm{rms}}$	0.20	mm-mrad
σ_z	0.18	mm

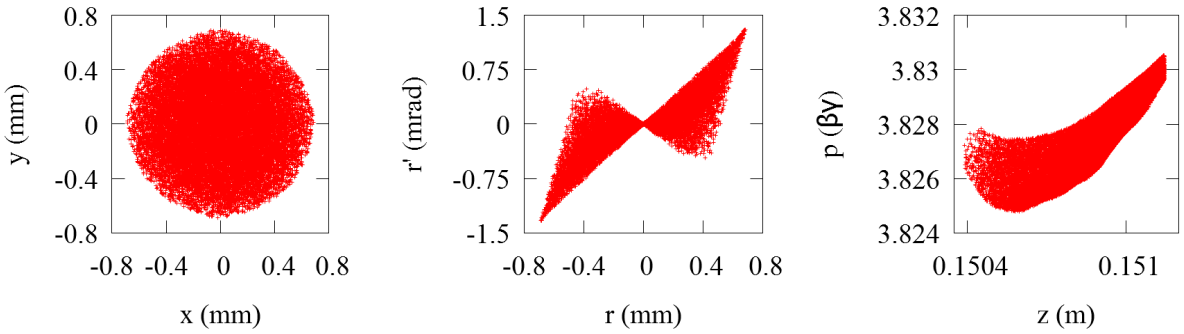

FIG. 26: Beam spot (left), transverse phase space (center), and longitudinal phase space (left) of bunch exiting gun in final iteration.

two orders of magnitude.

Another scheme for producing a flat-top bunch off the cathode involves the use of long-period fiber gratings (LPGs). Using this approach, it has been demonstrated experimentally that Gaussian-like optical pulses can be transformed into flat-top pulses. In the proof of concept experiment which confirmed this approach, 600 fs and 1.8 ps Gaussian-like pulses were transformed into 1 and 3.2 ps flat-top pulses, respectively. The same LPG was used for both transformations, demonstrating the adaptibility of such a device [74]. It remains to demonstrate this technology at high average power.

4.7 EMITTANCE DECREASE

It has been noted before that the transverse normalized *rms* emittance of the bunch out of the gun is not necessarily the same out of the linac. In the first iteration of the gun design, there was an increase in emittance after the bunch exited the gun because it was not yet at a sufficient energy to make space charge negligible. In the second and final iterations, however, the emittance actually decreases between the gun and linac exits. The final iteration has a greater decrease in emittance and will be examined here to explain the behavior.

This decrease in emittance is counter-intuitive to our understanding of emittance behavior. Liouville's theorem states that normalized emittance is invariant under conservative and linear forces and acceleration. However, this applies to the normalized emittance of the entire beam, not the *rms* normalized emittance that is being quoted.

The transverse normalized *rms* emittances and *rms* spot sizes of the bunch as it passes through the linac are shown in Fig. 27. Both horizontal and vertical emittances decrease through the linac, though the rate of decrease changes with the longitudinal position and

which transverse component is being considered. The transverse *rms* sizes of the beam grow rapidly immediately after the bunch exits the gun, but the size increase is limited within the linac.

Using IMPACT-T, it is possible to see the evolution of the bunch after the gun as the beam drifts downstream, without passing through the linac. The transverse normalized *rms* emittance and the spot size of this drifting bunch are shown as a function of longitudinal position in Fig. 28. While the spot size increases as the bunch drifts downstream, the emittance decreases to a minimum at approximately $z = 0.7$ m, before increasing. The transverse phase spaces of the bunch are shown in Fig. 29 at a number of locations after the gun exit, up to and including the minimum at $z = 0.7$ m.

One further aspect of interest is that for the drifting bunch, $\epsilon^N_{\mathrm{rms},r} = 0.12$ mm-mrad at the minimum of $z = 0.7$ m, but at the exit of the linac $\epsilon^N_{\mathrm{rms},x} = 0.10$ mm-mrad and $\epsilon^N_{\mathrm{rms},y} = 0.13$ mm-mrad. So even the average of the two transverse emittances is less than what can be attained if the bunch just drifts after the gun. If the bunch charge of the beam exiting the gun is artificially decreased, the distance to the emittance minimum increases and the emittance minimum decreases. This can be considered analogous to increasing the beam energy without the additional phase space manipulations of passing the beam through the "quadrupole-like" spoke cavities, which is discussed in the next chapter.

Increasing the energy of the beam does not mean it is impossible for an emittance minimum to occur within the linac; it depends on the bunch exiting the gun. One example of an emittance minimum occuring within the linac is shown in Fig. 30. The figure shows the transverse normalized *rms* emittances of the final cathode bunch tracked through the second version of the accelerating section. While the emittances decrease, after the minumum both increase. At this minimum, $\epsilon^N_{\mathrm{rms},x} = 0.095$ mm-mrad and $\epsilon^N_{\mathrm{rms},y} = 0.11$ mm-mrad, both of which are smaller values, respectively, than those of the bunch exiting the final linac. With the increase after the minimum, the bunch exits with $\epsilon^N_{\mathrm{rms},x} = 0.13$ mm-mrad and $\epsilon^N_{\mathrm{rms},y} = 0.13$ mm-mrad, so this is not the best possible system for this initial bunch. Consequently, there is some limit on the rate of emittance decrease for the bunch exiting the gun. If the emittance decreases too rapidly, a minimum occurs within the linac, which leads to the beam quality suffering.

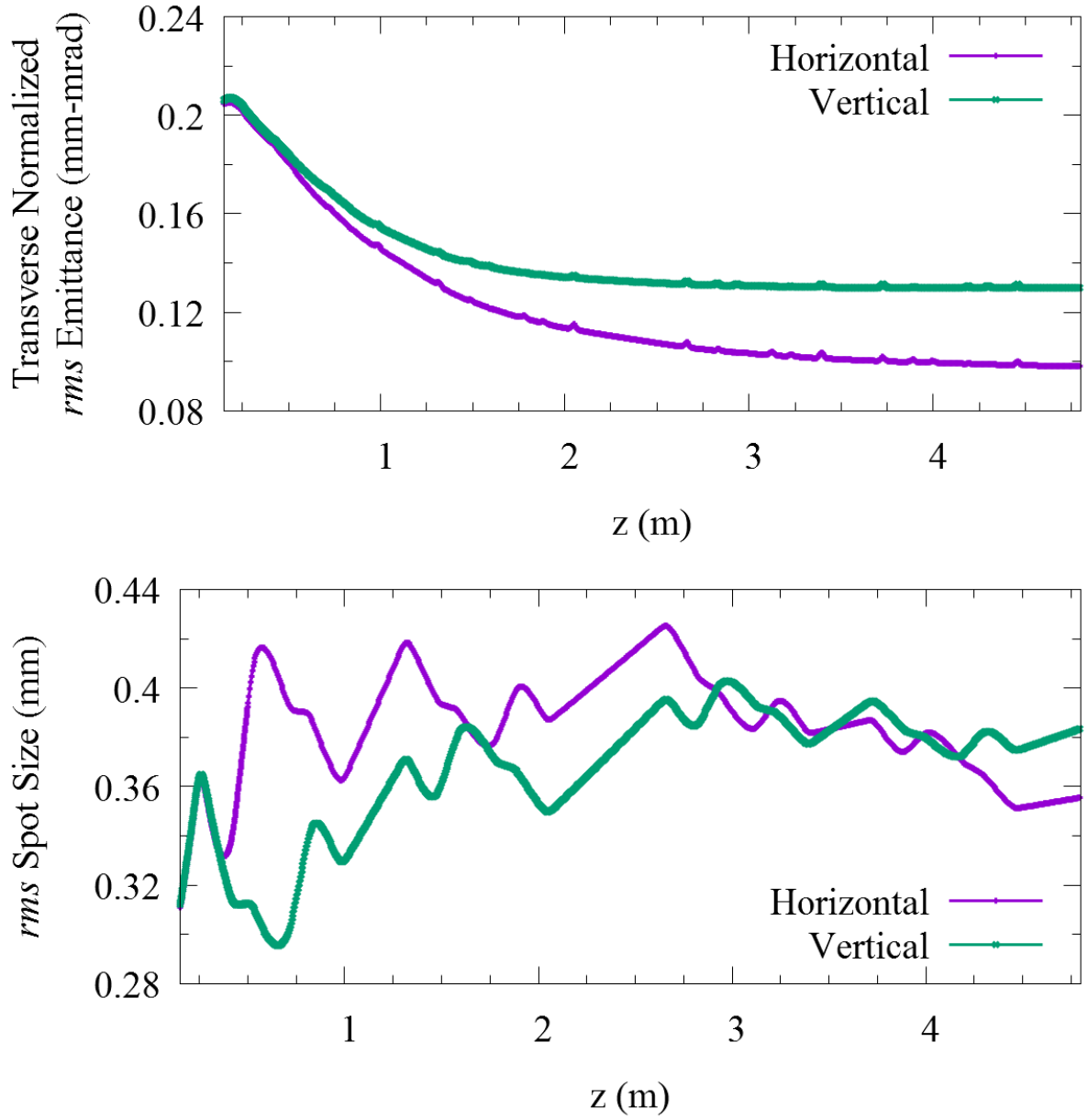

FIG. 27: Transverse normalized *rms* emittances (top) and spot sizes (bottom) of bunch passing through the linac in the final configuration.

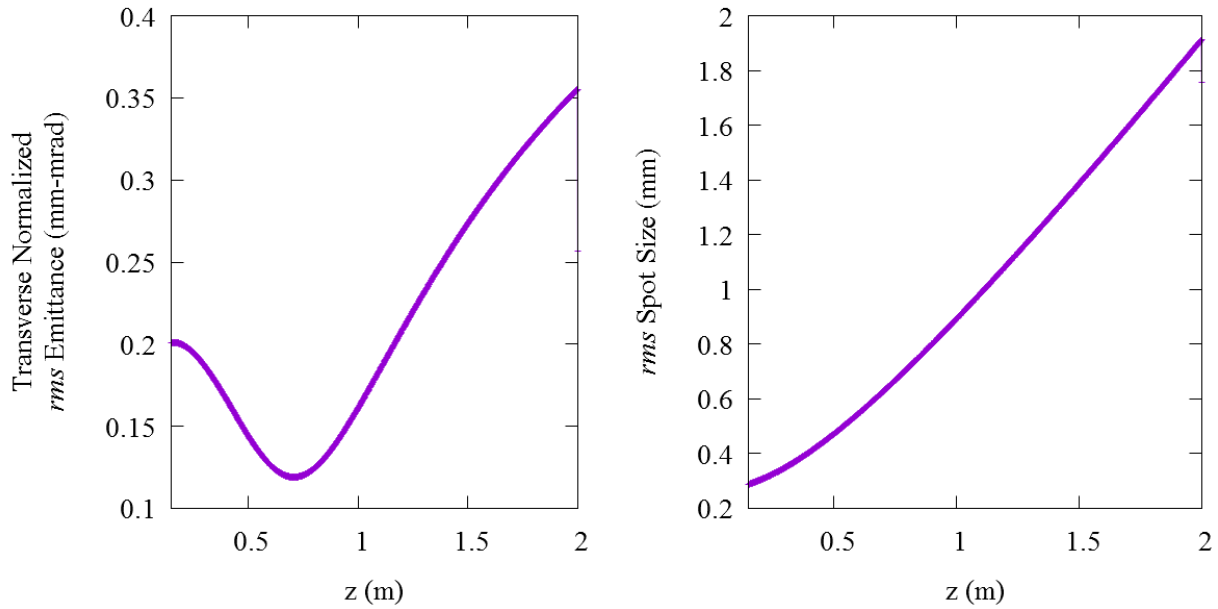

FIG. 28: Transverse normalized *rms* radial emittance (left) and transverse spot size (right) of final bunch drifting after final gun exit as a function of longitudinal position.

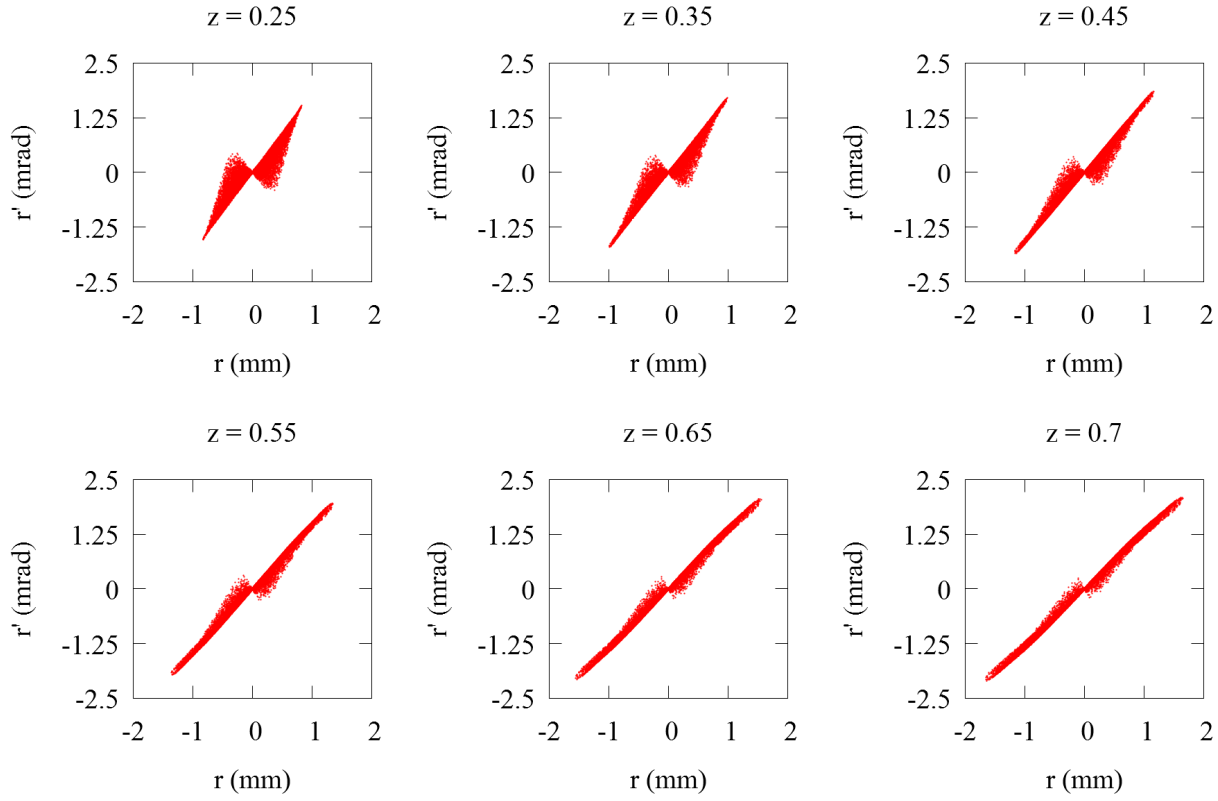

FIG. 29: Transverse phase spaces of the final bunch exiting the final gun as it drifts downstream.

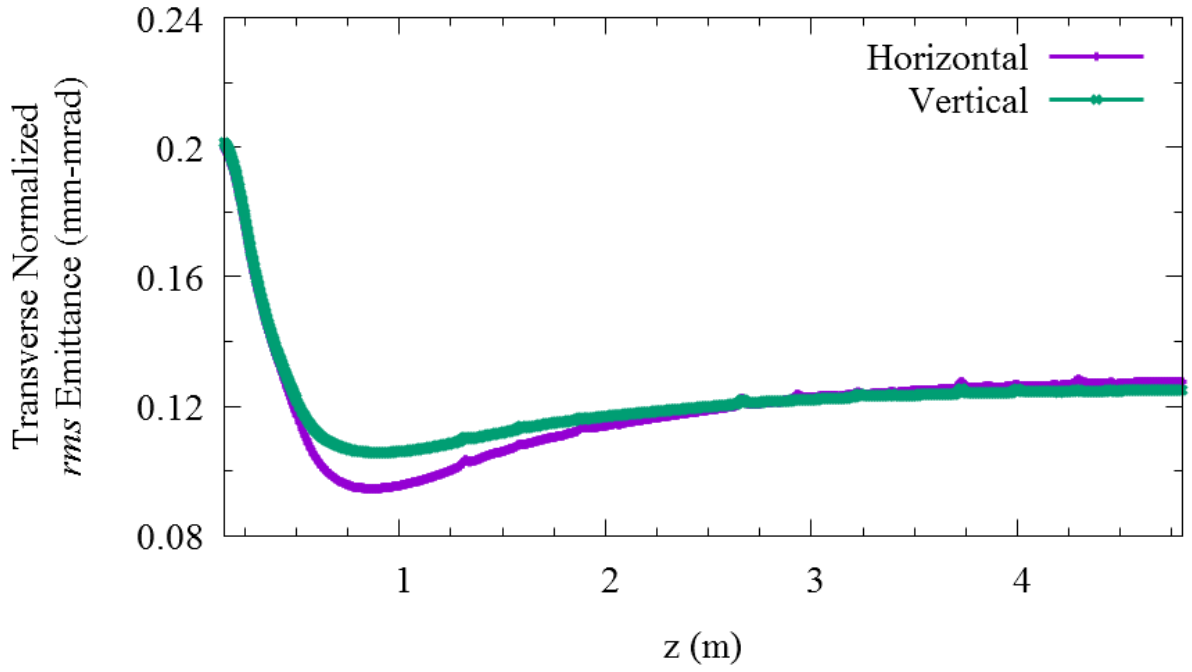

FIG. 30: Transverse normalized *rms* emittances of the final bunch off the cathode tracked through the second version of the accelerating section as a function of the longitudinal position.

CHAPTER 5

LINEAR ACCELERATOR

5.1 DOUBLE-SPOKE CAVITY

Until recently, accelerating electrons near the speed of light has not been attempted with multi-spoke cavities. This is largely because of the well-established and succesful performance of TM-type cavities. However, multi-spoke cavities are familiar options for accelerating ions. Previous studies of multi-spoke cavities for $\beta \sim 1$ strongly suggest that they are a viable option for accelerating electrons [75–79].

The four cavities which comprise the linac are double-spoke speed of light SRF cavities designed by Christopher Hopper in his ODU dissertation [80–82]. Fig. 31 contains an image of this cavity, with a portion cut away to more clearly view the interior structure. The accelerating field of this cavity is shown in Fig. 32. Select RF and physical properties are contained in Table 18.

One of the major design considerations for this cavity was the shape of the spoke. For the final design, a racetrack spoke shape was chosen, as it provides the best RF properties while providing a quality beam. Other choices considered were rounded square, ring, and elliptical spokes. All of these choices can be seen in Fig. 33, with the appropriate labels included in the caption.

5.2 TRANSVERSE CONSIDERATIONS

One aspect common for all spoke options is the "quadrupole-like" behavior of the cavities - the electron beam is focused in x and defocused in y, or vice versa by the accelerating mode [13, 82]. The degree of focusing each cavity provides depends on the choice of spoke. Regardless of the degree, this means that some adjustment is necessary to provide a round beam spot to the bunch compressor or final focusing section.

As the cavities behave like quadrupoles where the beam spot is concerned, it seems reasonable to arrange them as might be done for a set of four quadrupoles. In other words, orient them in the following order: focusing, defocusing, focusing, defocusing. The difference between a "focusing" and a "defocusing" cavity is determined by the direction of the spoke

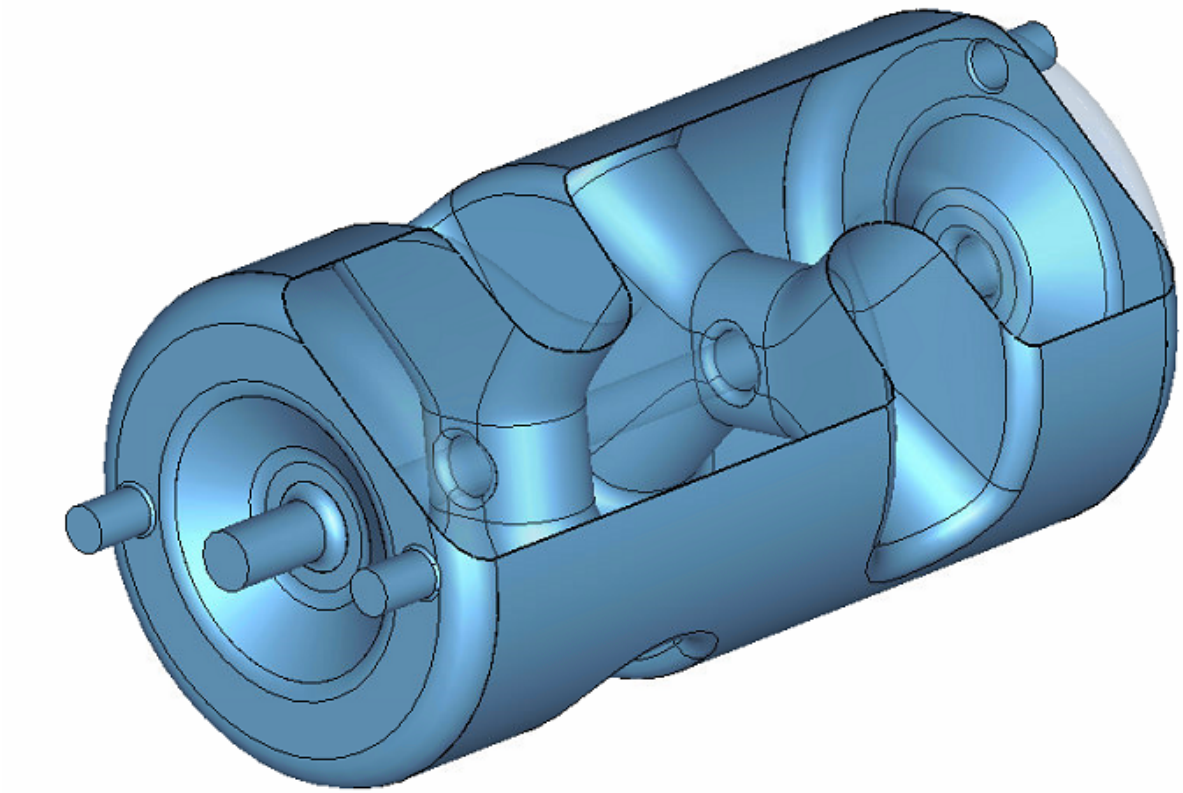

FIG. 31: The double-spoke SRF cavity, with a portion cut away to display the interior structure.

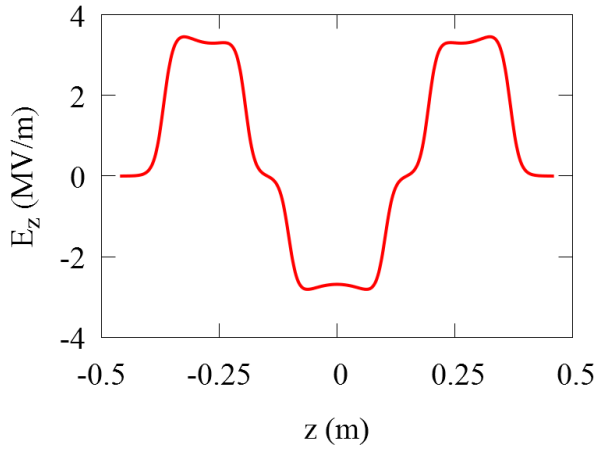

FIG. 32: The accelerating electric field along the beamline of the double-spoke SRF cavity.

TABLE 18: Physical (top) and RF (bottom) properties of double-spoke cavity.

Parameter	Quantity	Units
Frequency of accelerating mode	500	MHz
Frequency of nearest mode	507.1	MHz
Cavity diameter	416.4	mm
Iris-to-iris length	725	mm
Cavity length	805	mm
Reference length $[(3/2)\beta_0\lambda]$	900	mm
Aperture diameter	50	mm
Energy gain* at β_0	900	kV
R/Q	675	Ω
$QR_s^\dagger$	174	Ω
$(R/Q) \times QR_s^\dagger$	1.2×10^5	Ω^2
Peak electric surface field E_p^*	3.7	MV/m
Peak magnetic surface field B_p^*	7.6	mT
B_p^*/E_p^*	2.05	mT/(MV/m)
Energy content*	0.38	J
Power dissipation*†	0.87	W

*At $E_{\rm acc} = 1$ MV/m and reference length $(3/2)\beta_0\lambda$, $\beta_0 = 1$
†$R_s = 125$ nΩ

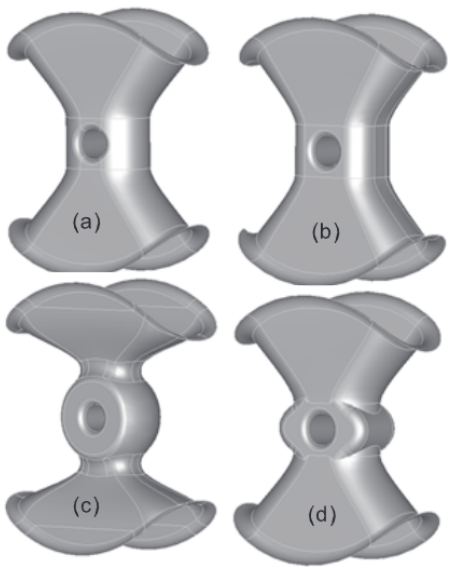

FIG. 33: The four options considered for spoke aperture geometry: (a) racetrack, (b) rounded square, (c) ring, and (d) elliptical.

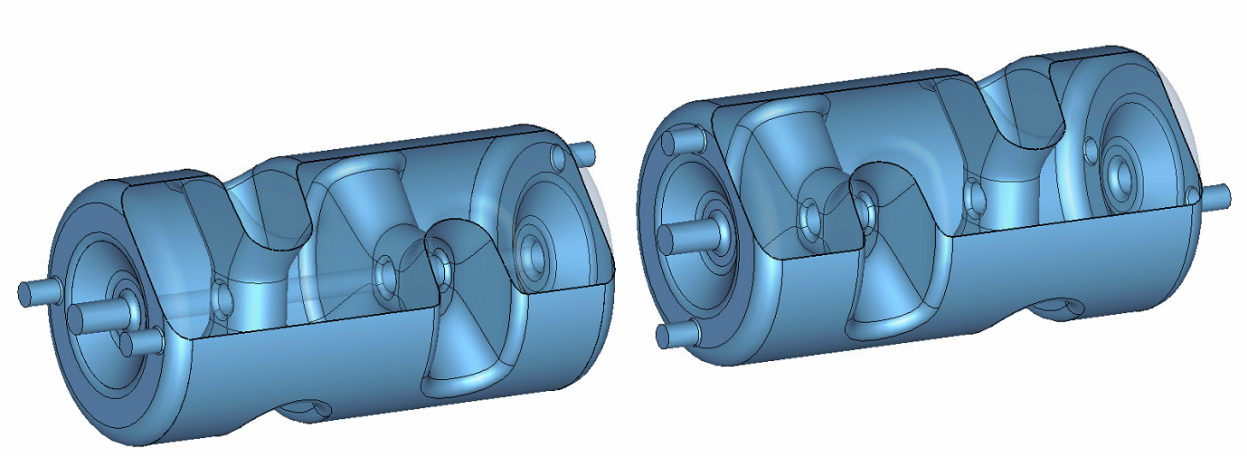

FIG. 34: Side-by-side comparison of focusing (left) and defocusing (right) double-spoke cavity. A beam passing from left to right first traverses a vertical (left, focusing) or horizontal (right, defocusing) spoke, depending on the orientation of the cavity.

which the beam first passes through within that cavity. The difference between the orientation for focusing and defocusing cavities is seen in Fig. 34, which puts one of each next to each other. Alternatively, the difference can be thought of as a rotation of 180° about the vertical axis in the center of the cavity. For completeness, many configurations were tried, varying both the number of reversed cavities and which ones were reversed. In the complete comparison however, the first approach produces the roundest beam spot. A comparison of the transverse sizes of the beam through both the typical and best linacs is shown in Fig. 35, with the resulting beam spots compared in Fig. 36.

5.3 FIRST ITERATION

The two main considerations for the longitudinal spacing of the spoke cavities is beam quality and floor footprint. The desire is to achieve the best possible beam, while the linac occupies the least amount of floor space. It was assumed that the minimum separation between RF structures for this purpose was 10 cm for structures within the same cryomodule and 30 cm for structures in adjacent cryomodules.

For the gap between the gun and the first spoke cavity it is necessary to keep the two structures as close together as possible, requiring them to occupy the same cryomodule. While the electron bunch is relativistic when it exits the gun, it is not sufficiently relativistic as to make the contributions due to space charge negligible. After the bunch exits the first double-spoke cavity, however, emittance increase due to space charge is negligible.

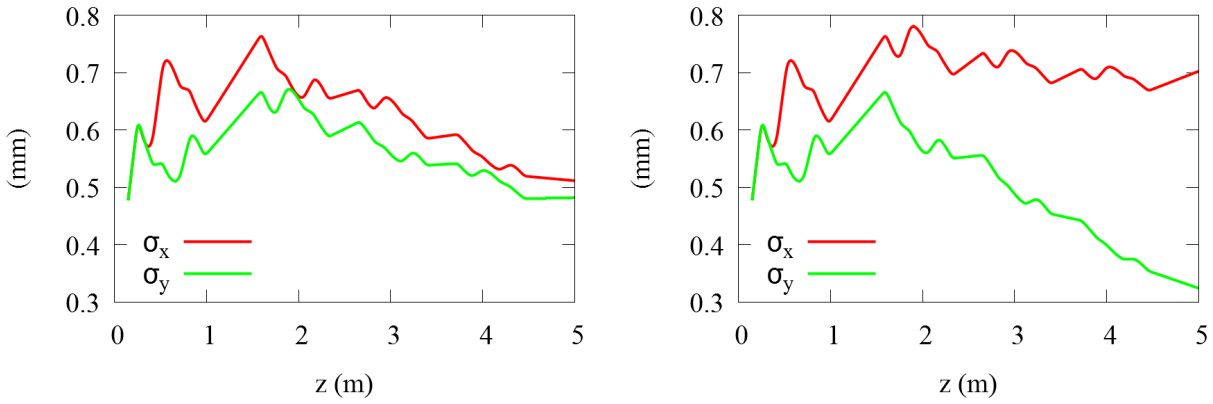

FIG. 35: The transverse sizes of the bunch through the linac with (left) and without (right) alternating orientation of cavities in the linac.

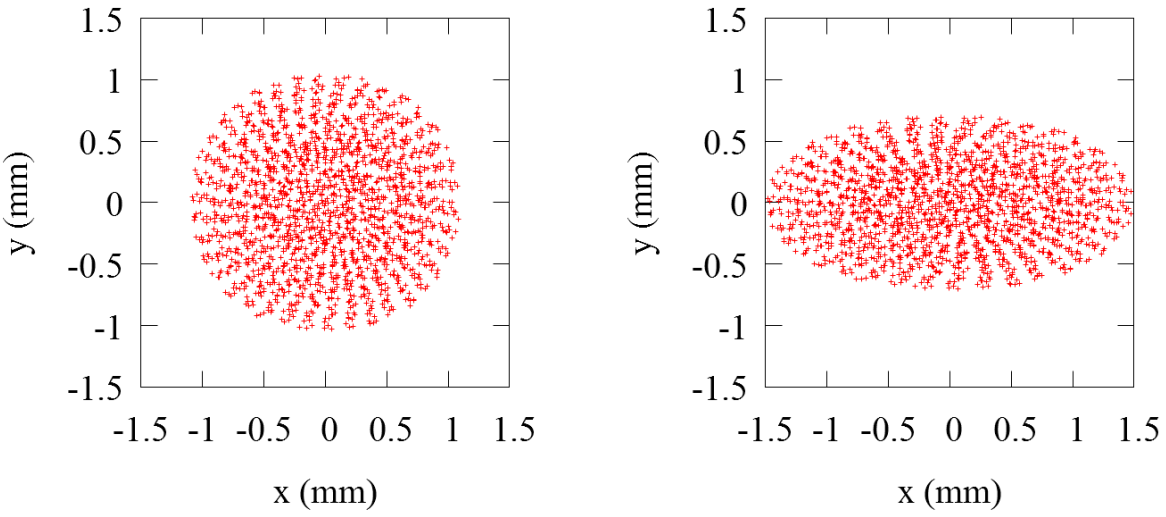

FIG. 36: The beam spots exiting the linac with (left) and without (right) alternating orientation of cavities in the linac.

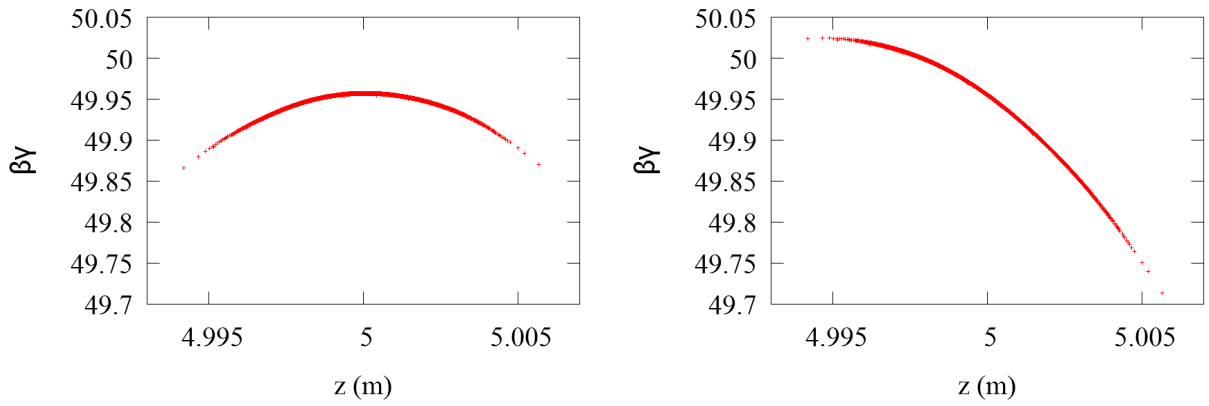

FIG. 37: The longitudinal phase space of the bunch exiting the linac without (left) and with (right) a chirp.

The subsequent spoke cavities were contained within two cryomodules - the second and third in one, and the last spoke cavity occupying the last one. In order for the bunch compressor to be most effective, the bunch needs to be chirped, meaning that the p_z of electrons within the bunch is correlated to the longitudinal position of the electrons. This is achieved by running the last two cavities of the linac off-crest 6.5°, which means that the phase for the cavity is not set to correspond to the highest average energy gain possible. A comparison of the longitudinal phase space of a non-chirped and chirped bunch is shown in Fig. 37.

Simulations show the "quadrupole"-like behavior of the spokes produce a round beam by passing the beam through cavities of alternating orientations. The first iteration of the accelerating section produces a simulated bunch at the exit of the linac with the properties shown in Table 19, with the transverse phase spaces and beam spot shown in Fig. 38.

5.4 SECOND ITERATION

The first difference between this design iteration and the initial one is the number of cryomodules. With only two cryomodules instead of three, the spacing between cavities within the linac are different than the previous version. The first cryomodule contains the gun followed by two double spoke cavities, with the last two cavities contained within the second cryomodule. The alternating orientation present in the previous iteration exists in this design as well.

Unlike the first iteration, running all cavities within the linac on-crest does not produce

TABLE 19: Properties of electron bunch at linac exit for the first design iteration.

Parameter	Quantity	Units
kinetic energy	25	MeV
rms energy spread	31.09	keV
$\epsilon^N_{x,\mathrm{rms}}$	0.16	mm-mrad
$\epsilon^N_{y,\mathrm{rms}}$	0.15	mm-mrad
σ_x	0.511	mm
σ_y	0.482	mm
β_x	82.1	m
β_y	75.5	m
α_x	2.34	-
α_y	-0.591	-
σ_z	2.1 (7)	mm (psec)

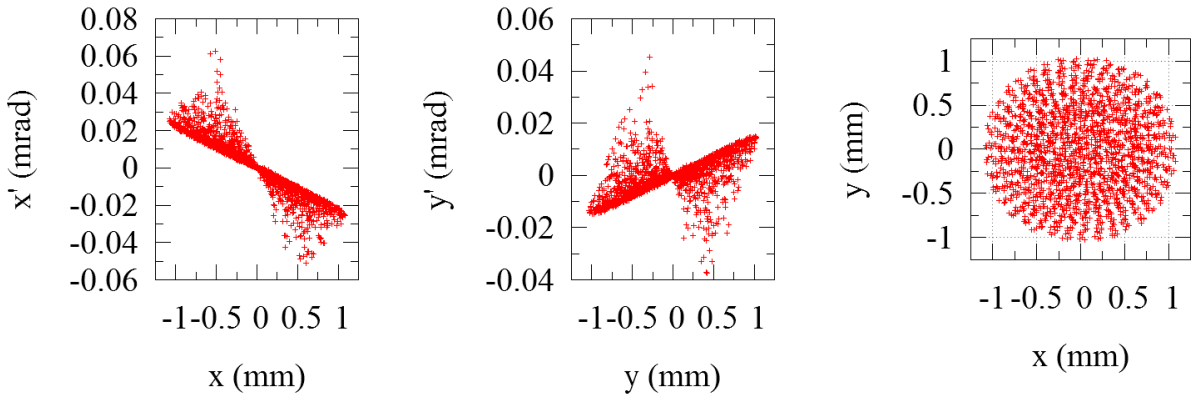

FIG. 38: Horizontal (left) and vertical (center) phase spaces and beam spot (right) of bunch after exiting the linac in the first design iteration.

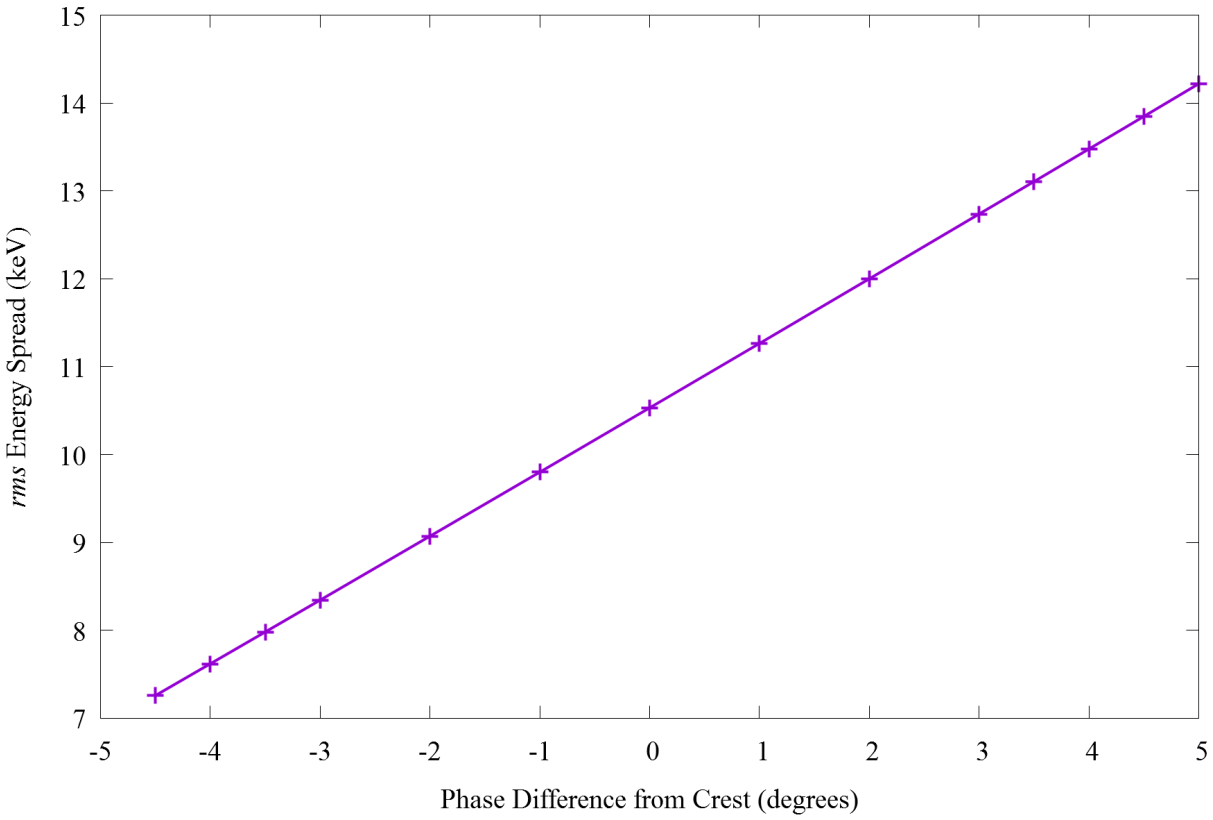

FIG. 39: The *rms* energy spread of the bunch exiting the linac as a function of the phase off-crest of the last two cavities.

the smallest energy spread. In order to meet the *rms* energy spread requirement, it is necessary for the last two cavities in the linac to run off-crest $-4.5°$. Shown in Fig. 39 is the *rms* energy spread of the bunch as a function of the phase off-crest at which the last two cavities run.

Taking the bunch which has emerged from the second iteration of the gun and tracking it through this design of the linac results in the bunch exiting the linac with the properties shown in Table 20. Because of the significantly shorter bunch length off the cathode and thus out of the gun, the length of the bunch is much shorter than called for in the original target goals, removing the necessity of a bunch compressor. Unlike the first version, the *rms* energy spread does meet the target goal. The transverse normalized *rms* emittances, however, do not meet the target specifications and are larger than those of the first iteration bunch exiting the linac. While the spot size of the beam is reasonable, it is increasing rapidly.

5.5 FINAL DESIGN

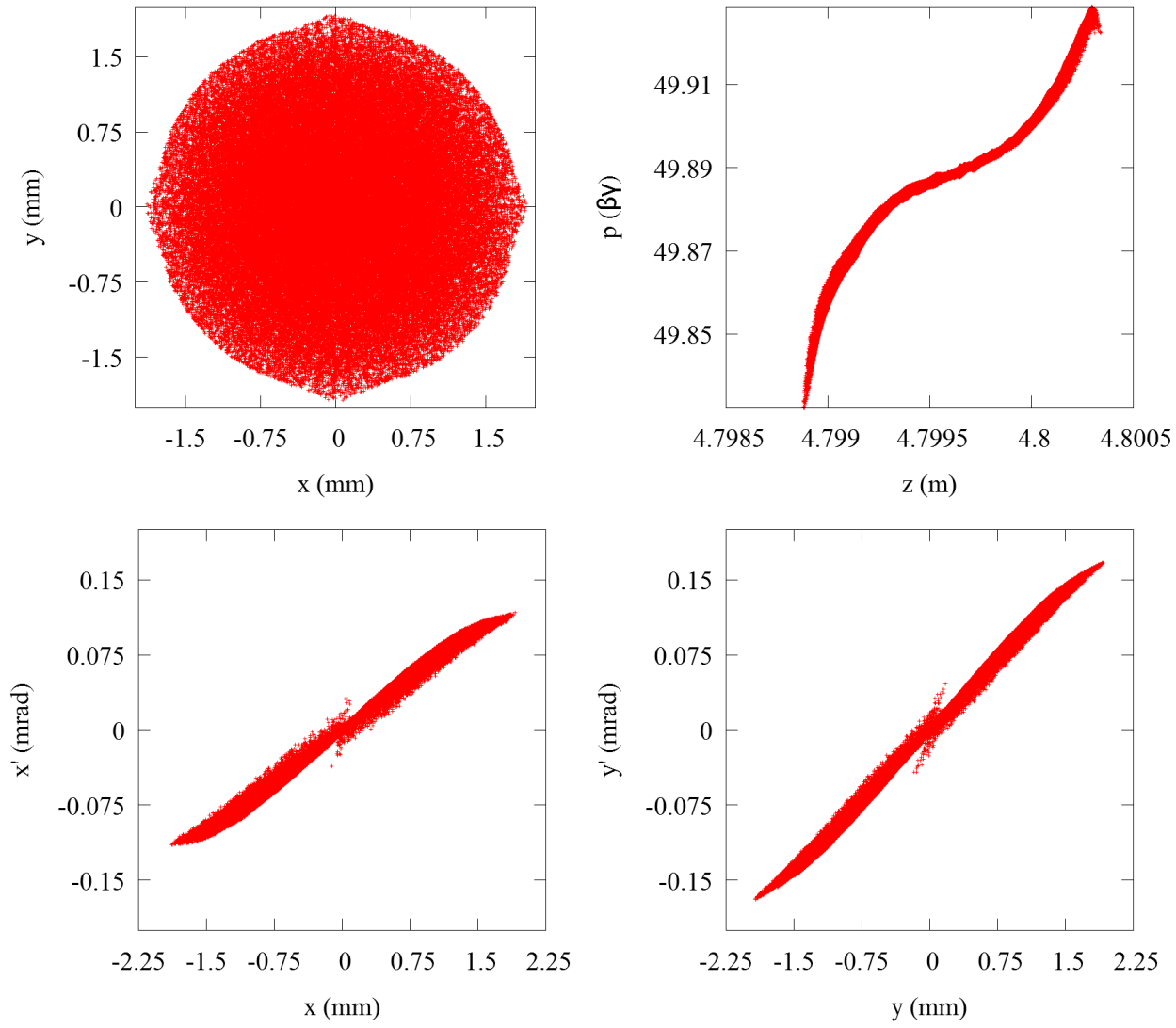

FIG. 40: Beam spot (upper left), longitudinal phase space (upper right), horizontal phase space (bottom left), and vertical phase space (bottom right) of bunch after exiting the linac in the second design iteration.

TABLE 20: Properties of electron bunch at linac exit for the second design iteration.

Parameter	Quantity	Units
kinetic energy	25.	MeV
rms energy spread	7.25	keV
$\epsilon^N_{x,\mathrm{rms}}$	0.19	mm-mrad
$\epsilon^N_{y,\mathrm{rms}}$	0.17	mm-mrad
σ_x	0.76	mm
σ_y	0.76	mm
β_x	154	m
β_y	171	m
α_x	-11	-
α_y	-16	-
σ_z	0.35	mm

While the number of cryomodules and spacing between subsequent SRF structures remains constant, the orientation of the spoke cavities changes in the final design. Instead of the alternating orientation of subsequent cavities, which can be thought of as focusing, defocusing, focusing, defocusing, the orientation of the spoke cavities is now focusing, defocusing, defocusing, focusing. For clarity, Fig. 41 shows the accelerating section for both the second and final iterations next to each other. The last two cavities are run -4° off-crest. The reason for this alteration to the orientation is that it produces a smaller beam (of approximately the same aspect ratio) at the exit of the linac.

Tracking of the bunch which exits the final iteration of the gun design results in a simulated bunch exiting the linac with the properties shown in Table 21. The significant differences between these results and those of the previous iteration, seen in Table 20, are due to the alteration of the gun design and the initial bunch produced by the cathode. The change in orientation of the final two spoke cavities merely produces the smallest, roundest beam at the linac exit. Ignoring the transverse sizes of the bunch, which will be altered in the focusing section, the only property that does not match the initial target goal is the vertical normalized *rms* emittance. The spot size is again reasonable for focusing to a small spot size and while increasing, is not increasing rapidly.

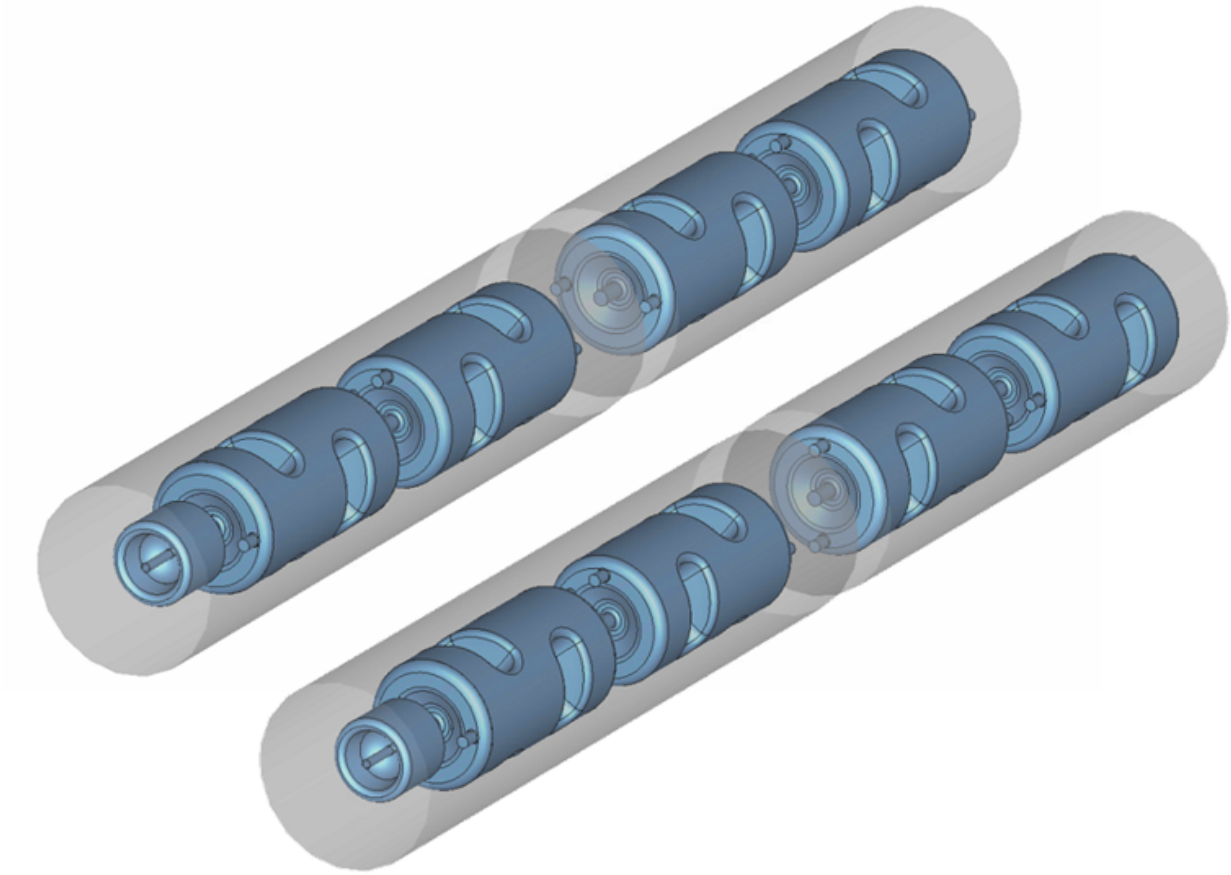

FIG. 41: The accelerating section layout of the second (top left) and final (bottom right) design iterations. Note that while the spacing between structures remains the same, the orientations of the last two spoke cavities has been switched.

TABLE 21: Properties of electron bunch at linac exit for the final design iteration.

Parameter	Quantity	Units
kinetic energy	25.	MeV
rms energy spread	3.44	keV
$\epsilon^N_{x,\mathrm{rms}}$	0.10	mm-mrad
$\epsilon^N_{y,\mathrm{rms}}$	0.13	mm-mrad
σ_x	0.35	mm
σ_y	0.38	mm
β_x	60	m
β_y	54	m
α_x	-2.3	-
α_y	-3.8	-
σ_z	0.67	mm

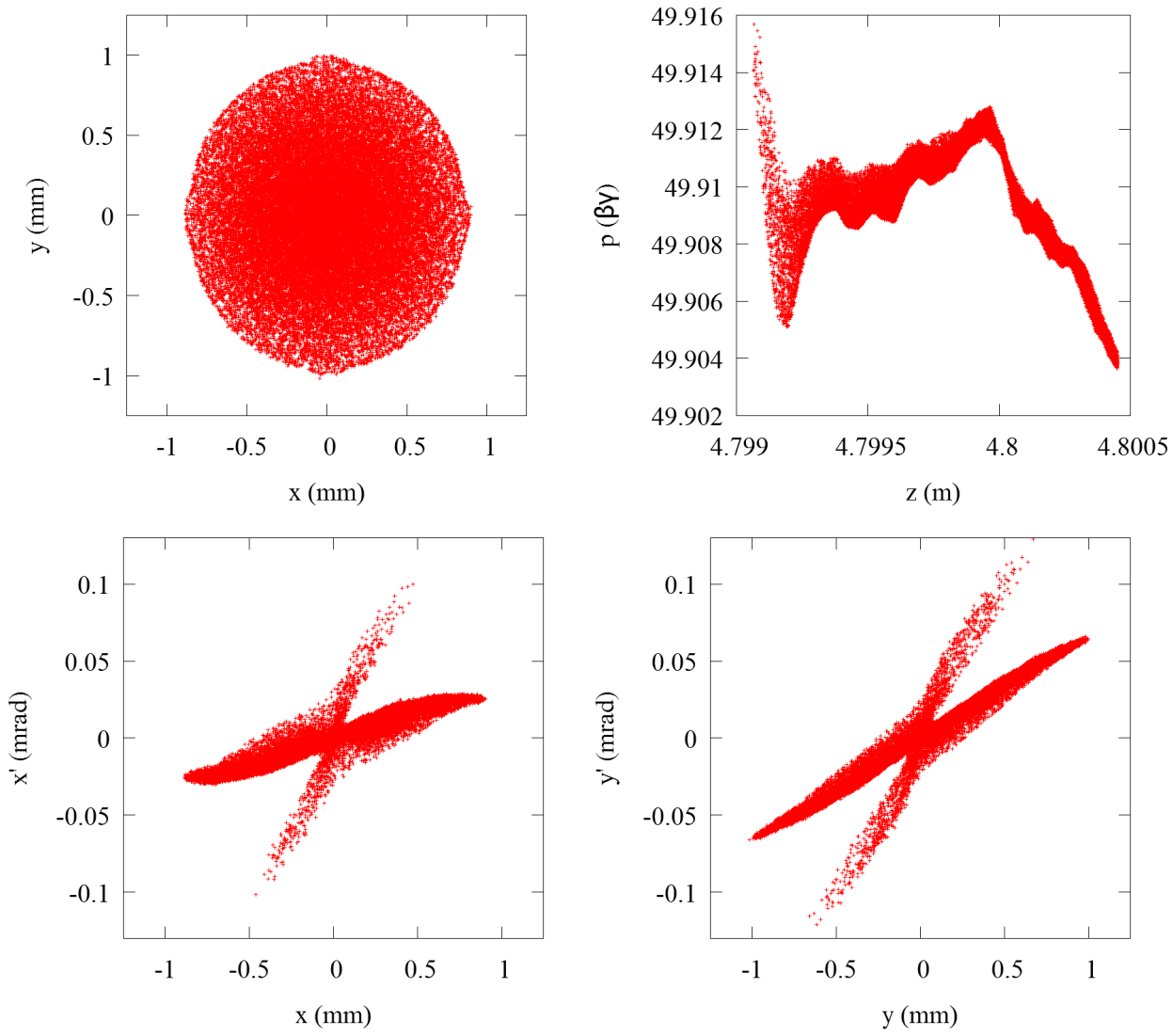

FIG. 42: Beam spot (upper left), longitudinal phase space (upper right), horizontal phase space (bottom left), and vertical phase space (bottom right) of bunch after exiting the linac in the final design iteration.

CHAPTER 6

BUNCH COMPRESSION

6.1 INITIAL DESIGN

Randika Gamage and Todd Satogata began the design of the magnetic bunch compressors considered for this system. They developed two options of 4-dipole s-chicane compressors, with tunable R_{56}, followed by an independent section to provide the final focusing down to a small spot size. One design, referred to as 3π for the net phase advance given to the beam traversing it, has a net bend of 90°. The second design provides a net phase advance of 4π, with no net bend. The basic layout of both the 3π and 4π designs are shown in Fig. 43 [26, 66, 83].

One thing to note is the lack of sextupoles in either design. Including sextupoles at points of high dispersion removes curvature of the longitudinal phase space, provided it is done correctly [84]. In the original requirements of the bunch compressor, sextupoles were specifically mentioned to be included in future iterations, precisely for this purpose [26].

6.2 FIRST ITERATION

When the bunch exiting the linac was tracked through the bunch compressor and final focus options provided using `elegant`, a number of problems were evident. First, while the compressors were achromats for bunches produced by `elegant` (the bunch exited the lattice with $D_x, D'_x = 0$), when the bunch exiting the linac was tracked through the lattice, the bunch exiting the compressor had a nonzero horizontal dispersion (D_x) and a nonzero rate of change of the horizontal dispersion (D'_x). Second, the transverse normalized *rms* emittances were blowing up within the compressor. Both of these were significant, for different reasons. In order to achieve a small spot size at the IP, the bunch exiting the compressor needs to satisfy the conditions $D_x, D'_x = 0$ [26]. Preserving an extremely small emittance was and is necessary to produce the high average brilliance desired in the X-ray source.

Fortunately, solving the first problem was straightforward. Running `elegant` with the actual bunch exiting the linac and adjusting the strength of the center quadrupole within the lattices produced an achromatic bunch exiting the compressors. Unfortunately, the problem of emittance blow up did not have a simple solution.

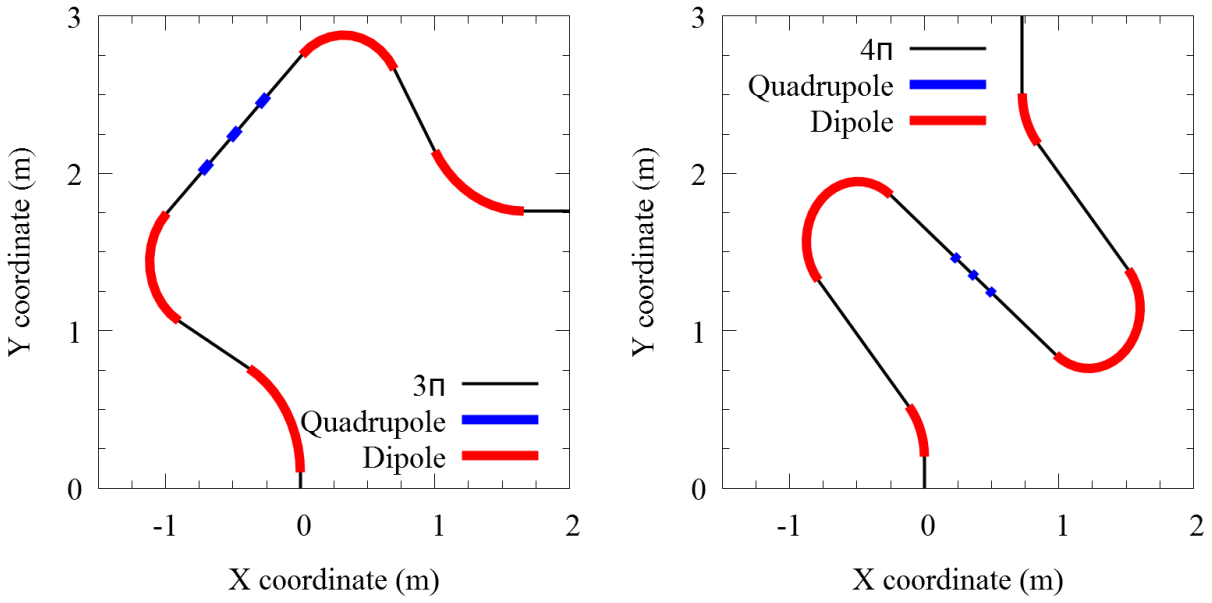

FIG. 43: Basic layout of both the 3π (left) and 4π (right) compressor designs. Bunch enters at (0,0).

6.2.1 SOLENOID

The idea that the "bow-tie" shape of the transverse phase spaces were a contributing factor to the emittance growth within the bunch compressor was explored. To that end, a solenoid was placed down stream from the linac, given the known applicability of solenoids in transverse phase space compensation [55]. Passing the bunch through a solenoid increased the emittance, when measured immediately after the solenoid. However, the emittance decreased to the value prior to entering the solenoid after a sufficient drift length.

As the strength of the solenoid increases, the growth of the transverse emittance the bunch experiences increases as well. Additionally, as the solenoid strength increases, the transverse phase spaces of the bunch exiting the solenoid more closely resemble an ellipse. This relationship between solenoid strength and resulting phase spaces can be seen in Fig. 44, which shows the phase spaces of an identical initial bunch after it has been passed through solenoids of varying strengths. The initial bunch is the bunch exiting the initial version of the linac, shown in Fig. 38.

Additionally, a quadrupole was placed after the solenoid and tuned so that $\alpha_x = \alpha_y$ and $\beta_x \approx \beta_y$ heading into the compressor. The transverse phase spaces of the bunch after the quadrupole are shown in Fig. 45, with select transverse properties after both the solenoid

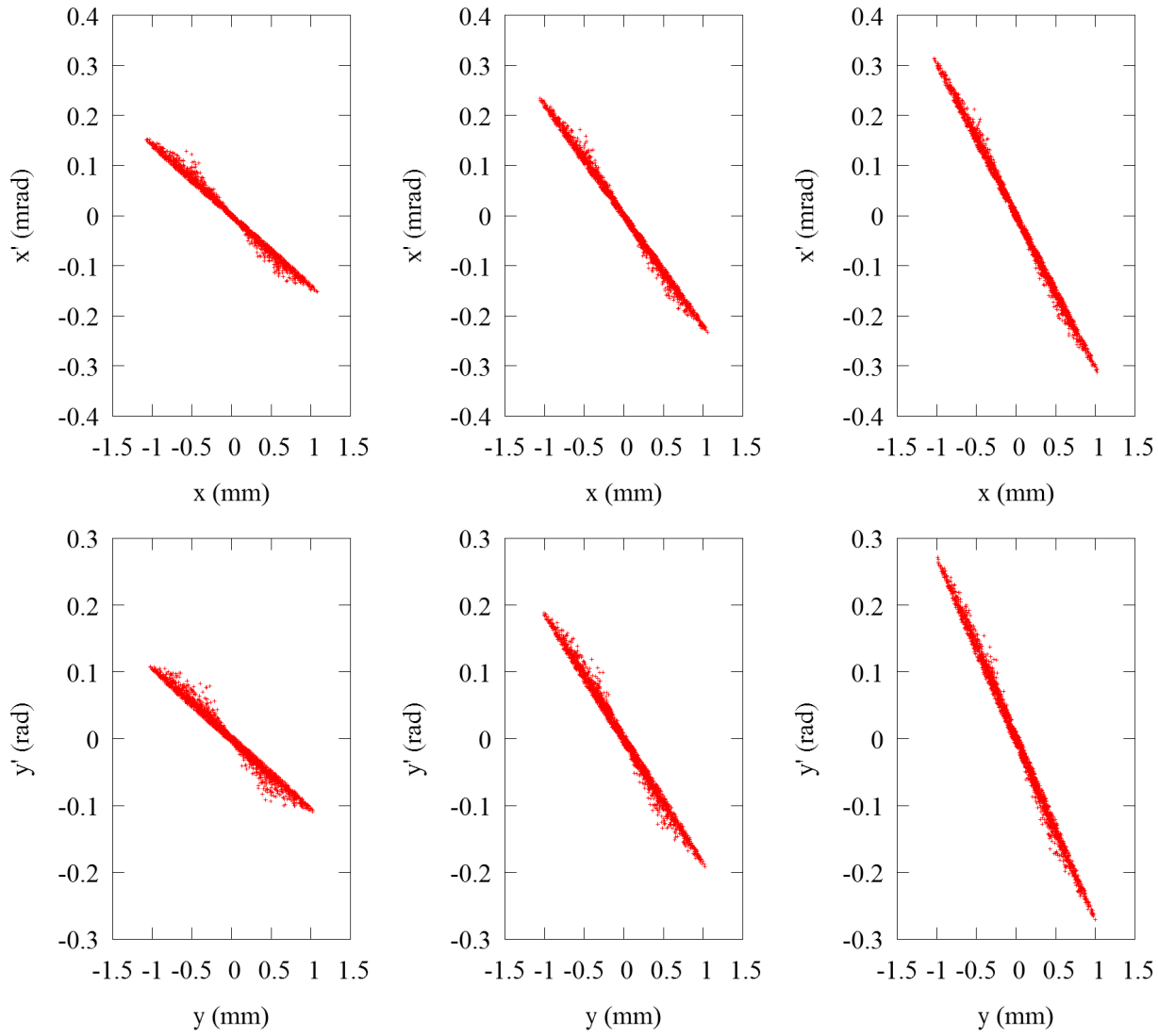

FIG. 44: The horizontal (top row) and vertical (bottom row) phase spaces of a bunch exiting a solenoid of increasing strength (left to right).

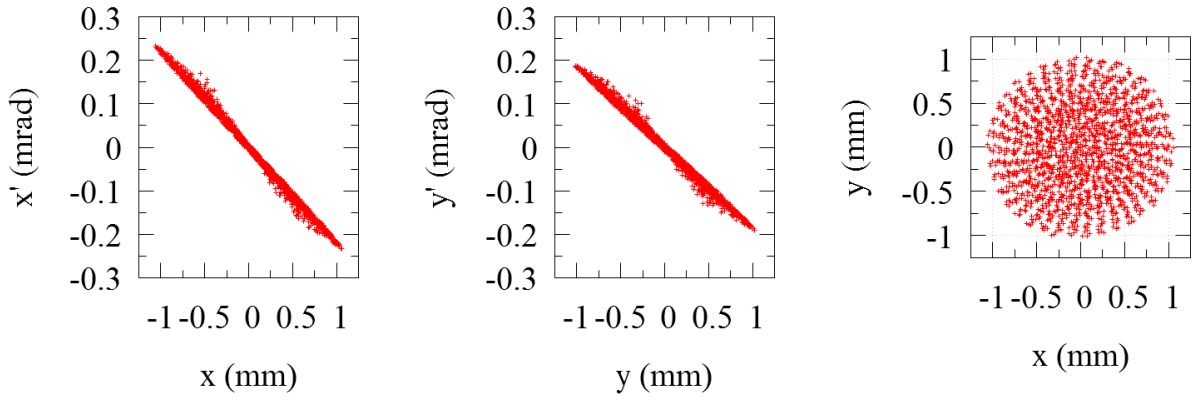

FIG. 45: Horizontal (left) and vertical (center) phase spaces and beam spot (right) of bunch after exiting the quadrupole following the solenoid for the first design iteration.

TABLE 22: Properties of electron bunch immediately after the solenoid (inner left) and quadrupole (inner right) for the first design iteration.

Parameter	After Solenoid	After Quadrupole	Units
$\epsilon^N_{x,\mathrm{rms}}$	0.19	0.19	mm-mrad
$\epsilon^N_{y,\mathrm{rms}}$	0.18	0.18	mm-mrad
σ_x	0.50	0.38	mm
σ_y	0.47	0.39	mm
β_x	65	38	m
β_y	61	39	m
α_x	15	10	-
α_y	12	10	-

and the quadrupole shown in Table 22.

While the solenoid did have some benefit towards limiting the growth of the emittance within the compressor, these effects were limited. Much more significant was taking the beam out of the linac and transforming it into a bunch which kept its roughly circular beam spot with drift, while making it focus in both transverse directions at the same rate.

6.2.2 FIRST INTRODUCTION OF SEXTUPOLES

At this point, the current layout for both compressors was similar to that shown in Fig. 43, with the addition of a solenoid and quadrupole after the linac but before the first

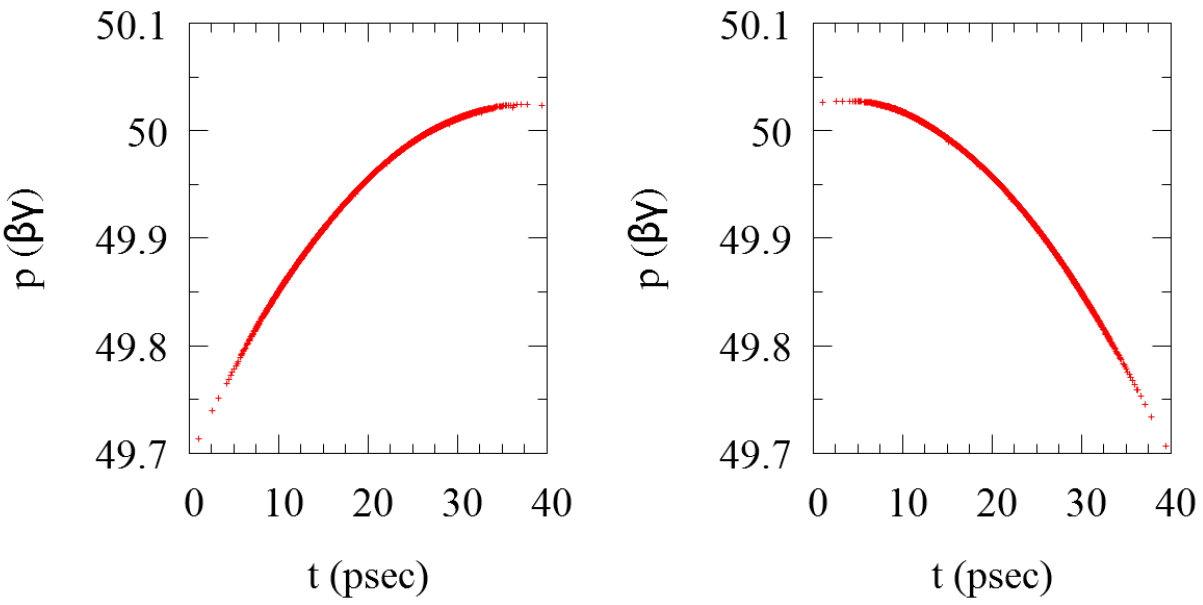

FIG. 46: A negative chirp in the longitudinal phase space going into the 3π compressor (left) and a positive chirp in the longitudinal phase space going into the 4π compressor (right).

dipole. The R_{56} of the 3π compressor is -1.53 m, while the R_{56} of the 4π compressor is 1.60 m. The fact that the R_{56} values of the compressor have different signs signifies that they each require a different chirp direction. The longitudinal phase spaces going into both compressors are shown in Fig. 46.

When placing the sextupoles, a typical approach is to place sextupoles of opposite strengths at the points of highest (horizontal) dispersion [26, 84]. To demonstrate these locations within each compressor design, Fig. 47 shows the horizontal dispersion along the beam path for both compressors, with the locations of the elements within the lattice indicated along the horizontal axis. Consequently, it seems reasonable to place a sextupole on either side of the inner set of quadrupoles for both designs. The location of sextupoles in each design are not necessarily the points of highest dispersion, but are sufficiently high.

The resulting longitudinal phase space for both compressor designs are shown in Fig. 48, as well as the distribution of macroparticles in the longitudinal direction. Note that the curvature removal is much more effective in the 4π compressor than the 3π compressor. At this point, select properties of both compressor designs and bunch properties at the exit of the compressors is given in Table 23.

From Fig. 48, it appears that the curvature removal from the longitudinal phase space is

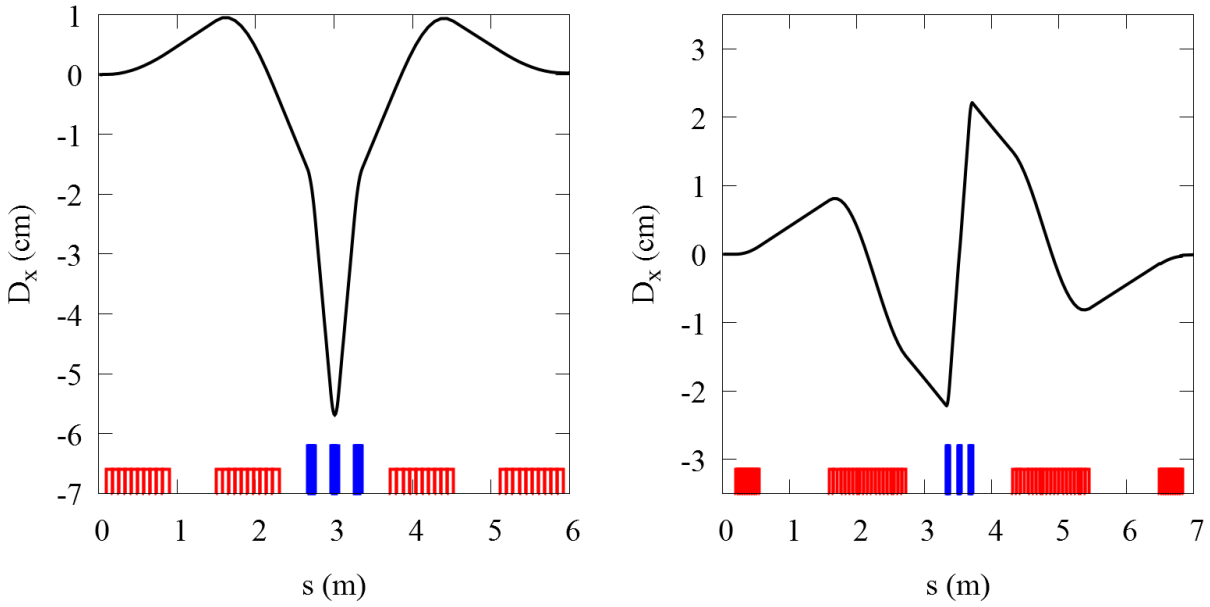

FIG. 47: Dispersion as a function of beam path s for both the 3π (left) and 4π (right) compressors.

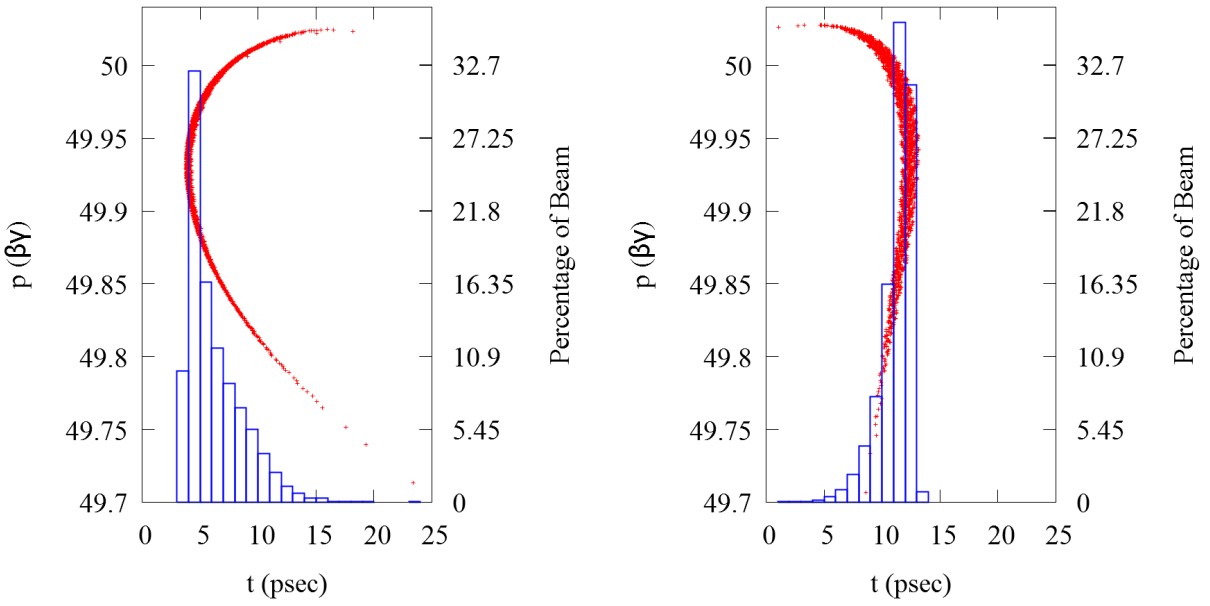

FIG. 48: Longitudinal phase space and distribution for bunches exiting both the 3π (left) and 4π (right) compressors.

TABLE 23: Selected properties of compressor (top) and the bunch exiting the compressor (bottom) for both the 3π (left) and 4π (right) designs.

Parameter	3π	4π	Units
R_{56}	-1.53	1.60	m
Dipole Angles	60, -105, -105, 60	40, -170, 170, -40	°
Dipole Lengths	0.8, 0.8, 0.8, 0.8	0.35, 1.1, 0.35, 1.1	m
β_x	24	7.1	m
β_y	925	350	m
$\epsilon^N_{\mathrm{rms},x}$	0.4	3	mm-mrad
$\epsilon^N_{\mathrm{rms},y}$	0.5	2	mm-mrad
σ_x	0.46	0.66	mm
σ_y	3	4.2	mm

only working for the 4π design, despite sextupoles being included similarly in both compressors. However, as the longitudinal phase spaces at the compressor exit remain approximately the same even after the sextupoles are removed from the lattice, it is evident that the sextupoles are not the source of the curvature removal apparent in the 4π design. Further simulation shows that the curvature removal exhibited in the 4π design is a consequence of second-order correction existing within the lattice. Attempting to alter the second-order correction of the 3π lattice without sextupoles proved to be unproductive.

6.2.3 COUPLING

It was suggested that one reason for emittance blow-up within the compressor was some transverse (xy or $x'y'$) coupling of the beam [85]. The presence of coupling, in either the xy or $x'y'$ planes, can be manipulated with skew quadrupoles, quadrupoles that have been rotated 45° [15]. The use of a solenoid introduces $x'y'$ coupling into the beam, but this coupling can be removed by placing a skew quadrupole of appropriate strength after the solenoid.

6.2.4 SECOND APPROACH OF SEXTUPOLES

Of the two longitudinal phase spaces shown in Fig. 48, the one exiting the 3π compressor is most in need of curvature removal. Additionally, the effects of the sextupoles are more apparent when tracking a bunch through the 3π compressor design instead of the 4π design.

TABLE 24: Selected properties of compressor (top) and the bunch exiting the compressor (bottom) for both the 3π (left) and 4π (right) designs with an uncoupled incoming bunch.

Parameter	3π	4π	Units
R_{56}	-1.52	1.39	m
Dipole Angles	60, -108, -108, 60	40, -180, 180, -40	°
Dipole Lengths	0.8, 0.8, 0.8, 0.8	0.35, 1.1, 1.1, 0.35	m
β_x	18	13	m
β_y	396	532	m
$\epsilon^N_{\mathrm{rms},x}$	0.7	0.6	mm-mrad
$\epsilon^N_{\mathrm{rms},y}$	0.5	0.16	mm-mrad
σ_x	0.49	0.39	mm
σ_y	1.9	1.3	mm

The initial approach to placing sextupoles had been at points of high dispersion, which is insufficient in this case. Taking guidance from [15], it became evident that what was critical was the separation of the sextupoles. In order to achieve curvature removal, the sextupoles need to be separated by a π phase advance within the compressor [15]. The phase advance of the bunch within the 3π compressor is shown in Fig. 49, with the structures of the lattice indicated along the bottom horizontal axis. After studying this plot, it is apparent that to properly place the sextupoles requires breaking the symmetry of the lattice. One sextupole is located immediately after the second dipole, while the other is immediately after the third dipole.

Skew quadrupoles are placed within the compressor to remove coupling, but skew quadrupoles placed at points of non-zero horizontal dispersion can produce vertical dispersion [86]. Fortunately, the set strength necessary of these skew quadrupoles to remove the existing coupling throughout the compressor is so low that no vertical dispersion is generated to first order.

An additional quadrupole is placed after the second sextupole, so that the bunch exiting the compressor is achromatic. The footprint of the new design is shown in Fig. 50, with the select compressor and bunch properties given in Table 25.

6.2.5 *RMS* ENERGY SPREAD AND THE MOTIVATION FOR THE SECOND ITERATION

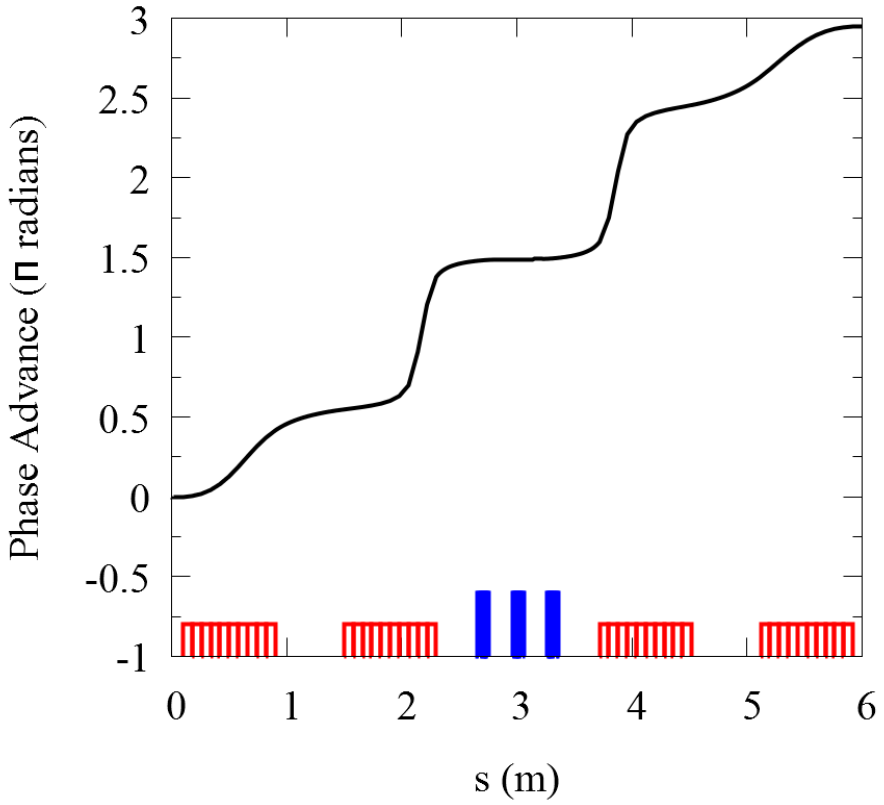

FIG. 49: Phase advance of the 3π compressor as a function of beam path, with the positions and elements of the compressor shown along the horizontal axis.

TABLE 25: Selected properties of compressor (top) and the bunch exiting the compressor (bottom) for the 3π compressor with curvature removal.

Parameter	Quantity	Units
R_{56}	-2.1	m
Dipole Angles	60, -105, -105, 60	°
Dipole Lengths	0.52, 0.92, 0.92, 0.52	m
β_x	5.9	m
β_y	3.8	m
$\epsilon^N_{\mathrm{rms},x}$	5.2	mm-mrad
$\epsilon^N_{\mathrm{rms},y}$	0.4	mm-mrad
σ_x	0.78	mm
σ_y	0.17	mm

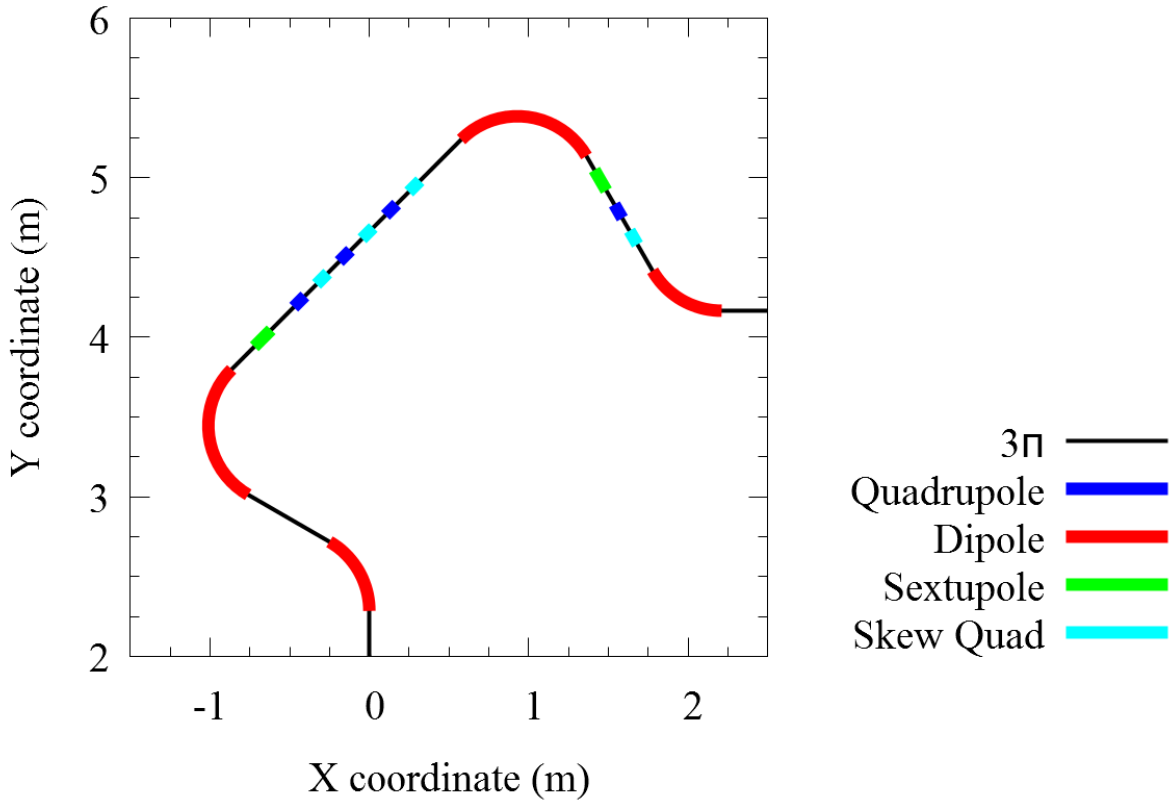

FIG. 50: Floor plan of the 3π compressor design with working curvature removal. Bunch enters at (0,2).

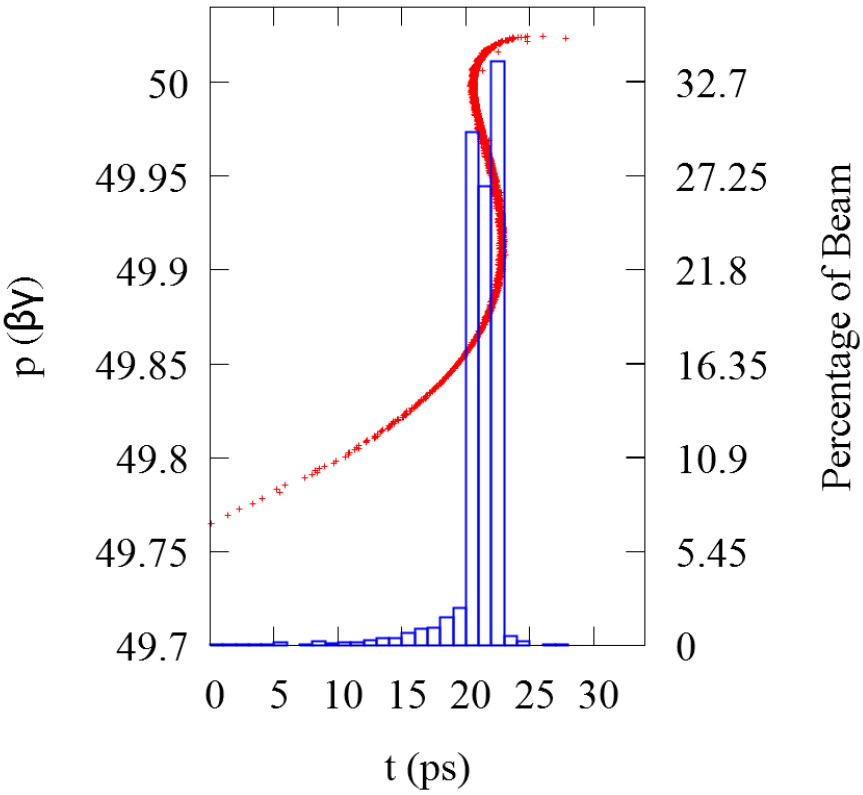

FIG. 51: Longitudinal phase space and distribution of bunch exiting 3π compressor with curvature removal.

As was noted in the previous chapter, the bunch exiting the linac has an *rms* energy spread more than four times the desired value. Additionally, this parameter of the beam is not one which can be altered by compressor elements which have previously been mentioned - solenoid, quadrupole, dipole, or sextupole.

When the *rms* energy spread of the bunch exiting the linac was artificially reduced by a factor of 4, results in both compressor options significantly improved, even without altering the components. The most notable effects were that emittance growth either decreased or disappeared and the betatron coupling was no longer a concern, to first order. While both compressor lattices would have benefited from fine tuning, the results were significantly supportive of bunch compression with emittance growth.

Even if bunch compression could be achieved for a bunch with the actual *rms* energy spread without emittance growth and was capable of being focused down to the desired spot size, the hourglass effect would reduce the brilliance of the generated X-ray beam [12]. Additionally, as the emittance exiting the linac was larger by at least 50% in both directions, the brilliance would be reduced by at least an order of magnitude, even without taking the reduction due to the hourglass effect into account. Overall, there seemed to be sufficient room for improvement of the transverse emittance and the *rms* energy spread of the bunch exiting the linac. In order to correct the *rms* energy spread, a shorter bunch off the cathode was called for, which eventually developed into the second design iteration.

6.3 ALPHA MAGNET

An alpha magnet was also considered as an option for compressing the bunch [26]. In this scheme, compression occurs at lower energy, typically between the gun and the linac [87]. This approach has the benefit of less required floor space and removes the need to chirp the beam exiting the linac. First described by Enge, the alpha magnet is half of a quadrupole magnet, with a vertical mirror plane [88]. This mirror plane produces the "quadrupole-like" fields within the magnet [88]. Instead of passing through the magnet, perpendicular to the front plate, the beam enters at an angle. While particles of different energies have different trajectories within the magnet, all particles exit at the same location and angle. These trajectories are shown in Fig. 52, displaying the shape which earned the concept its name [13, 87].

Because the bending is done at low energy, concerns exist about space charge and preserving the transverse normalized *rms* emittance [26]. Prior work with a bunch of 20 pC at 2.15 MeV exhibits significant emittance growth [89]. As this is comparable to the bunch

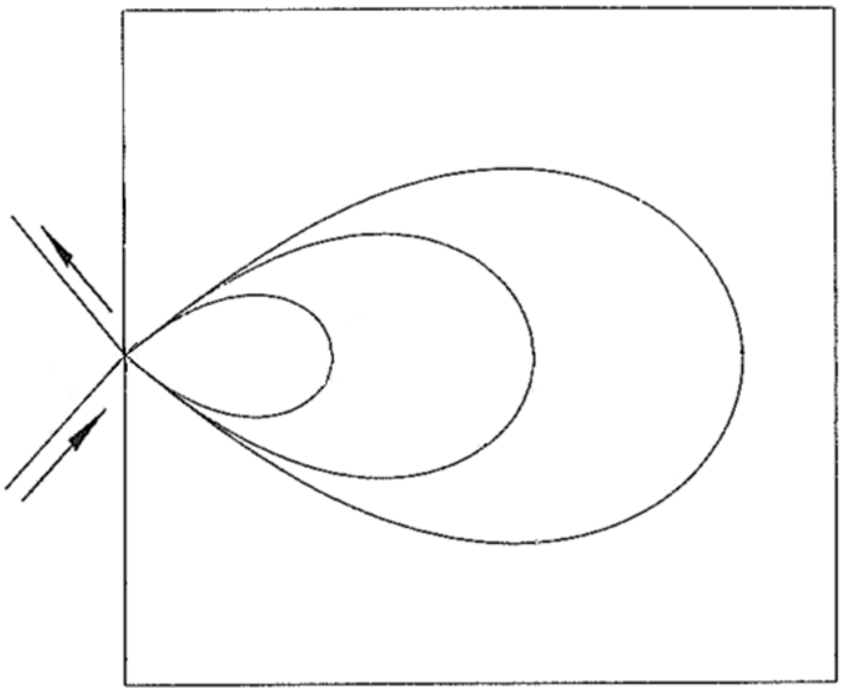

FIG. 52: Trajectories of beam through alpha magnet.

exiting the gun with 10 pC at ∼1.5 MeV, placing an alpha magnet immediately after the gun is unsuitable for producing and maintaining our small emittance value. Placing the alpha magnet after the first double-spoke cavity, where the beam has a kinetic energy of ∼7.3 MeV, may remove emittance growth due to space charge from concern. Due to the decrease of $\epsilon^N_{\mathrm{rms},x}$ through the entire linac for later versions, simulations need to take space charge into account in order to be accurate. As a compressor became unnecessary for later designs, the idea of using an alpha magnet was not pursued.

6.4 SECOND AND FINAL DESIGNS

In the second and final designs, a bunch compressor proved to be unnecessary because the bunch exiting the linac was already sufficiently short. This allows for a more compact and simpler overall design, which is desirable. The drawback is that without the bunch compressor it becomes more difficult to manipulate the longitudinal phase space, without altering other beam properties. By changing the chirp in the last two cavities of the linac, some manipulation is possible, though the effects are limited.

CHAPTER 7

FINAL FOCUSING

7.1 FIRST ITERATION

For the first iteration of the design, the bunch compressor was followed by a final focusing section. This approach has the benefit that simultaneous compression and focusing is not required. The bunch at the IP for the different bunch compressors presented in the previous chapter is shown in Tables 26, 27, and 28, corresponding to the initial compressor, the introduction of skew quadrupoles, and adding curvature removal, respectively.

What is common in the results for all of the proposed compressors is that the parameters of the beam at the IP fall far short of the desired values. A large beam spot leads to a decrease in the anticipated flux and average brilliance of the X-ray beam, while a larger transverse normalized *rms* emittance decreases the average brilliance. As the high average brilliance is the most attractive feature in such a compact Compton light source, it is disappointing that none of these designs are sufficient to produce the desired beam. Taken together with the poor results immediately after the bunch compressor for all designs, which can be corrected with a significantly smaller *rms* energy spread, the decision was made to significantly alter the design, particularly in the front end of beam formation. This alteration process lead to the second design iteration.

TABLE 26: Selected properties of the bunch at the IP for both the 3π (left) and 4π (right) designs.

Parameter	3π	4π	Units
β_x	5	8	mm
β_y	3	6	mm
$\epsilon^N_{\mathrm{rms},x}$	0.4	20	mm-mrad
$\epsilon^N_{\mathrm{rms},y}$	0.7	450	mm-mrad
σ_x	6	56	μm
σ_y	6	230	μm

TABLE 27: Selected properties of the bunch at the IP for both the 3π (left) and 4π (right) designs with skew quadrupoles.

Parameter	3π	4π	Units
β_x	5	6	mm
β_y	8	11	mm
$\epsilon^N_{\mathrm{rms},x}$	0.6	0.6	mm-mrad
$\epsilon^N_{\mathrm{rms},y}$	0.3	1.4	mm-mrad
σ_x	7	9	μm
σ_y	8	18	μm

TABLE 28: Selected properties of the bunch at the IP for the 3π design with curvature removal.

Parameter	Quantity	Units
β_x	6	mm
β_y	6	mm
$\epsilon^N_{\mathrm{rms},x}$	2.2	mm-mrad
$\epsilon^N_{\mathrm{rms},y}$	0.8	mm-mrad
σ_x	16	μm
σ_y	10	μm

7.2 SECOND ITERATION

While the initial target specifications called for FWHM of 3 ps in regards to the longitudinal distribution of the bunch, that assumes the bunch has a gaussian distribution, which is not the case. Consequently, it is necessary to compare the percentage of the bunch contained within a given range. A one-dimensional Gaussian function is given by

$$f(x) = \frac{1}{\sigma\sqrt{2\pi}} e^{-(x-\mu)^2/(2\sigma^2)}. \tag{65}$$

It is relatively straightforward to show that the bounds of the FWHM are located at $x = \pm\sigma\sqrt{2\ln 2} + \mu$ [38]. Integrating the Gaussian function between these coordinates, one finds that $\sim$76% of the distribution is contained within the range defined by the FWHM of the distribution.

For the bunch exiting the linac of the second design iteration, $\sim$76% of the beam is contained within 3 ps, despite the longitudinal *rms* parameter for the bunch being less than 1.5 ps. Consequently, the bunch does not need to be compressed and exits the linac to move immediately to the final focusing section.

7.2.1 WITHOUT SOLENOID

As the bunch does not need to be matched with a compressor lattice, the initial approach to the final focusing was to pass the bunch through a lattice of three quadrupoles. The value of β_x and β_y are shown as a function of the beam path s in Fig. 53. Certain aspects of the focusing lattice and the properties of the bunch at the IP are shown in Table 29, with the beam spot and phase spaces shown in Fig. 54. While the transverse emittance is still larger than desired, one other aspect becomes clear - the vertical size of the bunch becomes significantly large in the lattice. For a more suitable focusing lattice, the desire was to limit the transverse size of the beam.

7.2.2 WITH SOLENOID

Taking inspiration from the solenoid placed between the linac and the bunch compressor in the first design iteration, a solenoid was placed between the linac and the final focusing for this design. The change in α_x, α_y of the bunch after passing through the solenoid in the previous design made the introduction of a solenoid a feasible solution. Optimizing the lattice with the additional element demonstrated that the solenoid allowed for the reduction of the maximum transverse beam size while focusing the bunch down to a small size at the

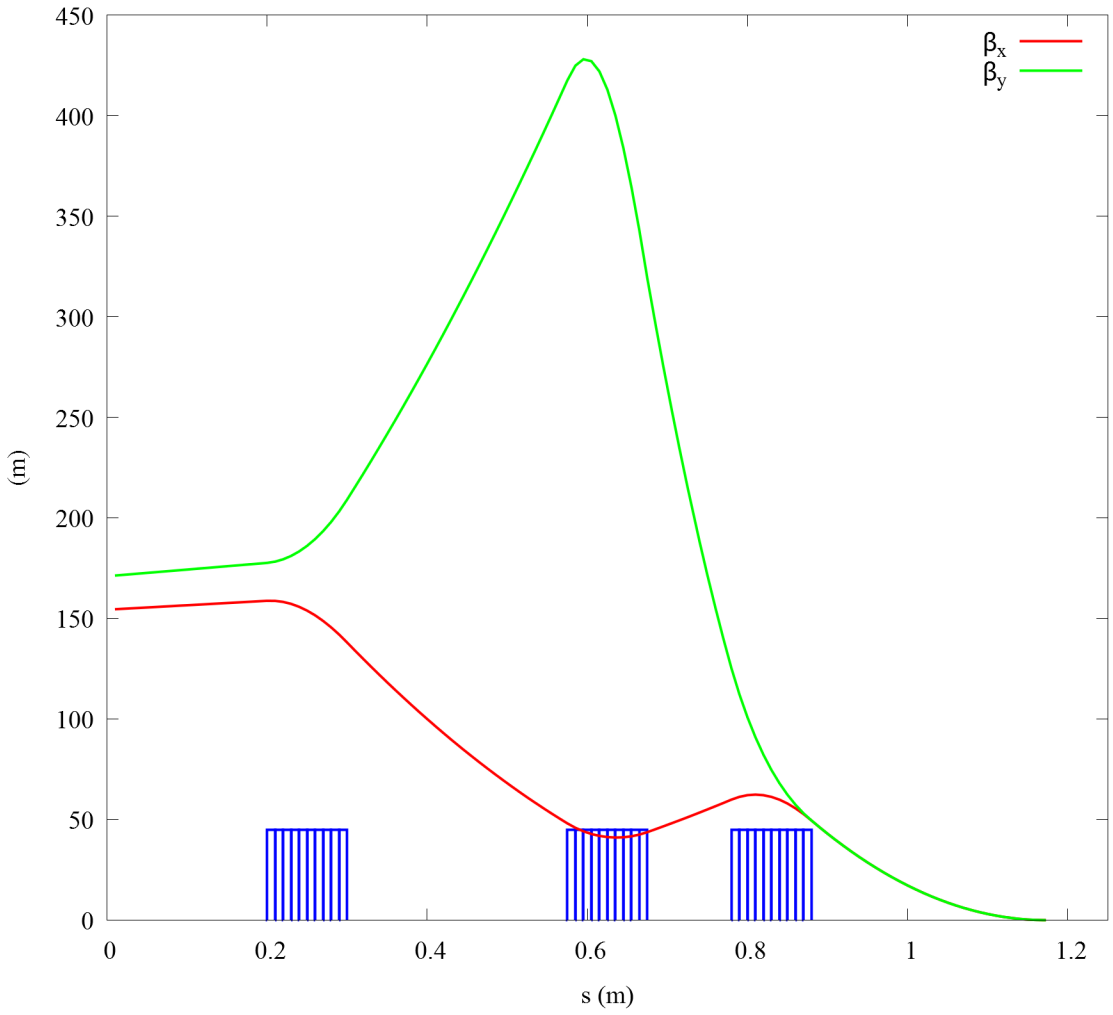

FIG. 53: β_x and β_y as a function of s in the final focusing section for the second iteration. The location of the three quadrupoles are positioned along the x-axis.

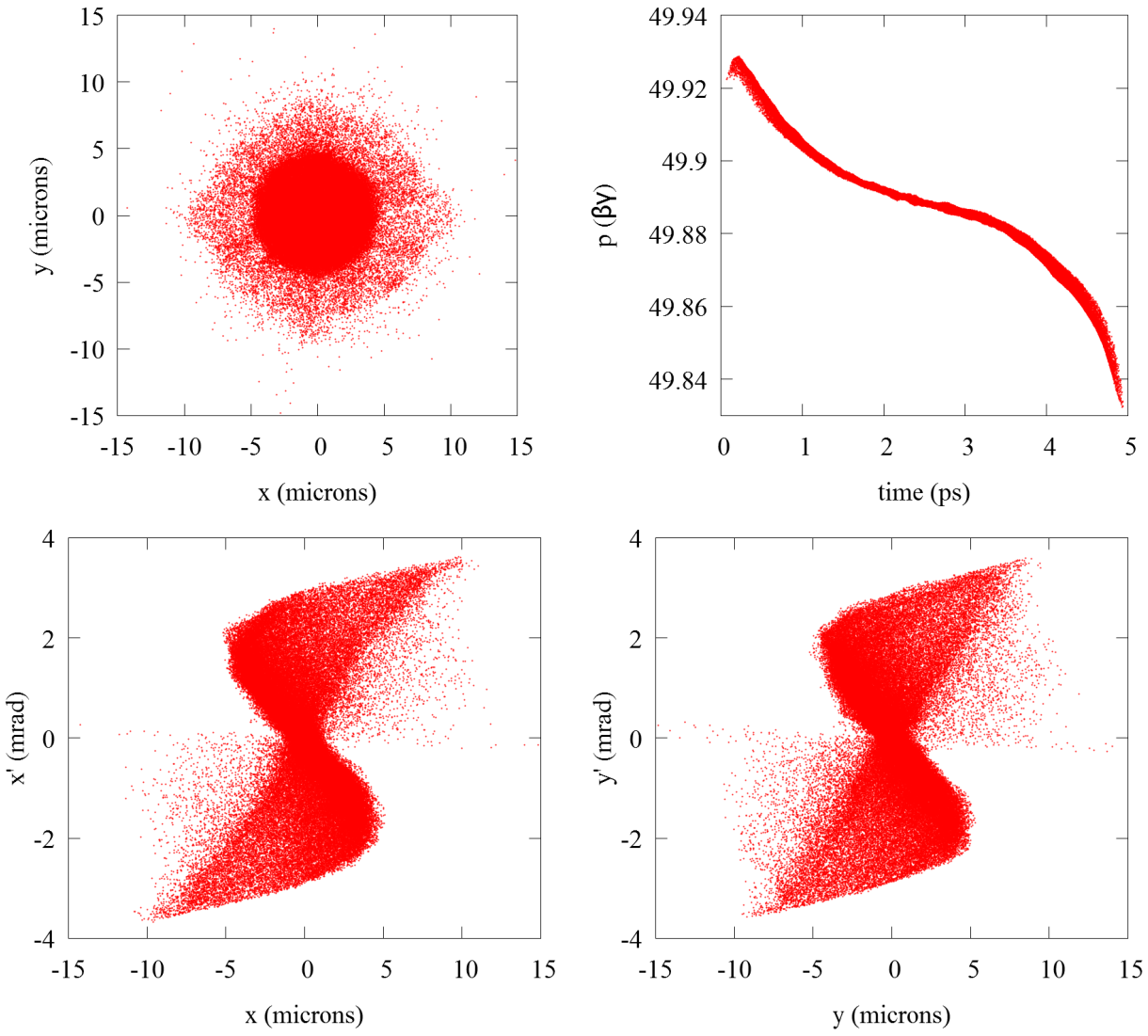

FIG. 54: The beam spot (top left), longitudinal phase space (top right), horizontal phase space (bottom left), and vertical phase space (bottom right) of the electron bunch at the IP for the second iteration without a solenoid in the final focusing section.

TABLE 29: Selected magnet properties of the final focusing section (top) and electron beam parameters (bottom) of the second version without a solenoid at the IP.

Parameter	Quantity	Units
Maximum β	428	m
Quadrupole length	0.1	m
Quadrupole strengths	1.2 - 3.7	T/m
β_x	1.7	mm
β_y	1.7	mm
$\epsilon^N_{x,rms}$	0.19	mm-mrad
$\epsilon^N_{y,rms}$	0.17	mm-mrad
σ_x	2.5	μm
σ_y	2.5	μm
$> 76\%$ longitude distribution	3	ps
rms energy spread	7.25	keV

IP. This can be seen in Fig. 55, which shows β_x and β_y as a function of the beam path s. The properties of the bunch at the IP are given in Table 30, with the beam spot and phase spaces displayed in Fig. 56.

Using the parameter values given in Table 30, the incident laser parameters given in Table 4, and the formulae presented in Section 2.5, it is possible to calculate the generated X-ray beam. The parameters of the anticipated X-ray beam are given in Table 31. While the flux is nearly equivalent to the original desired value, the average brilliance is less than a third of the original goal. Though the *rms* energy spread does meet the requirements, the transverse emittance has not improved significantly over the bunch which exited the linac of the first iteration. Consequently, it was decided to begin the final design version with a longer bunch length, in order to improve the transverse emittance, the parameter most in need of improvement in order to achieve the best possible X-ray source.

7.3 FINAL DESIGN

For the bunch which exits the linac of the final design, $\sim$80% of the beam is contained within 3 ps. Consequently, the bunch is sufficiently comparable to the longitudinal distribution requirements to satisfy the original target parameters and does not need to be compressed. In the design, the final focusing section consists of three quadrupoles, with a distance of $\sim$29 cm between the third quadrupole and the IP. The value of β_x and β_y are

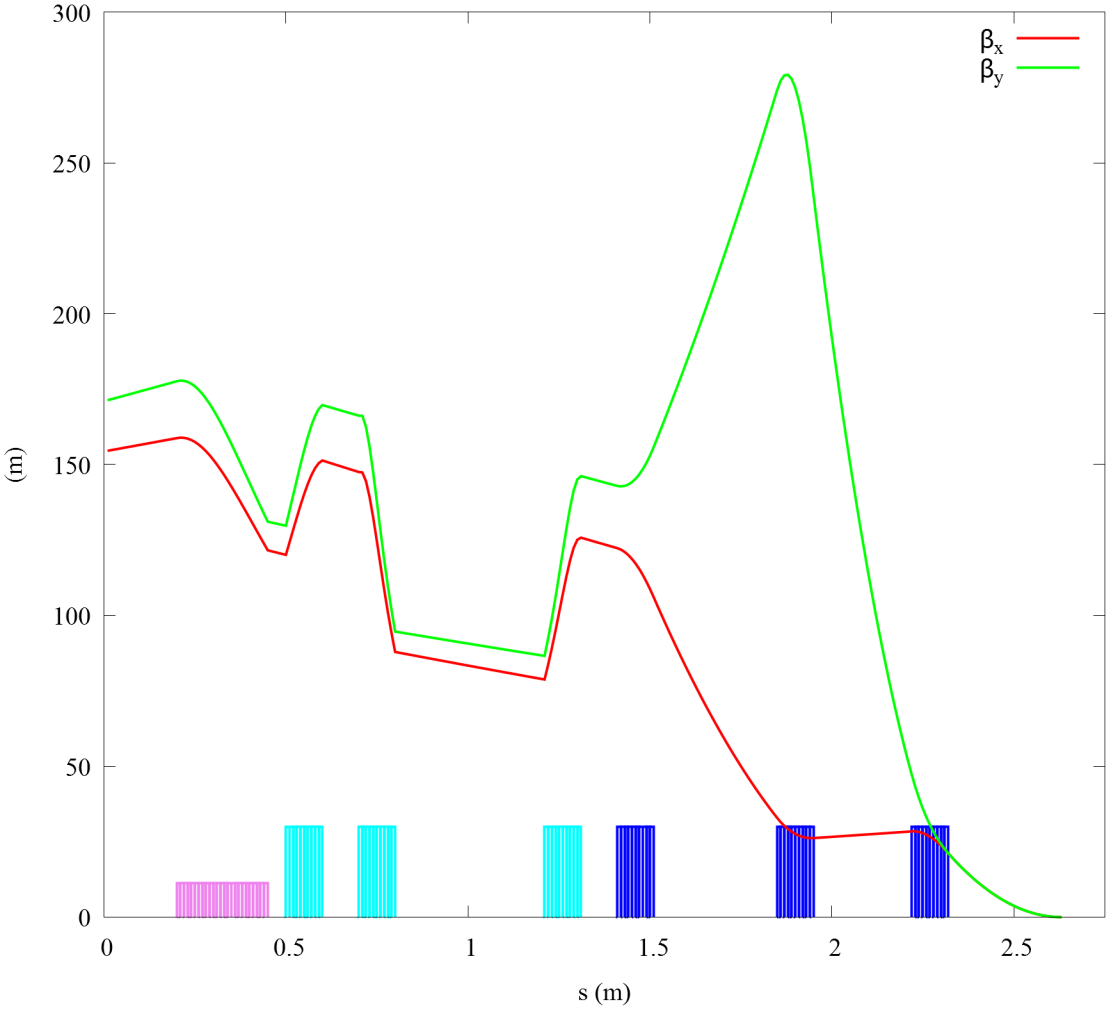

FIG. 55: β_x and β_y as a function of s in the final focusing section for the second iteration. The location of the solenoid, three skew quadrupoles, and three quadrupoles are positioned along the x-axis.

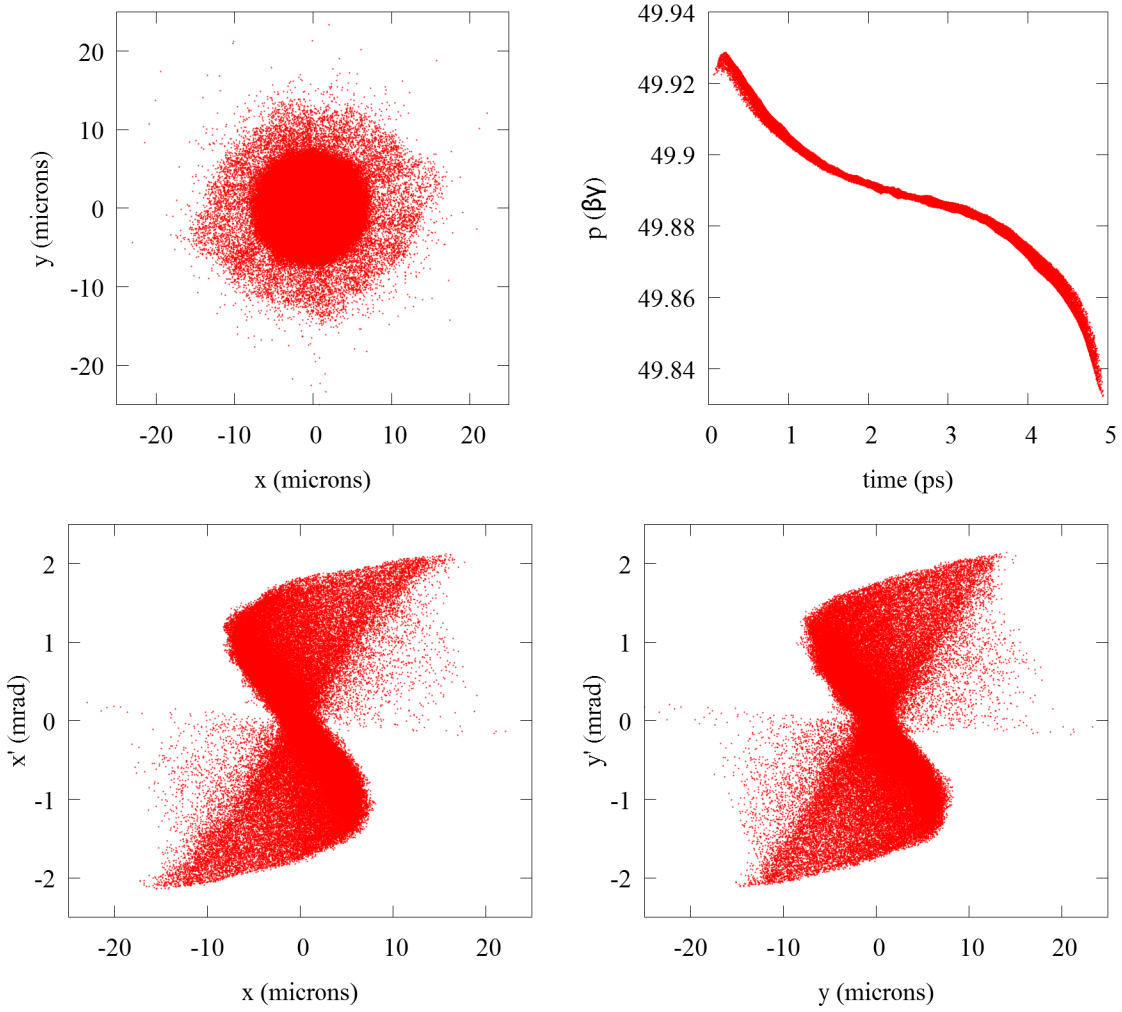

FIG. 56: The beam spot (top left), longitudinal phase space (top right), horizontal phase space (bottom left), and vertical phase space (bottom right) of the electron bunch at the IP for the second iteration with a solenoid in the final focusing section.

TABLE 30: Selected magnet properties of the final focusing section (top) and electron beam parameters (bottom) of the second version including a solenoid at the IP.

Parameter	Quantity	Units
Maximum β	280	m
Quadrupole length	0.1	m
Quadrupole strengths	.0039 - 2.5	T/m
β_x	4.6	mm
β_y	4.6	mm
$\epsilon^N_{x,rms}$	0.18	mm-mrad
$\epsilon^N_{y,rms}$	0.17	mm-mrad
σ_x	4	μm
σ_y	4	μm
$> 76\%$ longitudinal distribution	3	ps
rms energy spread	7.25	keV

TABLE 31: Estimated X-ray performance assuming second version of electron beam with solenoid attained at IP.

Parameter	Quantity	Units
X-ray energy	12	keV
N_γ	1.3×10^6	photons/bunch
Flux	1.3×10^{14}	ph/s
Average Brilliance	3.7×10^{14}	ph/(s-mm^2-mrad^2-0.1%BW)

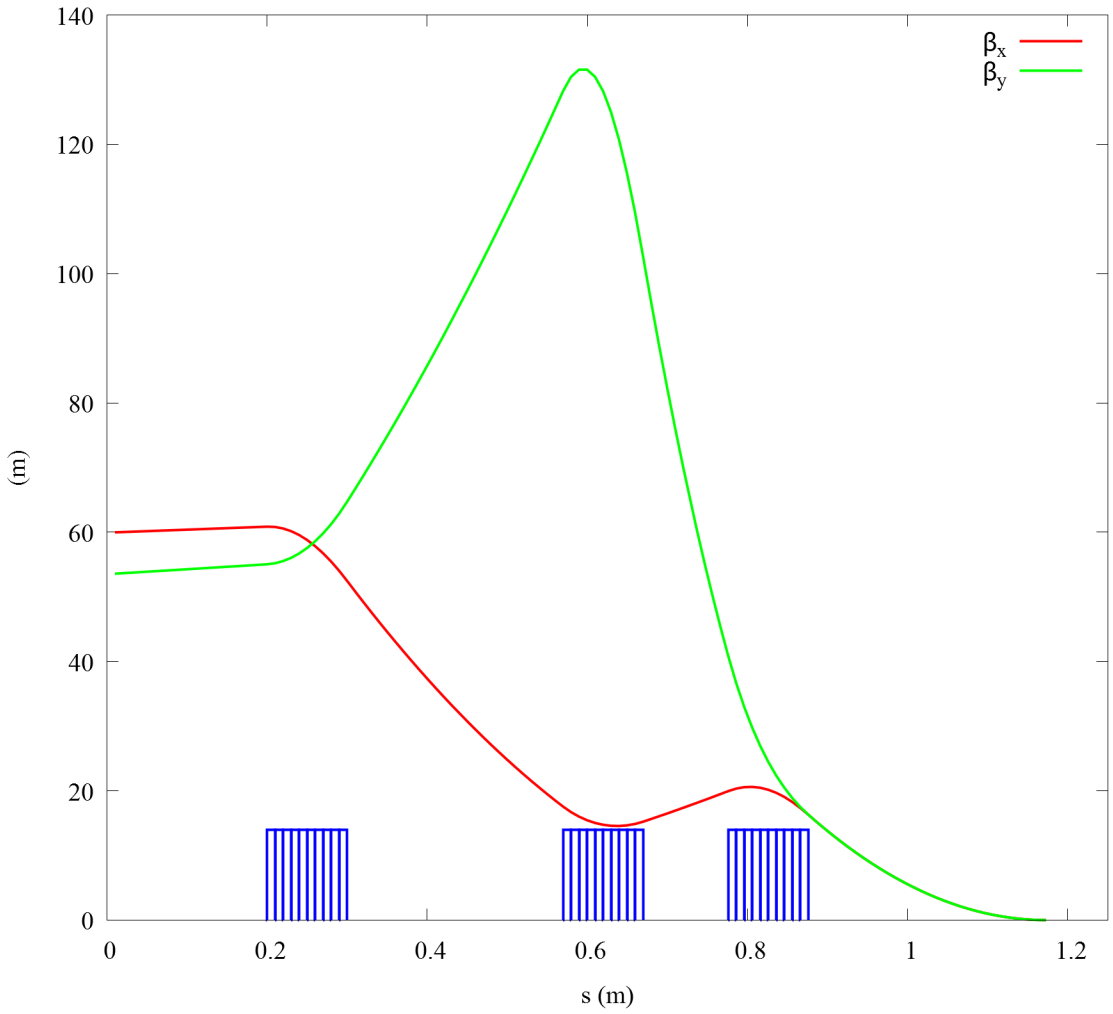

FIG. 57: β_x and β_y as a function of s in the final focusing section of the final design. The location of the three quadrupoles are positioned along the x-axis.

shown as a function of the beam path s in Fig. 57. Certain aspects of the focusing lattice and the properties of the bunch at the IP are shown in Table 32. From these values, it follows that this design iteration has produced an electron bunch much closer to the original goal given in Table 3. The beam spot and phase spaces of this beam are shown in Fig. 58, and are significantly better than in previous iterations.

Taking the simulated beam parameters given in Table 32 and the desired laser given in Table 4, it is possible to calculate properties of the resulting X-ray beam using the formulae presented in Section 2.5. The properties of the generated X-ray beam are given in Table 33. These results are compared with other compact Compton light sources which have been

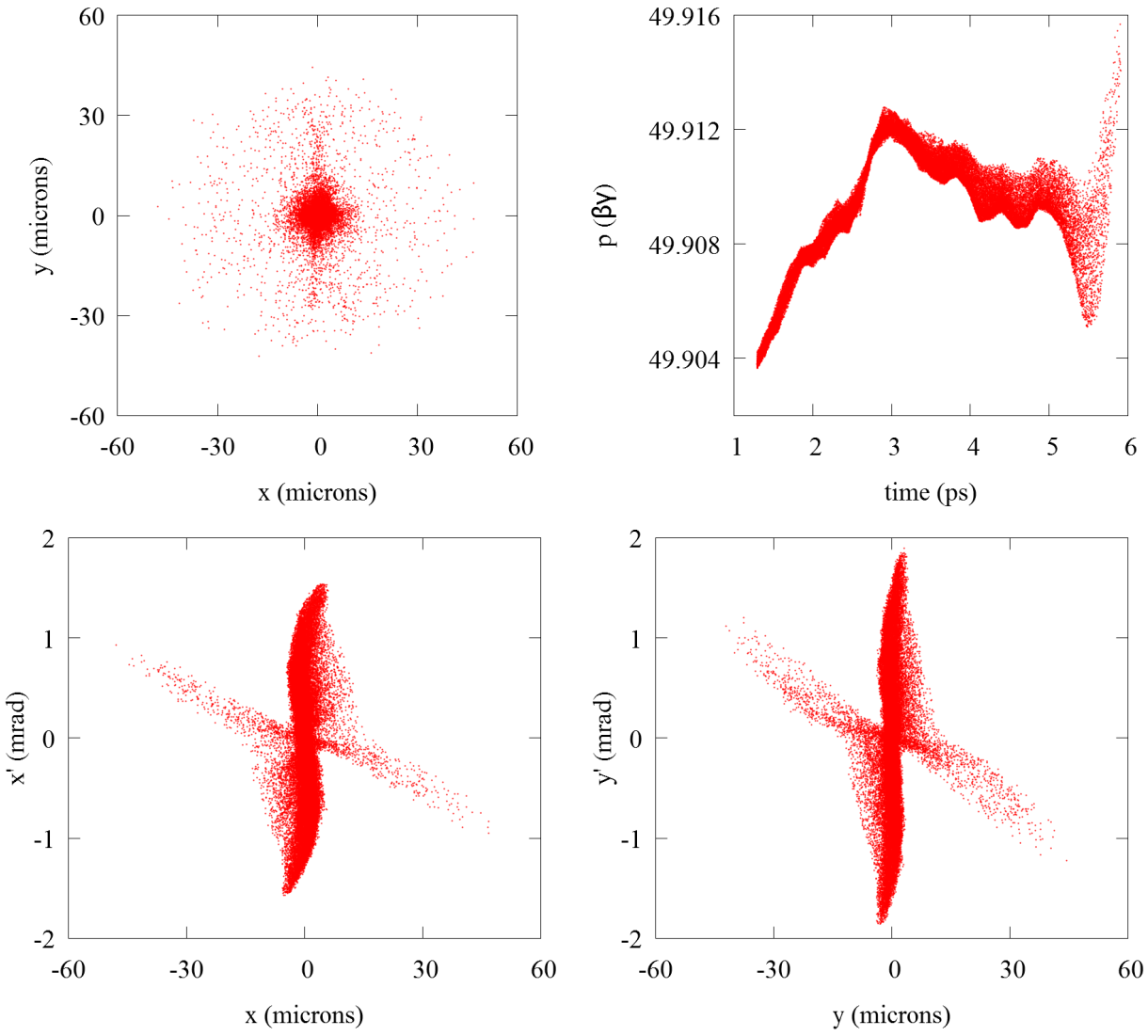

FIG. 58: The beam spot (top left), longitudinal phase space (top right), horizontal phase space (bottom left), and vertical phase space (bottom right) of the electron bunch at the IP for the final design.

TABLE 32: Selected magnet properties of the final focusing section (top) and electron beam parameters (bottom) of the final design at the IP.

Parameter	Quantity	Units
Maximum β	132	m
Quadrupole length	0.1	m
Quadrupole strengths	1.3 - 3.6	T/m
β_x	5.4	mm
β_y	5.4	mm
$\epsilon^N_{x,rms}$	0.1	mm-mrad
$\epsilon^N_{y,rms}$	0.13	mm-mrad
σ_x	3.4	μm
σ_y	3.8	μm
$> 76\%$ longitudinal distribution	3	ps
rms energy spread	3.4	keV

TABLE 33: Estimated X-ray performance assuming final design electron beam attained at IP.

Parameter	Quantity	Units
X-ray energy	12	keV
N_γ	1.4×10^6	photons/bunch
Flux	1.4×10^{14}	ph/s
Flux in 0.1% BW	2.1×10^{11}	ph/(s-0.1%BW)
Average Brilliance	1×10^{15}	ph/(s-mm^2-mrad^2-0.1%BW)

proposed in Table 34. It is immediately apparent that the flux of the design presented here is at least an order of magnitude greater than any other compact ICLS design. The average brilliance achieved by this design is greater by at least three orders of magnitude. Consequently, the compact ICLS presented by this dissertation is by far the most attractive prospect for potential users seeking a high average brilliance and narrow-bandwidth compact source.

TABLE 34: Selected X-ray properties of other compact ICLS designs, including X-ray energy, total flux, average brilliance in a 0.1% bandwidth, and spot size.

Project	Type	E_x (keV)	Ph/s	Ph/(s-mrad^2 -mm^2-0.1%BW)	σ_x (μm)
Lyncean [12, 17, 19]	SR	10-20	10^{11}	10^{11}	45
TTX [20]	SR	20-80	10^{12}	10^{10}	50
LEXG [21]	SR (SC)	33	10^{13}	10^{11}	20
ThomX [22]	SR	20-90	10^{13}	10^{11}	70
KEK QB [23]	Linac (SC)	35	10^{13}	10^{11}	10
KEK ERL [24]	Linac (SC)	67	10^{13}	10^{11}	30
NESTOR [25]	SR	30-500	10^{13}	10^{12}	70
MIT [1]	Linac	12	10^{13}	10^{12}	2
ODU	**Linac (SC)**	**$\leq$ 12**	**10^{14}**	**10^{15}**	**3**

CHAPTER 8

NUMERICAL SIMULATION OF SOURCE PERFORMANCE

For the calculation of the X-ray performance of the final design, the formulae presented in Section 2.5 were used to attain the values given in Table 33. When these formulae were initially presented, it was with the assumption that the electron beam distribution is Gaussian. The radial and longitudinal densities of the electron beam at the IP are shown in Fig. 59 and Fig. 60, respectively. It can easily be seen that the distribution in these directions are not Gaussian.

Consequently, it is appropriate to question the validity of using the aforementioned formulae to predict the performance of the final design as an X-ray source. Erik Johnson created a program which would numerically calculate the scattered radiation spectrum for a given electron beam distribution, such as a distribution generated by simulated particle tracking.

The energy density spectrum for an electron is given by

$$\frac{dU_1}{d\omega'} = \frac{\epsilon_0 c}{2\pi} \int_0^{2\pi} d\phi \int_{\cos\theta_a}^{1} |\tilde{E}(\omega(\omega'))|^2 \frac{d\sigma}{d\Omega} \left[\frac{\omega'}{\omega}\frac{d\omega}{d\omega'}\right] d\cos\theta, \tag{66}$$

where θ_a is the semi-angle of the aperture, $\tilde{E}$ is the Fourier time transform of the electric field of the incident laser pulse, ω' is the angular frequency of scattered radiation, ω is the angular frequency of the incident radiation, and $d\sigma/d\Omega$ is the differential cross-section of the electron. The equivalent number density of the spectrum is given by

$$\frac{dN_1}{d\omega'} = \frac{1}{\hbar\omega'}\frac{dU_1}{d\omega'}. \tag{67}$$

For realistic incident laser profiles, Eq. (66) is required to be numerically integrated. For a representative subset of N_p macroparticles from an electron beam distribution, such as one generated by tracking code, where $\mathbf{p} = (p_x, p_y, p_z)$, the total energy and number density spectra per electron are respectively given by

$$\begin{aligned} \frac{dU}{d\omega'} &= \frac{1}{N_p}\sum_{i=1}^{N_p} \frac{dU_1}{d\omega'}(\mathbf{p}_i) \\ \frac{dN}{d\omega'} &= \frac{1}{N_p}\sum_{i=1}^{N_p} \frac{dN_1}{d\omega'}(\mathbf{p}_i). \end{aligned} \tag{68}$$

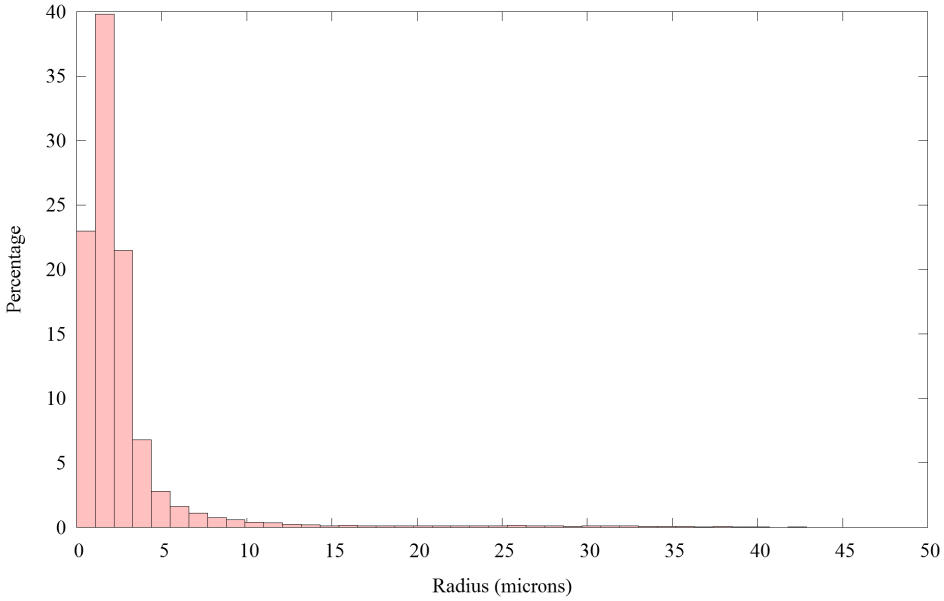

FIG. 59: Histogram of the radial distribution of the electron beam produced by the final design at the IP.

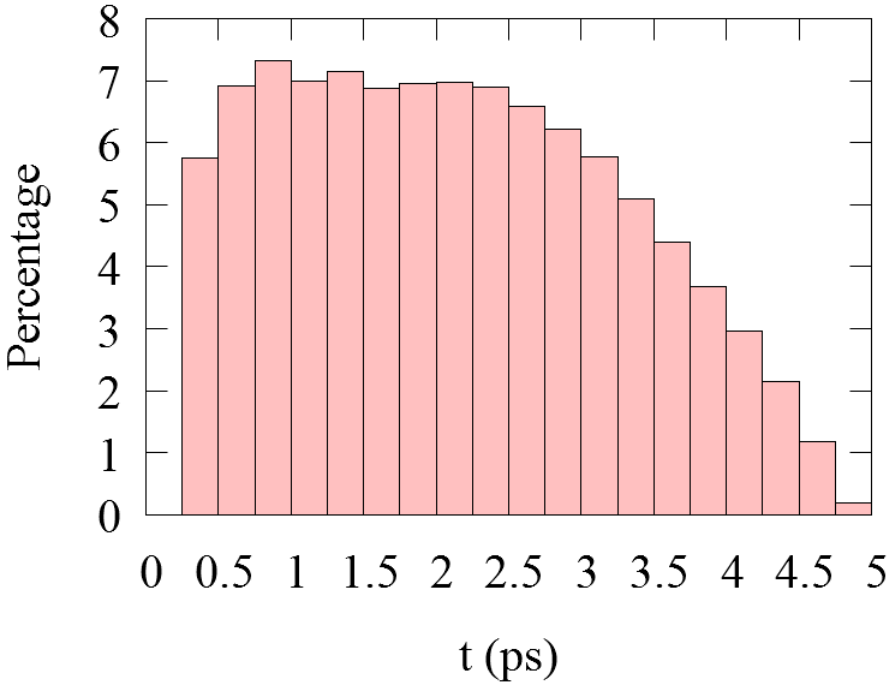

FIG. 60: Histogram of the longitudinal distribution of the electron beam produced by the final design at the IP.

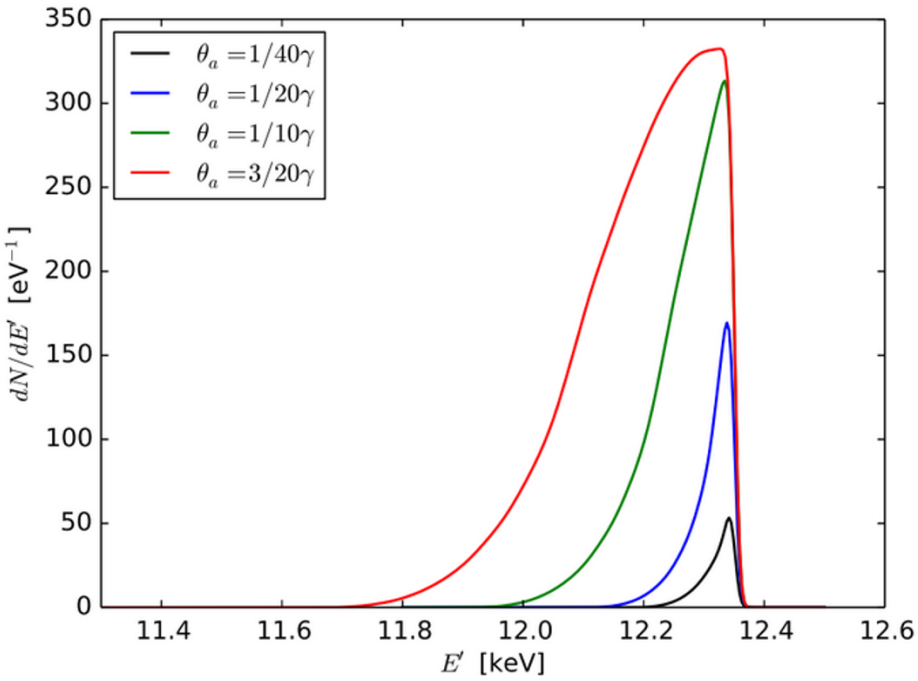

FIG. 61: Number spectra for different apertures generated using 4,000 particles (1/40γ, 1/20γ, 3/20γ) or 48,756 particles (1/10γ).

In essence, this program calculates the spectrum of scattered radiation for individual macroparticles, and the total spectrum is the result of summing over all spectra for the macroparticles. The accuracy of the results produced by this calculation from a sample size of N_p macroparticles is proportional to $1/\sqrt{N_p}$.

For the distribution of the electron beam at IP in the final version, results converged when using 4,000 particles for the calculation. The spectra results are shown in Fig. 61, which shows the number density of the scattered X-rays as a function of X-ray energy. Selected properties of the X-ray beam after being passed through a 1/40γ aperture are given in Table 35. The average brilliance is obtained from a pin-hole measurement

$$\mathcal{B} = \frac{\mathcal{F}_{0.1\%}}{2\pi^2 \sigma_x \sigma_y \theta_a^2} \tag{69}$$

where $\mathcal{F}_{0.1\%}$ is the flux of photons in a 0.1% bandwidth through an aperture of θ_a, with σ_x and σ_y being the transverse sizes of the electron beam at the IP [40].

By comparing the values in Tables 33 and 35, it is easily concluded that the difference in X-ray parameters due to the method of calculation is negligible to first order. While this may not be true for other electron beam distributions, in this case the formulae yield an

TABLE 35: X-ray performance of the final design attained by numerical simulation with an aperture of $1/40\gamma$.

Parameter	Quantity	Units
X-ray energy	12.3	keV
N_γ Number of photons in 0.1% BW	626.	ph/0.1%BW
$\mathcal{F}_{0.1\%}$ Flux in 0.1% BW	6.3×10^{10}	ph/(s-0.1%BW)
$\mathcal{B}$ Average Brilliance	9.4×10^{14}	ph/(s-mm^2-mrad^2-0.1%BW)

accurate estimations of the resulting X-ray parameters. Consequently, the final design of the source is exactly as outstanding as previously predicted [40].

CHAPTER 9

SENSITIVITY STUDIES

The sensitivity studies performed on the final version can be broken up into two different sections - the phase/amplitude of the SRF structures and the physical misalignment of all components in the design. The methodology used in each of these sections differs and will be detailed separately.

9.1 SRF CAVITY PHASE AND AMPLITUDE

For the gun and each of the four double-spoke cavities within the linac, the phase or amplitude was varied until the parameters of the electron beam at the IP had changed ∼20% from the values given in Table 32, which represent the ideal performance. While the phase or amplitude of one of the five SRF structures is varied, all other aspects are held constant to the values given by the ideal design. Table 36 gives the parameter being varied, the structure, the threshold at which the ∼20% change occurs, and which electron beam parameter has reached the threshold. As the amplitude of the SRF structures is normalized in different ways between simulation codes and physical control, the change in the amplitude is given as a percent of the original setting.

There are a few interesting observations which can be made about the results presented in Table 36. The threshold for both phase and amplitude is the same regardless of which cavity in the linac is being adjusted. However, these results do not mean that the electron beam at the IP is the same if the phase of the first and final cavity are altered.

More comprehensive results are shown in Tables 38 and 37, which correspond to the phase and amplitude errors, respectively. In both of these tables, the percentage change of the electron beam parameters are shown at the IP for the negative (-) and positive limits (+) given by Table 36. In these tables, values reported as "0" represent changes that fall below the threshold of 0.1%.

Some generalizations can be inferred from examining the two tables. For the phase errors of the cavities within the linac, while the limiting parameter is the energy spread, the next most altered parameter is typically the vertical size, σ_y. In regards to the transverse emittances, the values do not change more than 3% and typically less than that. Overall,

TABLE 36: The amplitude and phase perturbation from design for each SRF structure at which some electron beam parameter changes ∼20% at the IP.

Varied Parameter and Structure	Threshold	Changed Beam Parameter
Amplitude of Gun	-2.0%	*rms* energy spread
	+0.6%	*rms* energy spread
Amplitude of All Cavities	-1.0%	σ_y
	+0.8%	σ_y
Phase of Gun	-7.2°	*rms* energy spread
	+1.2°	*rms* energy spread
Phase of All Cavities	-1.2°	*rms* energy spread
	+1.2°	*rms* energy spread

the vertical emittance suffers more than the horizontal, and both emittance values typically differ more for perturbations in the gun or first two cavities, whether the perturbations are in the phase or amplitude. Given the difficulty in obtaining the extremely low emittance values in the design, it is somewhat surprising that emittance is not significantly impacted for either phase or amplitude. The energy of the beam only changes for amplitude perturbation in the cavities and in that case is limited to 0.2%. While the bunch length is more sensitive to perturbations in the gun or first cavity, this parameter changes more drastically due to amplitude perturbation. Indeed, aside from the beam parameter which is altered 20%, the change of the other parameters only rarely exceeds 5% (typically due to gun perturbations) and is generally much lower than that.

9.2 MISALIGNMENT

The parameters considered in this section are misalignment of different elements within the system - if the cavities or the magnets are displaced from their ideal positions while remaining parallel to the longitudinal axis (translational misalignment) or the translational misalignment of the quadrupoles in the final focusing. Instead of varying a single parameter while holding all others at their ideal setting, the sensitivity studies in this section take a different approach. For each of the situations, perturbations from the ideal are given to each aspect of position - i.e., for a single cavity, some perturbation is assigned to the x, y, and z directions. So for the situation of translational misalignment of the cavities comprising the linac, twelve perturbation values are needed. Each perturbation is a randomly generated

TABLE 37: Percent change of electron beam parameters at IP for limiting case of amplitude perturbation for SRF structures.

SRF Structure		$\epsilon^N_{x,\mathrm{rms}}$	σ_x	$\epsilon^N_{y,\mathrm{rms}}$	σ_y	σ_z	E_{kin}	ΔE_{kin}
Gun	-	0.2	0.9	2	2	15	0	20
	+	2	5	3	7	5	0	20
First Cavity	-	2	1	2	20	3	0.2	0.6
	+	1	5	2	20	2	0.2	0.1
Second Cavity	-	0.3	0.1	0.3	20	0.5	0.2	0
	+	0.2	2	0.2	20	0.4	0.2	0
Third Cavity	-	0	0.4	0	20	0.1	0.2	0.8
	+	0	2	0	20	0	0.2	0.6
Final Cavity	-	0	1	0	20	0	0.2	0.8
	+	0	2	0	20	0	0.2	0.6

TABLE 38: Percent change of electron beam parameters at IP for limiting case of phase perturbation for SRF structures.

SRF Structure		$\epsilon^N_{x,\mathrm{rms}}$	σ_x	$\epsilon^N_{y,\mathrm{rms}}$	σ_y	σ_z	E_{kin}	ΔE_{kin}
Gun	-	1	4	0.4	3	10	0	20
	+	0.8	2	2	3	5	0	20
First Cavity	-	0	0.7	0.6	1.4	0.5	0	20
	+	0	0.9	0.6	2	0.5	0	20
Second Cavity	-	0	0.2	0	0	0	0	20
	+	0	0.2	0.2	0.3	0	0	20
Third Cavity	-	0	0.2	0	0.4	0	0	20
	+	0	0.4	0.1	2	0	0	20
Final Cavity	-	0	0	0	0.3	0	0	20
	+	0	0.3	0.1	2	0	0	20

TABLE 39: The type and amount of error at which the specified electron beam parameter changes by ∼20%.

Type of Misalignment	Threshold	Changed Beam Parameter
Cavities, Translational	500 μm	*rms* energy spread
Magnets, Translational	300 μm	Vertical beam size, σ_y

TABLE 40: Percent change of electron beam parameters at IP for trials at limiting case of translational perturbation for cavities.

Trial	$\epsilon^N_{x,\mathrm{rms}}$	σ_x	$\epsilon^N_{y,\mathrm{rms}}$	σ_y	σ_z	E_{kin}	ΔE_{kin}
1	0	0	0	0.2	0	0	0
2	0.2	0.4	0.4	0.4	0.6	0	2
3	0.2	0.4	0.3	0.5	0.5	0	3
4	0.1	0.3	0.3	0.2	0.4	0	7
5	0	0	0.2	0	0.2	0	5
6	0.3	0.5	0.3	0.3	0.5	0	5
7	0	0.2	0	0.3	0.2	0	4
8	0	0	0.1	0	0	0	13
9	0	0	0	0	0	0	0.4
10	0.2	0.5	0.2	0.4	0.5	0	2
11	0	0	0	0.2	0	0	6
12	0	0.3	0	0.3	0.3	0	8

number between 0 and an upper limit. For each situation, the upper limit when the beam parameters at the IP differ by ∼20% than those given in Table 32 is the value which is being sought and reported. This approach requires fewer simulation runs while being more representative of how errors in a system are typically distributed.

The summary results of these studies are given in Table 39. It is more difficult to accurately identify the threshold perturbation amount in this approach - for a specific perturbation amount, 12 simulations are run. In the table, the maximum error is considered the defining quantity. This decision is made with the knowledge that this maximum is local, not global - meaning that for a different set of numbers generated to define simulations, an even larger maximum error may be possible.

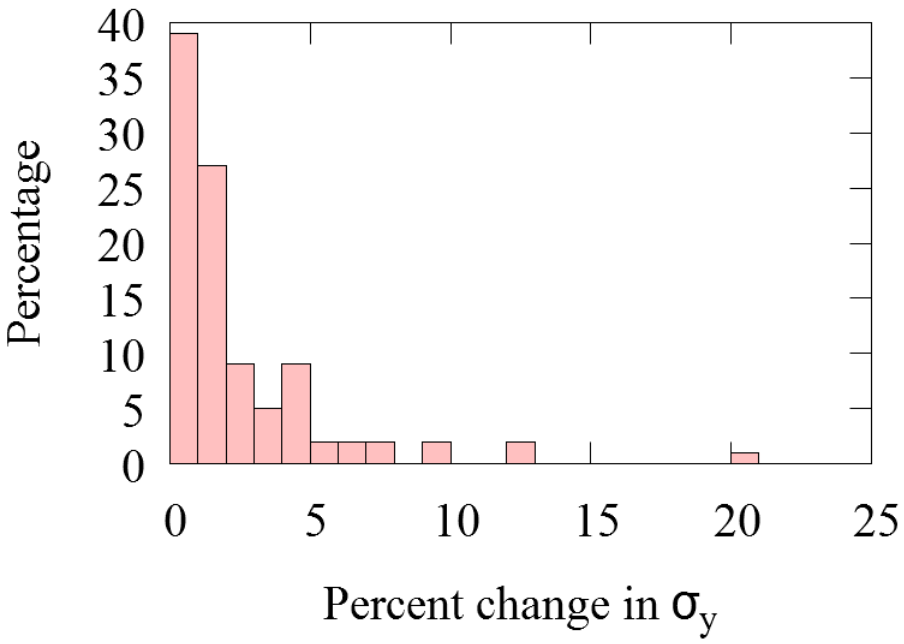

FIG. 62: Distribution of percent change of σ_y for 100 runs of translational misalignment of the magnets with a threshold of 300 μm.

The results from the set of trials for the 500 μm (0.5 mm) are given in Table 40. The limiting electron beam parameter is the *rms* energy spread, while all other electron beam parameters at the IP changed by less than 1%. The other electron beam parameters changed so minimally as to be insignificant to the overall light source performance. In fact, it is only when the perturbation threshold is set to 5 mm that another electron beam parameter becomes a limiting factor. At that point, the vertical size of the electron beam at the IP ranges from 0.6% to 17%, though the *rms* energy spread suffers exceedingly.

As the magnets do not affect the energy spread, taken with the fact that the largest beam size is in the vertical direction throughout the final focusing lattice, it follows that the limiting factor for translational perturbations of the magnets is the vertical size of the electron beam at the IP. For 100 runs, the resulting distribution of the percent change in σ_y of the electron beam at the IP is shown in Fig. 62. While the maximum change is $\sim$20%, the majority of the percent change is significantly smaller. There is no appreciable change in any other electron beam parameter at the IP except for the horizontal size, which does not change more than 1% for any run.

CHAPTER 10

FINAL DESIGN

This chapter presents all components of the final design, as a summary. All components are shown in Fig. 63, which does not include the necessary components to provide cooling, power, or the drive laser. The parameters of the electron bunch off the cathode are given in Table 41. The geometry parameters are given in Table 42. The values in this table, when used as input for the appropriate function in Appendix B, will produce the gun geometry as defined in Superfish.

The geometry of the double-spoke cavities which make up the linac has not varied, though the orientation and position has. In Table 43, the position, energy gain of the electron beam, and phases of each component. The position of each component is distance of the center of the structure from the surface of the cathode in the gun. First spoke orientation refers to the direction of the spoke closest to the cathode in a given cavity. RF phase is defined so that an RF phase of 0° corresponds to the maximum energy gain possible.

The details of the optics section are given in Table 44. Position and magnet strength are listed for each of the three quadrupoles. Position refers to the distance of the closest surface of the magnet measured from the surface of the cathode holder. The position of the interaction point is also given in the table. The stand off distance is the separation between the closest surface of the last quadrupole and the interaction point. Each quadrupole magnet has a length of 10 cm.

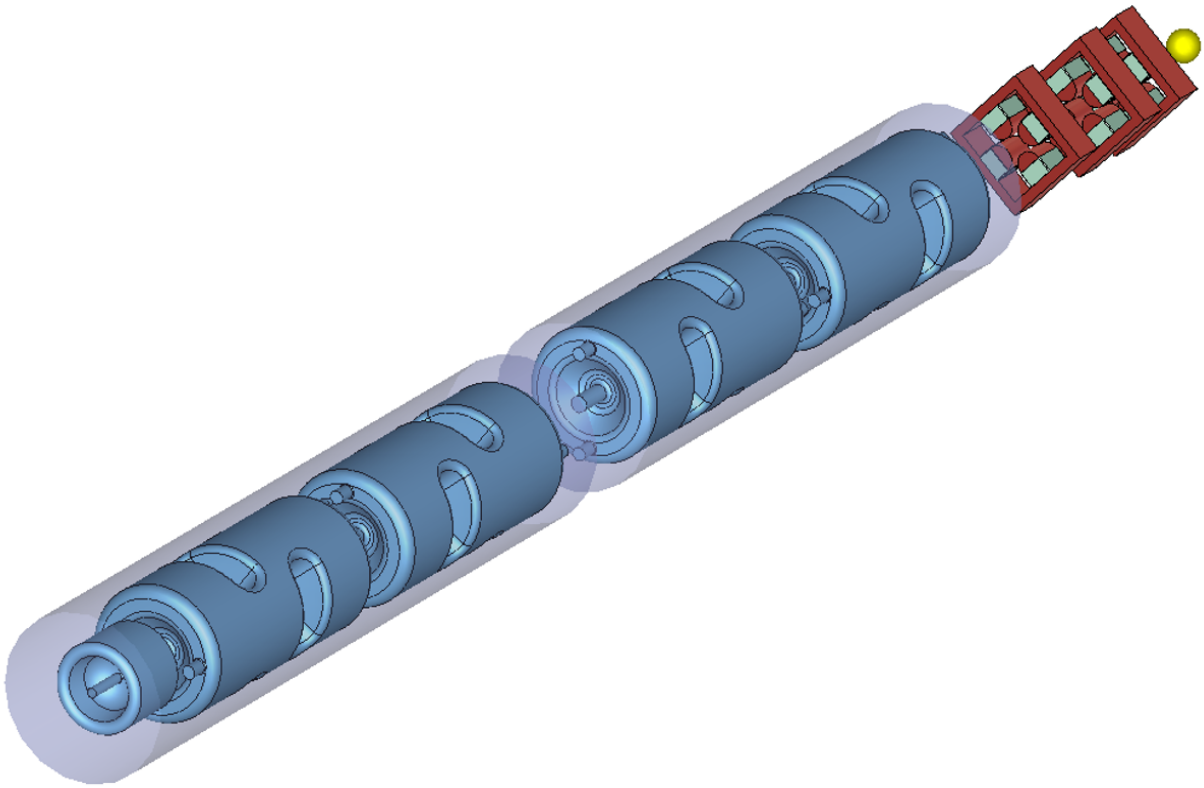

FIG. 63: A schematic of the entire final design. The first cryomodule containes the gun and two double-spoke cavities, the second contains the last two double-spoke cavities. Three quadrupole magnets (red) follow the linac, before the interaction point (yellow).

TABLE 41: Final iteration bunch distribution off the cathode.

Parameter	Quantity	Units
Longitudinal distribution	Plateau	
Bunch length	4.5	ps
Rise time	1.125	ps
Radial distribution	Uniform	
rms bunch radius	1	mm
Initial transverse momentum	0	mrad
Bunch charge	10	pC
Initial kinetic energy	1	keV
p_z distribution	Isotropic	

TABLE 42: List of geometry parameters with descriptions and values for the final iteration of the gun geometry.

Parameter	Description	Value	Units
R_{cav}	Radius of gun	134.24	mm
R_{cathode}	Radius of cathode holder tip	4.	mm
R_{pipe}	Radius of exiting beam pipe	10.	mm
R_{entrance}	Radius of entrance in nosecone	6.	mm
x_E	Distance of cathode recession	4.	mm
y_E	y-position of location on nosecone with vertical surface tangent	10.	mm
α	Angle of nosecone	13	$^\circ$
l_{fin}	Horizontal distance between fin tip and cathode tip	127.95	mm
h_{fin}	Maximum width of fin	52.734	mm
l_{gap}	Horizontal distance between x_E and x-position of y_{E2}	60.	mm
l_{rec}	Horizontal distance between two locations on exit face with vertical surface tangent	30.	mm
y_{E2}	y-position of location nearest beam pipe with vertical surface tangent	15.	mm

TABLE 43:

Structure	Position (m)	First Spoke Orientation	Beam Energy Gain (MeV)	Phase (°)	RF Phase (°)
SRF Gun	0	-	1.51	147.583	0
First Cavity	0.6195	Vertical	5.8725	325.95	0
Second Cavity	1.6835	Horizontal	5.8725	225.305	0
Third Cavity	3.0275	Horizontal	5.8725	133.724	-3.5
Fourth Cavity	4.0915	Vertical	5.8725	34.654	-3.5

TABLE 44:

Structure	Position (m)	Stregnth (T/m)
First Quad	5.0	1.267
Second Quad	5.3695	-3.533
Third Quad	5.5758	3.558
Interaction Point	5.9729	-
Stand off distance	0.297	-

CHAPTER 11

SUMMARY

The most fundamental elements of a Inverse Compton Light Source (ICLS) are an electron beam and a laser, which interact to produce X-rays or gamma-rays. At large scale facilities, such an electron beam is produced by large accelerators, such as 3rd generation synchrotrons. However, an alternative is to use a signficantly smaller accelerator to generate the electron beam, which is the case for Compact Inverse Compton Light Sources.

There are three main properties of an X-ray beam which are used to evaluate its quality - energy, flux, and average brilliance. At present, there is a massive difference between the flux and brilliance of an X-ray beam produced by bremsstrahlung using a typical lab-scale source and the flux and brilliance of a beam produced at a large facility by synchrotron radiation from an undulator. Compact Inverse Compton Light Sources are intended to bridge that divide, significantly improving upon bremsstrahlung sources while remaining more available in cost and ease of access than large facility sources. While they are significantly better than typical small-scale sources, current compact source designs leave much room for improvement in generating X-ray beams.

The Compact ICLS design presented improves on all other compact sources to date, expected to produce an X-ray beam of quality which is closer than ever to being comparable to beams produced at large-scale facilities. This is made possible by using cw superconducting rf to accelerate the beam before it is focused to the interaction point. At the interaction point, the electron beam has a small spot size and small transverse normalized *rms* emittance, which correspondingly result in an X-ray beam with high flux and brilliance. The ultra-low emittance is made feasible by a low bunch charge, with a high repetition rate so the X-ray flux is not adversely affected.

The most critical property in the electron beam at the interaction point is the transverse emittance. Because of this, in the first iteration of the design a long bunch length was used in order to mitigate emittance growth due to space charge. However, the long bunch results in a higher *rms* energy spread, to the point that the X-ray brilliance suffers. The long bunch length necessitates a compressor, during which the transverse emittance increases. This emittance increase is exacerbated by the high *rms* energy spread. At the interaction point,

the first iteration had neither a small spot size nor small transverse emittance, resulting in an estimated X-ray beam with properties far worse than the desired values.

The second iteration design involves a significantly shorter bunch duration off the cathode. In order to achieve a small transverse emittance, the bunch off the cathode had a spot size twice as large as in the prior iteration and the gun design was altered to more capably mitigate emittance growth due to space charge. Despite the significantly shorter bunch length off the cathode, the last two cavities required chirped operation in order to satisfy the *rms* energy spread requirement. The unanticipated difficulty with a extremely short bunch is that longitudinal space charge becomes a contributing factor in the bunch behavior. Additionally, the transverse emittance was still 60% higher than desired. Given that the bunch length exiting the linac was shorter than necessary to meet the longitudinal spatial distribution requirements at the IP, the bunch length was increased for the next version. The increase of bunch length allowed for a smaller transverse emittance, as the transverse space charge field decreases in strength.

The final design achieves an electron bunch which generates an X-ray beam unmatched in quality by other Compact ICLS designs. These desired electron beam parameters are achieved by utilizing a number of different techniques. The most effective technique was the emittance compensation by RF focusing. By altering the geometry of the gun to provide the correct RF focusing for a given bunch, it is possible to produce bunches with low normalized transverse *rms* emittances. Taken together with the low bunch charge, the achieved transverse emittances are sufficiently small. Choosing the correct bunch length off the cathode is necessary, in order to produce a bunch exiting the linac which does not need compression, but is still long enough that the transverse space charge effects can be compensated for by the RF focusing provided by the gun geometry. Another beneficial technique is taking advantage of the quadrupole-like behavior of the double-spoke cavities which comprise the linac in order to produce a fairly round beam at the exit of the linac. An approximately round beam at the exit to the linac allows for the bunch to be easily focused down to a small spot size on the order of a few microns.

By combining all of these techniques, it is possible to produce an electron beam which, when scattered off a suitable incident laser, generates an X-ray beam with a quality unmatched by any other Compact ICLS desgins. At present, the most common X-ray source to find in a small-scale facility is a bremsstrahlung source, which typically has a flux of at most $\sim 10^{13}$ ph/s and an average brilliance of $\sim 10^{9}$ ph/(s-mm^2-mrad^2-0.1%BW). Values of X-ray sources found at large-scale facilities, such as APS, have a similar flux but a much

higher average brilliance of $\sim 10^{19}$ ph/(s-mm^2-mrad^2-0.1%BW). Other compact designs do not offer improvement of beam flux and offer only a few orders of magnitude improvement for the average brilliance when compared to bremsstrahlung sources. The highest average brilliance such designs offer is $\sim 10^{12}$ ph/(s-mm^2-mrad^2-0.1%BW), which leaves significant room for improvement when compared to the average brilliance achievable at large-scale facilities. The source design that has been presented here has a flux at $\sim 10^{14}$ ph/s and an average brilliance of $\sim 10^{15}$ ph/(s-mm^2-mrad^2-0.1%BW). This average brilliance is a significant improvement on both bremsstrahlung and other compact sources, making the design presented here the best choice for a high average brilliance beam that can be found outside of large facilities.

Though the Compact ICLS presented here is capable of generating a world-class X-ray beam, some work remains to be done. Before this source can be built and tested, the appropriate incident laser needs to be constructed. A laser with a circulating power of 1 MW is called for in the design, but such a laser does not currently exist. Despite this, the consensus of those within that field is that such a laser is feasible, but until now there has not been a use for it. At present, high average power lasers currently constructed have a power of $\sim$100 kW, which is an order of magnitude lower than what is specified in this design. Using a laser with this circulating power would decrease the flux and brightness of the anticipated X-ray beam by an order of magnitude.

While the design presented is significantly better than other options, future work can lead to an even more impressive X-ray source. Some optimization was done on the gun geometry for a specific bunch off the cathode, but this work was not exhaustive. Alteration of the gun shape was focused around the cathode holder in the nosecone, to shape the radial component of the electric field at that location to mitigate emittance growth due to space charge. Another location within the gun with a significant radial component of the electric field is near the exit face of the gun. While this location has not been altered through the course of this work, it is possible that additional alteration may allow for an even smaller transverse emittance, leading to a higher average brilliance of the anticipated X-ray beam.

It is also possible that there exists a different initial bunch distribution which, when passed through a gun of appropriate shape, may result in a lower transverse emittance and consequently a higher average brilliance. Possible aspects of the initial bunch to change include the *rms* spot size and the distribution in both the longitudinal and radial directions. Increasing the initial *rms* length of the bunch off the cathode would necessitate the inclusion of some form of bunch compressor in order to meet the longitudinal distribution requirement

at the IP. However, increasing the initial bunch length may be called for to maintain the transverse emittance if the bunch charge is increased. Increasing the bunch charge would be one way to increase the flux of the X-ray beam, if the beam can still be focused down to a small spot size at the IP. The increase in flux would also lead to an increase in the brilliance, assuming the transverse emittance is the same as or better than what is presented here.

BIBLIOGRAPHY

[1] W. S. Graves *et al.*, Compact x-ray source based on burst-mode inverse Compton scattering at 100 kHz, Phys. Rev. ST Accel. Beams **17**, 120707 (2014).

[2] M.-E. Couprie and J.-M. Filhol, X radiation sources based on accelerators, Comptes Rendus Physique **9**, 487 (2008).

[3] M. Kihara, Development of Synchrotron Radiation Storage Rings, J. Synchrotron Rad. **5**, 179 (1998).

[4] R. Hettel, History of Synchrotron Radiation Sources, in *USPAS 2003 at Santa Barbara, California, USA: Beam Stability at Synchrotron Light Sources*, available at `http://www.aps.anl.gov/asd/diagnostics/uspas03/SR_history.pdf`.

[5] S. Benson *et al.*, The 4th generation light source at Jefferson Lab, Nucl. Instrum. Methods Phys. Res., Sect. A **582**, 14 (2007).

[6] G. R. Neil *et al.*, The JLab high power ERL light source, Nucl. Instrum. Methods Phys. Res., Sect. A **557**, 9 (2006).

[7] J. Arthur, G. Materlik, R. Tatchyn, and H. Winick, The LCLS: A fourth generation light source using the SLAC linac, Rev. Sci. Instrum. **66**, 1987 (1995).

[8] H. Ohashi *et al.*, Performance of focusing mirror device in EUV beamline of SPring-8 Compact SASE Source (SCSS), Nucl. Instrum. Methods Phys. Res., Sect. A **649**, 163 (2011).

[9] L. Strüder *et al.*, Large-format, high-speed, X-ray pnCCDs combined with electron and ion imaging spectrometers in a multipurpose chamber for experiments at 4th generation light sources, Nucl. Instrum. Methods Phys. Res., Sect. A **614**, 483 (2010).

[10] *European XFEL - Milestones*, `http://www.xfel.eu/overview/milestones/`.

[11] S. Benson *et al.*, X-ray sources by energy recovered linacs and their needed R&D, Nucl. Instrum. Methods Phys. Res., Sect. A 637, 1 (2011).

[12] G. A. Krafft and G. Priebe, Compton Sources of Electromagnetic Radiation, Rev. Accel. Sci. Technol. **3**, 147 (2010).

[13] H. Wiedemann, *Particle Accelerator Physics* (Springer, 2007).

[14] M. Jacquet, High intensity compact Compton X-ray sources: Challenges and potential of applications, Nucl. Instrum. Methods Phys. Res., Sect. B **331**, 1 (2014).

[15] A. W. Chao, K. H. Mess, M. Tigner, and F. Zimmermann, *Handbook of Accelerator Physics and Engineering* (World Scientific, 2013).

[16] A. Arnold and J. Teichert, Overview on superconducting photoinjectors, Phys. Rev. ST Accel. Beams **14**, 024801 (2011).

[17] *Lyncean Technologies, Inc. - Synchrotron light and the Lyncean Compact Light Source*, `http://www.lynceantech.com/technology.html`.

[18] *Beamlines Directory | Advanced Photon Source*, `http://www.aps.anl.gov/Beamlines/Directory/`.

[19] M. Bech, O. Bunk, C. David, R. Ruth, J. Rifkin, R. Loewen, R. Feidenhans'l, and F. Pfeiffer, Hard X-ray phase-contrast imaging with the Compact Light Source based on inverse Compton X-rays, J. Synchrotron Rad. **16**, 43 (2009).

[20] P. Yu and W. Huang, Lattice design and beam dynamics in a compact X-ray source based on Compton scattering, Nucl. Instrum. Methods Phys. Res., Sect. A **592**, 1 (2008).

[21] E. G. Bessonov, M. V. Gorbunkov, P. V. Kostryukov, Yu. Ya. Maslova, V. G. Tunkin, A. A. Postnov, A. A. Mikhailichenko, V. I. Shvedunov, B. S. Ishkhanov, and A. V. Vinogradov, Design study of compact Laser-Electron X-ray Generator for material and life sciences applications, J. Instrum. **4** P07017 (2009).

[22] A. Variola (ThomX Collaboration), The ThomX Project, in *Proceedings of the 2nd International Particle Acclerator Conference, San Sebastián, Spain* (IPAC'11/EPS-AG, 2011), p. 1903.

[23] J. Urakawa, Development of a compact X-ray source based on Compton scattering using a 1.3 GHz superconducting RF accelerating linac and a new laser storage cavity, Nucl. Instrum. Methods Phys. Res., Sect. A **637**, S47 (2011).

[24] R. Hajima, N. Kikuzawa, N. Nishimori, T. Hayakawa, T. Shizuma, K. Kawase, M. Kando, E. Minehara, H. Toyokawa, and H. Ohgaki, Detection of radioactive

isotopes by using laser Compton scattered γ-ray beams, Nucl. Instrum. Methods Phys. Res., Sect. A **608**, S57 (2009).

[25] E. Bulyak *et al.*, Compact X-ray source based on Compton backscattering, Nucl. Instrum. Methods Phys. Res., Sect. A **487**, 241 (2002).

[26] K. Deitrick, J. R. Delayen, B. R. P. Gamage, K. Hernández-Chahín, C. Hopper, G. Krafft, R. Olave, and T. Satogata, The ODU CAS Inverse Compton Source Design, `http://toddsatogata.net/Papers/2013-09-03-ComptonSource-2up.pdf`.

[27] W. S. Graves, W. Brown, F. X. Kaertner, and D. E. Moncton, MIT inverse Compton source concept, Nucl. Instrum. Methods Phys. Res., Sect. A **608**, S103 (2009).

[28] T. P. Wangler, *RF Linear Accelerators* (John Wiley and Sons, Inc., 2008).

[29] J. D. Jackson, *Classical Electrodynamics* (John Wiley and Sons, 1999).

[30] S. Belomestnykh and V. Shemelin, High-β Cavity Design - A Tutorial, in *Proceedings of the 12th International Workshop on RF Superconductivity, Cornell University, Ithaca, New York, USA* (2005), p. 2.

[31] T. Weiland, Eine Methode zur Lösung der Maxwellschen Gleichungen für sechskomponentige Felder auf diskreter Basis, Electronics and Communications (AEÜ) **31**, 116 (1977).

[32] T. Weiland, On the Unique Numerical Solution of Maxwellian Eigenvalue Problems in Three Dimensions, Particle Accelerators **17**, 227 (1985).

[33] *Poisson superfish*, `http://laacg1.lanl.gov/laacg/services/download\_sf.phtml`.

[34] *Computer simulation technology website*, `http://www.cst.com`.

[35] H. Padamsee, J. Knobloch, and T. Hays, *RF Superconductivity for Accelerators* (Wiley-VCH, 2008).

[36] J. Qiang, S. Lidia, R. D. Ryne, and C. Limborg-Deprey, Three-dimensional quasistatic model for high brightness beam dynamics simulation, Phys. Rev. ST Accel. Beams **9**, 044204 (2006).

[37] K. Floettmann, *ASTRA - A space charge tracking algorithm*, http://www.desy.de/~mpyflo.

[38] J. A. Clarke, *The Science and Technology of Undulators and Wigglers* (Oxford Series on Synchrotron Radiation, 2004).

[39] P. J. Duke, *Synchrotron Radiation: Production and Properties* (Oxford Science, 2000).

[40] G. A. Krafft, E. Johnson, K. Deitrick, B. Terzić, R. Kelmar, T. Hodges, W. Melnitchouk, and J. R. Delayen, Laser Pulsing in Linear Compton Scattering, Phys. Rev. Accel. Beams **19**, 121302 (2016).

[41] R. L. Burden and J. D. Faires, *Numerical Analysis* (Thomson Brooks/Cole, 2005).

[42] J. Qiang, *IMPACT-T User Document Beta Version 1.7*, http://amac.lbl.gov/~jiqiang/IMPACT-T/documents/ImpactTv1_7.pdf.

[43] *User's Manual for* elegant, http://aps.anl.gov/Accelerator_Systems_Division/Accelerator_Operations_Physics/manuals/elegant_latest/elegant.html.

[44] M. Borland, elegant: A Flexible SDDS-Compliant Code for Accelerator Simulation, Advanced Photon Source LS-287, September 2000.

[45] M. Borland, A Self-Describing File Protocol for Simulation Integration and Shared Post-Processors, in *Proceedings of the 1995 Particle Accelerator Conference, Dallas, Texas, USA* (IEEE, 1996).

[46] *User's Guide for SDDS Toolkit Version 2.8*, http://aps.anl.gov/Accelerator_Systems_Division/Accelerator_Operations_Physics/manuals/SDDStoolkit/SDDStoolkit.html.

[47] *The python programming language*, http://www.python.org.

[48] *The gnuplot graphing utility*, http://www.gnuplot.info.

[49] A. Michalke, Photocathodes Inside Superconducting Cavities: Studies on the Feasibility of a Superconducting Photoemission Source of High Brightness, Ph.D. thesis, Bergische Universität Gesamthochschule Wuppertal (1993).

[50] A. Michalke, H. Piel, C. K. Sinclair, P. Michelato, C. Pagani, L. Serafini, and M. Peiniger, Photocathodes Inside Superconducting Cavities: An experimental approach to a superconducting photoemission source of high brightness, in *Proceedings of the 5th Workshop on RF Superconductivity, DESY, Hamburg, Germany* (1991), p. 734.

[51] A. Michalke, H. Piel, C. K. Sinclair, P. Michelato, First Operation of High-Quantum Efficiency Photocathodes Inside Superconducting Cavities, in *Proceedings of the 3rd European Particle Accelerator Conference, Berlin, Germany* (1992), p. 1014.

[52] C. Pagani, P. Michelato, and L. Serafini, High brightness, long pulse, electron beam production with SC photo-injectors, Nucl. Instrum. Methods Phys. Res., Sect. A **340**, 17 (1994).

[53] D. Janssen *et al.*, First operation of a superconducting RF-gun, Nucl. Instrum. Methods Phys. Res., Sect. A **507**, 314 (2003).

[54] J. R. Harris *et al.*, Design and operation of a superconducting quarter-wave electron gun, Phys. Rev. ST Accel. Beams **14**, 053501 (2011).

[55] B. E. Carlsten, New Photoelectric Injector Design for the Los Alamos National Laboratory XUV FEL Accelerator, Nucl. Instrum. Methods Phys. Res., Sect. A **285**, 313 (1989).

[56] L. Serafini and J. B. Rosenzweig, Envelope analysis of intense relativistic quasilaminar beams in rf photoinjectors: A theory of emittance compensation, Phys. Rev. E **55**, 7565 (1997).

[57] V. Kumar, Understanding the focusing of charged particle beams in a solenoid magnetic field, Am. J. Phys. **77**, 737 (2009).

[58] D. Janssen and V. Volkov, RF focussing - an instrument for beam quality improvement in superconducting RF guns, Nucl. Instrum. Methods Phys. Res., Sect. A **452**, 34 (2000).

[59] C. E. Reece and G. Ciovati, Superconducting Radio-Frequency Technology R&D for Future Accelerator Applications, Rev. Accel. Sci. Technol. **5**, 285 (2012).

[60] A. Facco, Tutorial on Low Beta Cavity Design, in *Proceedings of the 12th International Workshop on RF Superconductivity, Cornell University, Ithaca, New York, USA* (2005), p. 21.

[61] S. Belomestnykh, Superconducting Radio-Frequency Systems for High-β Particle Accelerators, Rev. Accel. Sci. Technol. **5**, 147 (2012).

[62] C. Reece, SRF Challenges for Improving Operational Electron Linacs, in *Proceedings of SRF 2011, Chicago, Illinois, USA* (2011), MOIOA04 Presentation, `http://accelconf.web.cern.ch/AccelConf/SRF2011/talks/moioa04_talk.pdf`.

[63] R. Legg *et al.*, Status of the Wisconsin SRF Gun, in *Proceedings of the 2012 International Particle Accelerator Conference, New Orleans, Louisiana, USA* (IEEE, 2012), p. 661.

[64] S. A. Belomestnykh, Status of Superconducting RF Guns at BNL, in *Proceedings of the 50th ICFA Advanced Beam Dynamics Workshop on Energy Recovery Linacs* (2011), WG1001 Presentation, `http://accelconf.web.cern.ch/AccelConf/ERL2011/talks/wg1001_talk.pdf`.

[65] A. S. Hofler, Optimization Framework for a Radio Frequency Gun Based Injector, Ph.D. thesis, Old Dominion University, 2012.

[66] T. Satogata, K. Deitrick, J. Delayen, B. R. P. Gamage, K. Hernández-Chahín, C. Hopper, G. Krafft, and R. Olave, Compact Accelerator Design for a Compton Light Source, in *Proceedings of the 4th International Particle Accelerator Conference, Shanghai, China* (JACoW, 2013), p. 2292.

[67] M. Groover and E. Zimmers, *CAD/CAM: Computer-Aided Design and Manufacturing* (Prentice-Hall, 1983).

[68] I. V. Bazarov, B. M. Dunham, C. Gulliford, Y. Li X. Liu, C. K. Sinclair, K. Soong, and F. Hannon, Benchmarking of 3D space charge codes using direct phase space measurements from photoemission high voltage dc gun, Phys. Rev. ST Accel. Beams **11**, 100703 (2008).

[69] L. Groening *et al.*, Benchmarking of measurement and simulation of transverse rms-emittance growth, Phys. Rev. ST Accel. Beams **11**, 094201 (2008).

[70] R. D. Ryne, J. Qiang, A. Adelmann, J. Amundson, and P. Spentzouris, A Test Suite of Space-Charge Problems for Code Benchmarking, in *Proceedings of the 2004 European Particle Accelerator Conference, Lucerne, Switzerland* (2004), p. 1939.

[71] J. Qiang and R. D. Ryne, Benchmark of the IMPACT Code for High Intensity Beam Dynamics Simulation (2008), available at `http://escholarship.org/uc/item/10h5h1qx`.

[72] R. Akre *et al.*, Commissioning the Linac Coherent Light Source injector, Phys. Rev. ST Accel. Beams **11**, 030703 (2008).

[73] D. H. Dowell et al., *Proccedings of the 2007 Particle Accelerator Conference, Albuquerque, NM, USA* (IEEE, 2007), p. 1317.

[74] Y. Park, M. Kulishov, R. Slavík, and J. Azaña, Picosecond and sub-picosecond flat-top pulse generation using uniform long-period fiber gratings, Optics Express **14**, 12670 (2006).

[75] C. S. Hopper, R. G. Olave, and J. R. Delayen, Superconducting Single-Spoke Cavities for High-Velocity Applications, in *Proceedings of the 4th International Particle Accelerator Conference, Shanghai, China* (JACoW, 2013), p. 2480.

[76] C. S. Hopper, R. G. Olave, and J. R. Delayen, Development of Spoke Cavities for High-Velocity Applications, in *Proceedings of the 3rd International Particle Accelerator Conference, New Orleans, Louisiana, USA* (IEEE, 2012), p. 2456.

[77] C. S. Hopper and J. R. Delayen, Design of Superconducting Spoke Cavities for High-Velocity Applications, in *Proceedings of the 15th International Converence of RF Superconductivity, Chicago, Illinois, USA* (2011), p. 154.

[78] J. R. Delayen, Applications of Spoke Cavities, in *Proceedings of the 2010 Linac Conference, Tsukuba, Japan* (2010), p. 377.

[79] J. R. Delayen, S. U. DeSilva, and C. S. Hopper, Design of Superconducting Spoke Cavities for High-Velocity Applications, in *Proceedings of the 2011 Particle Accelerator Conference, New York, New York, USA* (PAC'11 OC/IEEE, 2011), p. 1024.

[80] C. S. Hopper, Development of Superconducting Spoke Cavities for High-Velocity Applications, Ph.D. thesis, Old Dominion University, 2015.

[81] C. S. Hopper and J. R. Delayen, Superconducting spoke cavities for high-velocity applications, Phys. Rev. ST Accel. Beams **16**, 102001 (2013).

[82] C. S. Hopper, K. Deitrick, and J. R. Delayen, Geometry Effects on Multipole Components and Beam Optics in High-Velocity Multi-Spoke Cavities, in *Proceedings of the 2013 North American Particle Accelerator Conference, Pasadena, California, USA* (2013), p. 868.

[83] B. R. P. Gamage and T. Satogata, Magnetic Bunch Compression for a Compact Inverse Compton Source, in *Proceedings of the 2013 North American Particle Accelerator Conference, Pasadena, California, USA* (2013), p. 1346.

[84] R. J. England, Longitudinal Shaping of Relativistic Bunches of Electrons Generated by an RF Photoinjector, Ph.D. thesis, University of Californai Los Angeles (2003).

[85] M. Borland (private communication).

[86] S. Y. Lee, *Accelerator Physics* (World Scientific Pub., 2004).

[87] M. Borland, A High-Brightness Thermionic Microwave Electron Gun, Ph.D. thesis, Stanford University (1991).

[88] H. A. Enge, Achromatic Magnetic Mirror for Ion Beams, Rev. Sci. Instrum. **34**, 385 (1963).

[89] H. Hama, F. Hinode, K. Kasamsook, M. Kawai, K. Nanbu, M. Yasuda, Space Charge Effect for Short Electron Bunches in an Alpha Magnet, in *Proceedings of the 30th International Free Electron Conference, Gyeongju, Korea* (2008), p. 305.

APPENDIX A

INPUT/OUTPUT FIELD FORMATS

Throughout this appendix, a grid is defined by specific points in a number of directions. Three-dimensional grids have points in the x, y, and z directions, while two-dimensional grids have points in the r and z directions. For any given direction a, the total number of grid points in that direction is represented by Na. Any grid point in direction a is represented by a_i, where i is an integer between 1 and Na. The grid points are ordered such that $a_i < a_{i+1}$ for all values of i between 1 and Na-1. An example of this is shown in Fig. 64 for a two-dimensional grid, with both the representative symbol and the actual value shown.

A.1 INPUT/OUTPUT FORMATS OF EM FIELDS

A.1.1 OUTPUT FORMAT OF EM FIELDS FROM CST MICROWAVE STUDIO

The output of the EM fields from CST Microwave Studio is separated into two files, one for the E field and one for the H field. These files are tab-separated text files, with user-defined names. The first line of each file labels each tab-separated column while indicating the units used in [ ], such as x [mm]. The second line is a line of "- - - -", simply a separator between the labels and the values. The field components in a given row are for the grid point given in the first three elements of that row. The interval between grid points is constant in a given direction and each direction interval is user-defined. The output formats of the E and H fields are given in Tables 45 and 46, respectively.

A.1.2 OUTPUT FORMAT OF EM FIELDS FROM SUPERFISH

EM field data from SF7, the Poisson Superfish Field Interpolator, can be output on a line, arc, or grid - though only the grid option is addressed here. Before running SF7, it is suggested to run SFO, the postprocessor, though this decision is left up to the user. The output is produced in the file "OUTSF7.TXT". The grid is defined by the user providing the following four values: Zmin, Rmin, Zmax, and Rmax, as well as the increments in each

TABLE 45: Electric field file output format from CST Microwave Studio.

x [mm]	y [mm]	z [mm]	ExRe [V/m]	EyRe [V/m]	EzRe [V/m]	ExIm [V/m]	EyIm [V/m]	EzIm [V/m]
x_1	y_1	z_1	E_x	E_y	E_z	0	0	0
x_2	y_1	z_1	E_x	E_y	E_z	0	0	0
.								
.								
.								
x_{Nx}	y_1	z_1	E_x	E_y	E_z	0	0	0
x_1	y_2	z_1	E_x	E_y	E_z	0	0	0
x_2	y_2	z_1	E_x	E_y	E_z	0	0	0
.								
.								
.								
x_{Nx}	y_2	z_1	E_x	E_y	E_z	0	0	0
.								
.								
.								
x_{Nx}	y_{Ny}	z_1	E_x	E_y	E_z	0	0	0
x_1	y_1	z_2	E_x	E_y	E_z	0	0	0
x_2	y_1	z_2	E_x	E_y	E_z	0	0	0
.								
.								
.								
x_{Nx}	y_{Ny}	z_2	E_x	E_y	E_z	0	0	0
.								
.								
.								
x_{Nx}	y_{Ny}	z_{Nz}	E_x	E_y	E_z	0	0	0

TABLE 46: Magnetic induction field file output format from CST Microwave Studio.

x [mm]	y [mm]	z [mm]	HxRe [A/m]	HyRe [A/m]	HzRe [A/m]	HxIm [A/m]	HyIm [A/m]	HzIm [A/m]
x_1	y_1	z_1	0	0	0	H_x	H_y	H_z
x_2	y_1	z_1	0	0	0	H_x	H_y	H_z
.								
.								
.								
x_{Nx}	y_1	z_1	0	0	0	H_x	H_y	H_z
x_1	y_2	z_1	0	0	0	H_x	H_y	H_z
x_2	y_2	z_1	0	0	0	H_x	H_y	H_z
.								
.								
.								
x_{Nx}	y_2	z_1	0	0	0	H_x	H_y	H_z
.								
.								
.								
x_{Nx}	y_{Ny}	z_1	0	0	0	H_x	H_y	H_z
x_1	y_1	z_2	0	0	0	H_x	H_y	H_z
x_2	y_1	z_2	0	0	0	H_x	H_y	H_z
.								
.								
.								
x_{Nx}	y_{Ny}	z_2	0	0	0	H_x	H_y	H_z
.								
.								
.								
x_{Nx}	y_{Ny}	z_{Nz}	0	0	0	H_x	H_y	H_z

TABLE 47: The output format from SF7 (Superfish) for EM field data, which is necessarily cylindrically symmetric.

Electromagnetic fields for a rectangular area with corners at:
(Zmin,Rmin) = (z_1,r_1)
(Zmax,Rmax) = (z_{Nz},r_{Nr})
Z and R increments: Nz − 1 Nr − 1

Z	R	Ez	Er	|E|	H
(cm)	(cm)	(MV/m)	(MV/m)	(MV/m)	(A/m)
z_1	r_1	E_z	E_r	$\|\mathbf{E}\|$	H_θ
z_2	r_1	E_z	E_r	$\|\mathbf{E}\|$	H_θ
.					
.					
.					
z_{Nz}	r_1	E_z	E_r	$\|\mathbf{E}\|$	H_θ
z_1	r_2	E_z	E_r	$\|\mathbf{E}\|$	H_θ
z_2	r_2	E_z	E_r	$\|\mathbf{E}\|$	H_θ
.					
.					
.					
z_{Nz}	r_2	E_z	E_r	$\|\mathbf{E}\|$	H_θ
.					
.					
.					
z_{Nz}	r_{Nr}	E_z	E_r	$\|\mathbf{E}\|$	H_θ

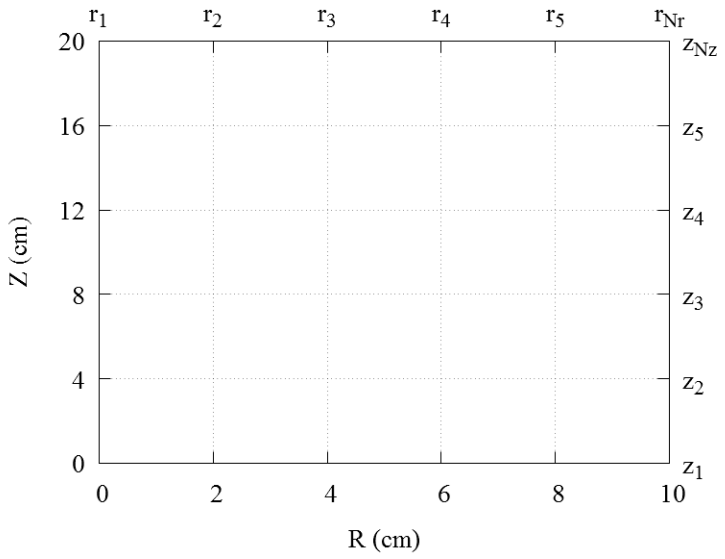

FIG. 64: Grid definition example.

direction. The format given in Table 47 starts at line 27 of the output file, preceeded by copyright information and with which solution file this output is associated.

A.1.3 INPUT FORMAT OF EM FIELDS FOR *ASTRA*

Six files are required to define a 3D field map. These files have a common name, which must have '3D' at the beginning or following three characters, such as "3D_Cavity" or "TM_3D". The six file extensions are .ex, .ey, .ez, .bx, .by, and .bz. The six field components (E_x, E_y, E_z, B_x, B_y, and B_z) are individually stored in the file with the matching extension. The grid positions are given in meters (m), the E field components in volts per meter (V/m), and the B field components in teslas (T). The format of these files is shown in Table 48, with $\mathcal{F}(x_i, y_j, z_k)$ representing the field component indicated in the file extension at the grid point (x_i, y_j, z_k).

A.1.4 INPUT FORMAT OF EM FIELDS FOR IMPACT-T

Two different input formats are given here - one for a 3D EM field (Cartesian) and one for a 2D EM field (cylindrically symmetric). For either case, there is a constant interval between subsequent points in a given direction. However, the units depend upon the dimension of the field - 2D or 3D. The input file format for a 3D field is shown in Table 49. The grid point positions are given in units of meters (m), the E field components in volts per meter (V/m),

TABLE 48: EM field file format for *Astra* input.

Nx	x_1	x_2	$x_{\mathrm{Nx}-1}$	x_{Nx}
Ny	y_1	y_2	$y_{\mathrm{Ny}-1}$	y_{Ny}
Nz	z_1	z_2	$z_{\mathrm{Nz}-1}$	z_{Nz}
$\mathcal{F}(x_1, y_1, z_1)$		$\mathcal{F}(x_2, y_1, z_1)$	. . . . .	$\mathcal{F}(x_{\mathrm{Nx}}, y_1, z_1)$
$\mathcal{F}(x_1, y_2, z_1)$		$\mathcal{F}(x_2, y_2, z_1)$	. . . . .	$\mathcal{F}(x_{\mathrm{Nx}}, y_2, z_1)$
.				
.				
.				
$\mathcal{F}(x_1, y_{\mathrm{Ny}}, z_1)$		$\mathcal{F}(x_2, y_{\mathrm{Ny}}, z_1)$	. . . . .	$\mathcal{F}(x_{\mathrm{Nx}}, y_{\mathrm{Ny}}, z_1)$
$\mathcal{F}(x_1, y_1, z_2)$		$\mathcal{F}(x_2, y_1, z_2)$	. . . . .	$\mathcal{F}(x_{\mathrm{Nx}}, y_1, z_2)$
$\mathcal{F}(x_1, y_2, z_2)$		$\mathcal{F}(x_2, y_2, z_2)$	. . . . .	$\mathcal{F}(x_{\mathrm{Nx}}, y_2, z_2)$
.				
.				
.				
$\mathcal{F}(x_1, y_{\mathrm{Ny}}, z_2)$		$\mathcal{F}(x_2, y_{\mathrm{Ny}}, z_2)$	. . . . .	$\mathcal{F}(x_{\mathrm{Nx}}, y_{\mathrm{Ny}}, z_2)$
$\mathcal{F}(x_1, y_1, z_3)$		$\mathcal{F}(x_2, y_1, z_3)$	. . . . .	$\mathcal{F}(x_{\mathrm{Nx}}, y_1, z_3)$
.				
.				
.				
$\mathcal{F}(x_1, y_{\mathrm{Ny}}, z_{\mathrm{Nz}})$		$\mathcal{F}(x_2, y_{\mathrm{Ny}}, z_{\mathrm{Nz}})$	. . . . .	$\mathcal{F}(x_{\mathrm{Nx}}, y_{\mathrm{Ny}}, z_{\mathrm{Nz}})$

and B field components in teslas (T). The file format for a 2D field is shown in Table 50. The grid point positions are given in units of centimeters (cm), the E field components in megavolts per meter (MV/m), the H field component in amperes per meter (A/m).

A.2 PYTHON CODES TO TRANSLATE OUTPUT TO INPUT FORMAT

A.2.1 PYTHON CODE TO TRANSFORM CST MICROWAVE STUDIO OUTPUT TO *ASTRA* INPUT

```
import math

def map(fileName, type):
    input = file(fileName,'r')
    outputx = open("TM_3D." + type + "x",'w')
    outputy = open("TM_3D." + type + "y",'w')
    outputz = open("TM_3D." + type + "z",'w')

    if type == 'e':
        a = 3
        mu = 1.0
    else:
        a = 6
        mu = 4.0*math.pi*math.pow(10.0,-7)

    field = {}
    x = []
    y = []
    z = []

    #Get rid of headers
    temp = input.readline()
    temp = input.readline()

    #read in coordinates and field
```

TABLE 49: EM Cartesian field file format for IMPACT-T input.

x_1 x_{Nx} $\mathrm{Nx}-1$					
y_1 y_{Ny} $\mathrm{Ny}-1$					
z_1 z_{Nz} $\mathrm{Nz}-1$					
$E_x(x_1, y_1, z_1)$	$E_y(x_1, y_1, z_1)$	$E_z(x_1, y_1, z_1)$	$B_x(x_1, y_1, z_1)$	$B_y(x_1, y_1, z_1)$	$B_z(x_1, y_1, z_1)$
$E_x(x_2, y_1, z_1)$	$E_y(x_2, y_1, z_1)$	$E_z(x_2, y_1, z_1)$	$B_x(x_2, y_1, z_1)$	$B_y(x_2, y_1, z_1)$	$B_z(x_2, y_1, z_1)$
.					
.					
.					
$E_x(x_{\mathrm{Nx}}, y_1, z_1)$	$E_y(x_{\mathrm{Nx}}, y_1, z_1)$	$E_z(x_{\mathrm{Nx}}, y_1, z_1)$	$B_x(x_{\mathrm{Nx}}, y_1, z_1)$	$B_y(x_{\mathrm{Nx}}, y_1, z_1)$	$B_z(x_{\mathrm{Nx}}, y_1, z_1)$
$E_x(x_1, y_2, z_1)$	$E_y(x_1, y_2, z_1)$	$E_z(x_1, y_2, z_1)$	$B_x(x_1, y_2, z_1)$	$B_y(x_1, y_2, z_1)$	$B_z(x_1, y_2, z_1)$
$E_x(x_2, y_2, z_1)$	$E_y(x_2, y_2, z_1)$	$E_z(x_2, y_2, z_1)$	$B_x(x_2, y_2, z_1)$	$B_y(x_2, y_2, z_1)$	$B_z(x_2, y_2, z_1)$
.					
.					
.					
$E_x(x_{\mathrm{Nx}}, y_{\mathrm{Ny}}, z_1)$	$E_y(x_{\mathrm{Nx}}, y_{\mathrm{Ny}}, z_1)$	$E_z(x_{\mathrm{Nx}}, y_{\mathrm{Ny}}, z_1)$	$B_x(x_{\mathrm{Nx}}, y_{\mathrm{Ny}}, z_1)$	$B_y(x_{\mathrm{Nx}}, y_{\mathrm{Ny}}, z_1)$	$B_z(x_{\mathrm{Nx}}, y_{\mathrm{Ny}}, z_1)$
$E_x(x_1, y_1, z_2)$	$E_y(x_1, y_1, z_2)$	$E_z(x_1, y_1, z_2)$	$B_x(x_1, y_1, z_2)$	$B_y(x_1, y_1, z_2)$	$B_z(x_1, y_1, z_2)$
$E_x(x_2, y_1, z_2)$	$E_y(x_2, y_1, z_2)$	$E_z(x_2, y_1, z_2)$	$B_x(x_2, y_1, z_2)$	$B_y(x_2, y_1, z_2)$	$B_z(x_2, y_1, z_2)$
.					
.					
.					
$E_x(x_{\mathrm{Nx}}, y_{\mathrm{Ny}}, z_2)$	$E_y(x_{\mathrm{Nx}}, y_{\mathrm{Ny}}, z_2)$	$E_z(x_{\mathrm{Nx}}, y_{\mathrm{Ny}}, z_2)$	$B_x(x_{\mathrm{Nx}}, y_{\mathrm{Ny}}, z_2)$	$B_y(x_{\mathrm{Nx}}, y_{\mathrm{Ny}}, z_2)$	$B_z(x_{\mathrm{Nx}}, y_{\mathrm{Ny}}, z_2)$
.					
.					
.					
$E_x(x_{\mathrm{Nx}}, y_{\mathrm{Ny}}, z_{\mathrm{Nz}})$	$E_y(x_{\mathrm{Nx}}, y_{\mathrm{Ny}}, z_{\mathrm{Nz}})$	$E_z(x_{\mathrm{Nx}}, y_{\mathrm{Ny}}, z_{\mathrm{Nz}})$	$B_x(x_{\mathrm{Nx}}, y_{\mathrm{Ny}}, z_{\mathrm{Nz}})$	$B_y(x_{\mathrm{Nx}}, y_{\mathrm{Ny}}, z_{\mathrm{Nz}})$	$B_z(x_{\mathrm{Nx}}, y_{\mathrm{Ny}}, z_{\mathrm{Nz}})$

TABLE 50: EM Cylindrically symmetric field file format for IMPACT-T input.

z_1 z_{Nz} $\mathrm{Nz}-1$		
0		
r_1 r_{Nr} $\mathrm{Nr}-1$		
$E_z(z_1, r_1)$	$E_r(z_1, r_1)$	$\lvert\mathbf{E}(z_1, r_1)\rvert$
$H_\theta(z_1, r_1)$		
$E_z(z_2, r_1)$	$E_r(z_2, r_1)$	$\lvert\mathbf{E}(z_2, r_1)\rvert$
$H_\theta(z_2, r_1)$		
.		
.		
.		
$E_z(z_{\mathrm{Nz}}, r_1)$	$E_r(z_{\mathrm{Nz}}, r_1)$	$\lvert\mathbf{E}(z_{\mathrm{Nz}}, r_1)\rvert$
$H_\theta(z_{\mathrm{Nz}}, r_1)$		
$E_z(z_1, r_2)$	$E_r(z_1, r_2)$	$\lvert\mathbf{E}(z_1, r_2)\rvert$
$H_\theta(z_1, r_2)$		
$E_z(z_2, r_2)$	$E_r(z_2, r_2)$	$\lvert\mathbf{E}(z_2, r_2)\rvert$
$H_\theta(z_2, r_2)$		
.		
.		
.		
$E_z(z_{\mathrm{Nz}}, r_2)$	$E_r(z_{\mathrm{Nz}}, r_2)$	$\lvert\mathbf{E}(z_{\mathrm{Nz}}, r_2)\rvert$
$H_\theta(z_{\mathrm{Nz}}, r_2)$		
.		
.		
.		
$E_z(z_{\mathrm{Nz}}, r_{\mathrm{Nr}})$	$E_r(z_{\mathrm{Nz}}, r_{\mathrm{Nr}})$	$\lvert\mathbf{E}(z_{\mathrm{Nz}}, r_{\mathrm{Nr}})\rvert$
$H_\theta(z_{\mathrm{Nz}}, r_{\mathrm{Nr}})$		

```
temp = input.readline()

while temp:
    holder = temp.split()

    add(x, holder[0])
    add(y, holder[1])
    add(z, holder[2])

    pos = str(float(holder[0])) + "_" + str(float(holder[1]))
       + "_" + str(float(holder[2]))

    field[pos] = [float(holder[a]), float(holder[a+1]), float(
       holder[a+2])]

    temp = input.readline()

xlen = len(x)
ylen = len(y)
zlen = len(z)

#output header (coord list)
#x coordinate
xcount = 0
outputx.write(str(xlen) + '\t')
outputy.write(str(xlen) + '\t')
outputz.write(str(xlen) + '\t')
while xcount < xlen:
    outputx.write(str(0.001*x[xcount]) + '\t')
    outputy.write(str(0.001*x[xcount]) + '\t')
    outputz.write(str(0.001*x[xcount]) + '\t')
    xcount = xcount + 1
outputx.write('\n')
outputy.write('\n')
```

```
outputz.write('\n')

#y coordinate
ycount = 0
outputx.write(str(ylen) + '\t')
outputy.write(str(ylen) + '\t')
outputz.write(str(ylen) + '\t')
while ycount < ylen:
    outputx.write(str(0.001*y[ycount]) + '\t')
    outputy.write(str(0.001*y[ycount]) + '\t')
    outputz.write(str(0.001*y[ycount]) + '\t')
    ycount = ycount + 1
outputx.write('\n')
outputy.write('\n')
outputz.write('\n')

#z coordinate
zcount = 0
outputx.write(str(zlen) + '\t')
outputy.write(str(zlen) + '\t')
outputz.write(str(zlen) + '\t')
while zcount < zlen:
    outputx.write(str(0.001*z[zcount]) + '\t')
    outputy.write(str(0.001*z[zcount]) + '\t')
    outputz.write(str(0.001*z[zcount]) + '\t')
    zcount = zcount + 1
outputx.write('\n')
outputy.write('\n')
outputz.write('\n')

#field output
zcount = 0
while zcount < zlen:
    ycount = 0
```

```
        while ycount < ylen:
            xcount = 0
            while xcount < xlen:
                pos = str(x[xcount]) + "_" + str(y[ycount]) + "_"
                   + str(z[zcount])
                outputx.write(str(mu*field[pos][0]) + '\t')
                outputy.write(str(mu*field[pos][1]) + '\t')
                outputz.write(str(mu*field[pos][2]) + '\t')
                xcount = xcount + 1
            outputx.write('\n')
            outputy.write('\n')
            outputz.write('\n')
            ycount = ycount + 1
        zcount = zcount + 1

    #close files
    outputx.close()
    outputy.close()
    outputz.close()

def cull(fileName, output):
    input = file(fileName,'r')
    output = open(output,'w')

    #cut off of 60 mm from center
    limit = 60.0

    output.write(input.readline())
    output.write(input.readline())

    temp = input.readline()

    while temp:
        hold = temp.split()
```

```
            if math.fabs(float(hold[0])) < limit and math.fabs(float(
                hold[1])) < limit:
                output.write(temp)

            temp = input.readline()

        input.close()
        output.close()

def add(list, number):
        coord = float(number)

        if list.count(coord) == 0:
            list.append(coord)
```

If the code excerpt above is located within the file "Formatting2.py", then given two field map files produced by CST Microwave Studio ("E_Racetrack.txt" and "H_Racetrack.txt"), the proper method and order of calling these functions is shown below, assuming all three files are located within the same folder. The **cull** function restricts the map to a given radius around the center of the cavity (60 mm in the above example). This is simply to restrict the input file size, as sufficiently large field maps will require a long run time when used as input to the **map** function, and this approach produces identical results as simulations run using the full map. The **map** function produces a correctly formatted file using the desired units for input into *Astra*. While it is clear in retrospect that this approach is unnecessary and a different function could easily avoid this difficulty, rewriting the **map** function never became a priority, as the function did the job required.

```
>>> Formatting2.cull("E_Racetrack.txt", "Small_E_Racetrack.txt")
>>> Formatting2.cull("H_Racetrack.txt", "Small_H_Racetrack.txt")
>>> Formatting2.map("Small_E_Racetrack.txt", 'e')
>>> Formatting2.map("Small_H_Racetrack.txt", 'b')
```

A.2.2 PYTHON CODE TO TRANSFORM SUPERFISH OUTPUT TO *ASTRA* INPUT

```
import math
```

```
def fieldTranslate(fileIn, fileOut):
    input = file(fileIn, 'r')
    outputE = open(fileOut + "_E.txt", 'w')
    outputH = open(fileOut + "_H.txt", 'w')

    #weed out header information
    temp = input.readline()
    i = 1
    while i < 33:
        temp = input.readline()
        i = i + 1

    field = {}
    z = []
    r = []

    posFactor = 10.
    eFactor = 1.0*math.pow(10.0,6)
    zShift = -149.99
    tLimit = 3.0
    tStep = 0.15

    #input
    temp = input.readline()
    hold = temp.split()
    cont = True
    first = True
    while cont:
        add(z, hold[0])
        add(r, hold[1])
        pos = str(float(hold[0])) + "_" + str(float(hold[1]))
        field[pos] = [float(hold[2]), float(hold[3]), float(hold
            [5])]
```

```
        if first:
            print pos
            first = False

        temp = input.readline()
        hold = temp.split()
        if len(hold) == 6:
            cont = True
        else:
            cont = False

    #output
    grid = [0.0, 0.15, 0.30, 0.45, 0.60, 0.75, 0.90, 1.05, 1.20,
       1.35, 1.50, 1.65, 1.80, 1.95, 2.10, 2.25, 2.40, 2.55, 2.70,
        2.85, 3.0, 3.15, 3.30, 3.45, 3.60, 3.75, 3.90, 4.05, 4.20,
        4.35, 4.50, 4.65, 4.80, 4.95, 5.10, 5.25, 5.40, 5.55,
       5.70, 5.85, 6.0]
    zlen = len(z)
    rlen = len(r)
    zcount = 0
    outputE.write("Heading line 1\n")
    outputE.write("Heading line 2\n")
    outputH.write("Heading line 1\n")
    outputH.write("Heading line 2\n")
    while zcount < zlen:
        ycount = 0
        y = {}
        while ycount < len(grid):
            x = {}
            rcount = 0
            #apply to grid
            while rcount < rlen:
                if math.fabs(grid[ycount]) <= r[rcount]:
```

```
            if rcount == 0:
                phi = 0.0
            else:
                phi = math.asin(grid[ycount]/r[rcount])
            xVal = r[rcount]*math.fabs(math.cos(phi))
            pos = str(z[zcount]) + "_" + str(r[rcount])
            x[xVal] = [field[pos][1]*math.fabs(math.cos(
                phi)), field[pos][1]*math.fabs(math.sin(phi
                )), field[pos][0], field[pos][2]*-1.0*math.
                fabs(math.sin(phi)), field[pos][2]*math.
                fabs(math.cos(phi))]
        rcount = rcount + 1
    #interpolate
    xcount = ycount
    xKeys = x.keys()
    xKeys.sort()
    xlen = len(xKeys)
    y[grid[ycount]] = {}
    lb = 0
    rb = 1
    while xcount < len(grid):
        lb = seek(grid[xcount], xKeys)
        rb = lb + 1
        y[grid[ycount]][grid[xcount]] = interpolate(grid[
            xcount], xKeys[lb], xKeys[rb], x[xKeys[lb]], x[
            xKeys[rb]])
        if zcount == 170 and ycount == 4:
            print str(xcount) + '\t' + str(xKeys[lb]) + '\
                t' + str(xKeys[rb])
            print x[xKeys[lb]]
            print x[xKeys[rb]]
            print y[grid[ycount]][grid[xcount]]
            print '\n'
        xcount = xcount + 1
```

```
        #step
        ycount = ycount + 1
        del x

    #reflection over line
    ycount = 1
    while ycount < len(grid):
        xcount = 0
        while xcount < ycount:
            a = y[grid[xcount]][grid[ycount]]
            y[grid[ycount]][grid[xcount]] = [a[1], a[0], a[2],
                -1.0*a[4], -1.0*a[3]]
            del a
            xcount = xcount + 1
        ycount = ycount + 1

    #output
    ycount = len(grid) - 1
    while ycount > 0:
        xcount = len(grid) - 1
        while xcount > 0:
            xVal = grid[xcount]
            yVal = grid[ycount]
            pos = str(-1.0*xVal*posFactor) + '\t' + str(-1.0*
                yVal*posFactor) + '\t' + str(z[zcount]*
                posFactor + zShift) + '\t'
            outputE.write(pos + str(y[yVal][xVal][0]*eFactor
                *-1.0) + '\t' + str(y[yVal][xVal][1]*eFactor
                *-1.0) + '\t' + str(y[yVal][xVal][2]*eFactor) +
                 '\t0\t0\t0\n')
            outputH.write(pos + '0\t0\t0\t' + str(y[yVal][xVal
                ][3]*-1.0) + '\t' + str(y[yVal][xVal][4]*-1.0)
                + '\t0\n')
            xcount = xcount - 1
```

```
        while xcount < len(grid):
            xVal = grid[xcount]
            yVal = grid[ycount]
            pos = str(1.0*xVal*posFactor) + '\t' + str(-1.0*
                yVal*posFactor) + '\t' + str(z[zcount]*
                posFactor + zShift) + '\t'
            outputE.write(pos + str(y[yVal][xVal][0]*eFactor
                *1.0) + '\t' + str(y[yVal][xVal][1]*eFactor
                *-1.0) + '\t' + str(y[yVal][xVal][2]*eFactor) +
                 '\t0\t0\t0\n')
            outputH.write(pos + '0\t0\t0\t' + str(y[yVal][xVal
                ][3]*-1.0) + '\t' + str(y[yVal][xVal][4]*1.0) +
                 '\t0\n')
            xcount = xcount + 1

        ycount = ycount - 1

    while ycount < len(grid):
        xcount = len(grid) - 1
        while xcount > 0:
            xVal = grid[xcount]
            yVal = grid[ycount]
            pos = str(-1.0*xVal*posFactor) + '\t' + str(1.0*
                yVal*posFactor) + '\t' + str(z[zcount]*
                posFactor + zShift) + '\t'
            outputE.write(pos + str(y[yVal][xVal][0]*eFactor
                *-1.0) + '\t' + str(y[yVal][xVal][1]*eFactor
                *1.0) + '\t' + str(y[yVal][xVal][2]*eFactor) +
                '\t0\t0\t0\n')
            outputH.write(pos + '0\t0\t0\t' + str(y[yVal][xVal
                ][3]*1.0) + '\t' + str(y[yVal][xVal][4]*-1.0) +
                 '\t0\n')
            xcount = xcount - 1
```

```
            while xcount < len(grid):
                xVal = grid[xcount]
                yVal = grid[ycount]
                pos = str(1.0*xVal*posFactor) + '\t' + str(1.0*
                    yVal*posFactor) + '\t' + str(z[zcount]*
                    posFactor + zShift) + '\t'
                outputE.write(pos + str(y[yVal][xVal][0]*eFactor
                    *1.0) + '\t' + str(y[yVal][xVal][1]*eFactor
                    *1.0) + '\t' + str(y[yVal][xVal][2]*eFactor) +
                    '\t0\t0\t0\n')
                outputH.write(pos + '0\t0\t0\t' + str(y[yVal][xVal
                    ][3]*1.0) + '\t' + str(y[yVal][xVal][4]*1.0) +
                    '\t0\n')
                xcount = xcount + 1

            ycount = ycount + 1

        del y
        zcount = zcount + 1

    input.close()
    outputE.close()
    outputH.close()

def add(list, number):
    coord = float(number)

    if list.count(coord) == 0:
        list.append(coord)

def seek(value, list):
    limit = len(list)
    i = 0
```

```
    lost = True

    while lost and i < limit:
        if list[i] > value:
            lost = False
        else:
            i = i + 1

    if lost:
        return -1
    else:
        return i - 1

def interpolate(x, a, b, ya, yb):
    y = [0, 0, 0, 0, 0]
    i = 0

    while i < 5:
        y[i] = ya[i] + (x - a)*(yb[i] - ya[i])/(b - a)
        i = i + 1

    return y
```

The code excerpt above, contained in the file "SFCollection.py", translates the output from Superfish into the output format of CST Microwave Studio when the **fieldTranslate** function is called. At that point, the newly created files are used as input into the **map** function from the previous subsection. The **cull** function does not need to be called, as **fieldTranslate** only creates data for the field immediately near the ideal beam-trajectory.

A.2.3 PYTHON CODE TO TRANSFORM CST MICROWAVE STUDIO OUTPUT TO IMPACT-T INPUT

```
def CST2Impact(inputE, inputH, outputFile):
    input = file(inputE, 'r')
    output = open(outputFile, 'w')
```

```
mu = 4.0*math.pi*math.pow(10.0,-7)

x = []
y = []
z = []

#Get rid of headers
temp = input.readline()
temp = input.readline()

#read in coordinates and field
temp = input.readline()

while temp:
    holder = temp.split()

    add(x, holder[0])
    add(y, holder[1])
    add(z, holder[2])

    temp = input.readline()

input.close()
output.write(str(float(x[0])*0.001) + " " + str(float(x[len(x)
    -1])*0.001) + " " + str(len(x) - 1) + '\n')
output.write(str(float(y[0])*0.001) + " " + str(float(y[len(y)
    -1])*0.001) + " " + str(len(y) - 1) + '\n')
output.write(str(float(z[0])*0.001) + " " + str(float(z[len(z)
    -1])*0.001) + " " + str(len(z) - 1) + '\n')

inputE = file(inputE, 'r')
inputH = file(inputH, 'r')
```

```
    #get rid of headers and read first field line
    tempE = inputE.readline()
    tempE = inputE.readline()
    tempE = inputE.readline()
    tempH = inputH.readline()
    tempH = inputH.readline()
    tempH = inputH.readline()

    while tempE:
        holdE = tempE.split()
        holdH = tempH.split()

        output.write(holdE[3] + "  " + holdE[4] + "  " + holdE[5]
            + "  " + str(float(holdH[6])*mu) + "  " + str(float(
            holdH[7])*mu) + "  " + str(float(holdH[8])*mu) + '\n')

        tempE = inputE.readline()
        tempH = inputH.readline()

    inputE.close()
    inputH.close()
    output.close()



def add(list, number):
    coord = float(number)

    if list.count(coord) == 0:
        list.append(coord)
```

Unlike *Astra*, IMPACT-T requires all the EM field components in a single file. Consequently, the **CST2Impact** function requires both the E and H field files.

A.2.4 PYTHON CODE TO TRANSFORM SUPERFISH OUTPUT TO IMPACT-T INPUT

```
def field2impact(fileIn, fileOut):
    input = file(fileIn, 'r')
    output = open(fileOut, 'w')

    #weed out useless header info
    temp = input.readline()
    i = 1
    while i < 28:
        temp = input.readline()
        i = i + 1

    #increment info
    temp = input.readline()
    #print temp.split()
    hold = (temp.split()[2]).split(',')
    #print hold
    zMin = float((hold[0]).split('(')[1])
    rMin = float((hold[1]).split(')')[0])
    temp = input.readline()
    hold = (temp.split()[2]).split(',')
    zMax = float((hold[0]).split('(')[1])
    rMax = float((hold[1]).split(')')[0])
    zMax = zMax - zMin
    zMin = 0.0
    temp = input.readline()
    hold = temp.split()
    zStep = hold[4]
    rStep = hold[5]

    output.write(str(zMin) + '\t' + str(zMax) + '\t' + zStep + '\n
        ')
    output.write("2865\n")
    output.write(str(rMin) + '\t' + str(rMax) + '\t' + rStep + '\n
        ')
```

```
temp = input.readline()
temp = input.readline()
temp = input.readline()
temp = input.readline()
hold = temp.split()
cont = True
while cont:
    output.write(hold[2] + '\t' + hold[3] + '\t' + hold[4] + '
       \n')
    output.write(hold[5] + '\n')
    temp = input.readline()
    hold = temp.split()
    if len(hold) == 6:
        cont = True
    else:
        cont = False

input.close()
output.close()
```

It is possible to treat the gun field in the same manner as the CST fields - call **Field-Translate** from "SFCollection.py" and use the created files as input for the **CST2Impact** function from the previous subsection. However, this method treats the gun field as a fully 3D map, instead of a cylindrically symmetric field map. The **field2impact** function instead formats the input for a 2D field and removes the need for intermediary steps.

APPENDIX B

GENERATING REENTRANT GEOMETRY

```
import math

def drawGun(values, fileName):
    yCav = values[0]
    h = values[1]
    rPipe = values[2]
    xE = values[3]
    yE = values[4]
    alpha = math.radians(values[5])
    lFin = values[6]
    hFin = values[7]
    lGap = values[8]
    lRec = values[9]
    yE2 = values[10]

    rEnt = 6.0
    #rEnt = h ?
    rCathode = 4.0
    rCav = yCav

    if math.cos(alpha) <= 0.0 or lRec <= 0.0 or (1.0 + math.cos(
       alpha) + math.tan(alpha)*(math.sin(alpha) - 1.0)) == 0.0:
        cont = False
    else:
        cont = True

    if cont:
        rRec = yE - rEnt
```

```
        yRec = yE
        xRec = xE - rRec
        yNC = yE
        rNC = (rCav - hFin - yNC)/math.cos(alpha)
        xNC = xE - rNC
        rFin = (hFin - math.tan(alpha)*(xNC + rNC*math.sin(alpha)
            + lFin))/(1.0 + math.cos(alpha) + math.tan(alpha)*(math
            .sin(alpha) - 1.0))
        xFin = rFin - lFin
        yFin = rCav - rFin
        yBot = yE2
        rBot = yE2 - rPipe
        xBot = xE + lGap + rBot
        rTop = rBot
        yTop = rCav - rTop
        xTop = xE + lGap + lRec - rTop
        ySph = yE2
        rSph = ((yTop - ySph)*(yTop - ySph) + xTop*(xTop) + (xE +
            lGap)*(xE + lGap) - (rTop*rTop) - 2.0*xTop*(xE + lGap))
            /(2.0*lRec)
        xSph = xE + lGap + rSph

    if (xSph - xTop) == 0.0:
        cont = False
    else:
        cont = True

    if cont:
        phi = math.atan((yTop - ySph)/(xSph - xTop))

    if yE <= rEnt:
        cont = False
    if yE2 <= rPipe:
        cont = False
```

```
if rRec <= 0.0 or rNC <= 0.0 or rFin <= 0.0 or rTop <= 0.0 or
   rSph <= 0.0 or rBot <= 0.0:
    cont = False
if (rNC + rFin)*math.sin(alpha) < (xFin - xNC):
    cont = False
if (rNC + rFin)*math.cos(alpha) > (yFin - yNC):
    connt = False
if (xTop + rTop*math.cos(phi)) <= (xE + lGap):
    cont = False
if (yTop - rTop*math.sin(phi)) <= yE2:
    cont = False

if cont:
    output = open(fileName, 'w')
    output.write("0\t0\n")
    output.write("0\t3.5\n")
    output.write("2\t-0.5\t 3.5\t-0.5\t4.0\n")
    output.write("-6.0\t4.0\n-12.0\t14.0\n-149.99\t14.0\n
       -149.99\t15.0\n-12.0\t15.0\n")
    output.write("-6.0\t" + str(h) + "\n")
    output.write(str(xRec) + '\t' + str(h) + '\n')
    hold = [xRec, yE, xE, yE]
    output.write("2\t" + compLine(hold) + '\n')
    hold = [xNC, yNC, xNC + rNC*math.sin(alpha), yNC + rNC*
       math.cos(alpha)]
    output.write("2\t" + compLine(hold) + '\n')
    hold = [xFin - rFin*math.sin(alpha), yFin - rFin*math.cos(
       alpha)]
    output.write(compLine(hold) + '\n')
    hold = [xFin, yFin, xFin, yCav]
    output.write("2\t" + compLine(hold) + '\n')
    hold = [xTop, yCav]
    output.write(compLine(hold) + '\n')
```

```
        hold = [xTop, yTop, xTop + rTop*math.cos(phi), yTop - rTop
            *math.sin(phi)]
        output.write("2\t" + compLine(hold) + '\n')
        hold = [xSph, ySph, xSph - rSph, ySph]
        output.write("2\t" + compLine(hold) + '\n')
        hold = [xBot, yBot, xBot, yBot - rBot]
        output.write("2\t" + compLine(hold) + '\n')
        output.write("150.01\t10.0\n150.01\t0.0\n0.0\t0.0\n")
        output.close()

    return cont

def translate(fileIn):
    input = file(fileIn,'r')
    output = open("Translated.txt", 'w')

    temp = input.readline()
    shift = 149.99
    factor = 0.1
    while temp:
        hold = temp.split()
        output.write("$po ")
        if len(hold) == 2:
            output.write("x=" + str((float(hold[0])+shift)*factor)
                + ", y=" + str(float(hold[1])*factor) + " $\n")
        if len(hold) == 5:
            x0 = float(hold[1])
            y0 = float(hold[2])
            output.write("nt=2, x0=" + str((x0+shift)*factor) + ",
                y0=" + str(y0*factor) + ", x=" + str((float(hold
                [3]) - x0)*factor) + ", y=" + str((float(hold[4]) -
                 y0)*factor) + " $\n")
        temp = input.readline()
```

```
    input.close()
    output.close()
    print "Done!"

def translateEntire(fileIn, fileOut, radius):
    translate(fileIn)
    output = open(fileOut, 'w')

    output.write("RFGun\n\n&reg kprob=1,\t! Superfish\nicylin=1\t!
        Cylindrical symmetry\ndx=.035,\t! Mesh interval\nfreq
        =495.0,\t! Starting frequency\nxdri=13.025,ydri=" + str
        (0.1*radius) + ",\t! Drive point coordinates\nkmethod=1\t!
        Use beta to compute wave number\nbeta=0.95 &\t! Particle
        velocity for transit-time integrals\n")

    output.write('\n')
    input = file("Translated.txt",'r')
    temp = input.readline()

    while temp:
        output.write(temp)
        temp = input.readline()

    input.close()
    output.close()
```

The code excerpt above allows for gun geometry parameters, which have been defined elsewhere in the document, to be used to generate an input file suitable for Autofish input, which can be used to calculate the EM fields of the gun. An example of how to properly call these functions is given below, assuming all three are contained in the file "SFCollection.py". The numbers given below correspond to the final gun geomety.

```
>>> parameters = [134.24, 6.0, 10.0, 4.0, 10.0, 13.0, 127.95,
    52.734, 60.0, 30.0, 15.0]
>>> SFCollection.drawGun(parameters, "Input01.txt")
```

```
>>> SFCollection.translateEntire("Input01.txt", "RFGun.af",
    134.24)
```

VITA

Kirsten Elizabeth Deitrick
Department of Physics
Old Dominion University
Norfolk, VA 23529

Kirsten Deitrick was born on March 17, 1989 in St. Paul, Minnesota. She was awarded a Bachelor of Science degree in Physics from Rensselaer Polytechnic Institute in Troy, New York, USA in May of 2011. Kirsten became a graduate student of the Department of Physics at Old Dominion University in Norfolk, Virginia, USA in August of 2011 and completed her Masters of Science degree in Physics in August of 2014.

Typeset using LaTeX.